Final Report

LIDAR STUDY OF STACK PLUMES

By: WARREN B. JOHNSON, JR. and EDWARD E. UTHE

Prepared for:

DEPARTMENT OF HEALTH, EDUCATION, AND WELFARE
NATIONAL AIR POLLUTION CONTROL ADMINISTRATION
DIVISION OF METEOROLOGY
411 WEST CHAPEL HILL STREET
DURHAM, NORTH CAROLINA 27701

CONTRACT PH 22-68-33

STANFORD RESEARCH INSTITUTE
Menlo Park, California 94025 • U.S.A.

STANFORD RESEARCH INSTITUTE
Menlo Park, California 94025 · U.S.A.

Final Report

LIDAR STUDY OF STACK PLUMES

By: WARREN B. JOHNSON, JR. and EDWARD E. UTHE

Prepared for:

DEPARTMENT OF HEALTH, EDUCATION, AND WELFARE
NATIONAL AIR POLLUTION CONTROL ADMINISTRATION
DIVISION OF METEOROLOGY
411 WEST CHAPEL HILL STREET
DURHAM, NORTH CAROLINA 27701

CONTRACT PH 22-68-33

SRI Project 7289

Approved:

R. T. H. COLLIS
Director
Aerophysics Laboratory

RAY L. LEADABRAND
Executive Director
Electronics and Radio Sciences Division

Copy No. 112

ABSTRACT

The feasibility of lidar (laser radar) for stack plume studies is established from the results of an experimental investigation of plume behavior from a 245-m power plant stack in western Pennsylvania. During this study a total of 175 vertical plume cross sections containing about 3800 separate lidar observations were obtained, of which 64 cross sections representative of various types of plume behavior were selected for detailed analysis. Each vertical cross section was built up from 15 to 30 lidar shots at 5 to 8 second intervals and at elevation angle increments of $1/3^{\circ}$ to 10°. The selected cross sections are grouped into series which show the spatial (downwind) and temporal variations in plume geometry and relative particulate concentration distributions.

The factors involved in interpreting the lidar data in terms of plume rise and diffusion are discussed and exemplified. Although calculated plume-rise values agree reasonably well with the observations, it is clear from inspection of the cross sections that the important effects of vertical wind direction shear (plume tilting and fanning) and vertical changes in stability (plume trapping) should be taken into account when predicting plume rise and diffusion. Close correspondence between plume tops and levels of increased atmospheric stability was found. Several cross sections are shown of fumigating plumes, which occurred frequently. In a tilted plume, different portions apparently fumigate at different times. Optimum use of lidar for diffusion studies requires provision for obtaining 30-minute or hourly plume concentration distributions, as well as allowances for the effect of the lidar noise level upon plume size.

To investigate the potential of lidar for making quantitative measurements, a sample cross section of absolute mass concentration was computed on the basis of Mie scattering theory and independent particle size measurements. The cross-axial integrated mass concentration represented by this cross section is 680 g/m. The corresponding value calculated from the gross power-plant data and wind speed is 875 g/m.

The advantages of the mobile lidar technique stem from its ability to obtain measurements remotely and at a high density in space and time. The quantitative application of the technique for obtaining absolute particulate mass concentrations is limited mainly by the accuracy with which the optical characteristics of the aerosol are known. An improved lidar system for plume studies would incorporate better signal-to-noise characteristics and a higher pulse repetition rate than present equipment provides. In addition, an expanded data processing capability with "real-time" output is necessary.

CONTENTS

ILLUSTRATIONS

TABLES

SYMBOLS

a = particle radius

A = effective receiver area

c = speed of light

C = particle number concentration; also parameter in formula for Junge fit to particle-size data

$\overline{C}$ = optical cross section averaged over particle size interval

E = lidar site elevation

F = buoyancy flux

g = acceleration of gravity (= 9.8 m/s)

G = stability parameter

$H(R)$ = magnitude of magnetic disk-recorded signal return from atmosphere as a function of range

H_p = height of plume axis above lidar

H_s = height of top of stack above lidar

H_t = height of plume top above lidar after maximum rise

ΔH = plume rise (height of axis of plume above stack top after reaching equilibrium)

ℓ = distance along the laser pulse propagation path

i = complex operator ($\sqrt{-1}$)

k = slope parameter in equation for Junge fit to particle-size data

$\log^*$ = logarithmic amplifier transfer function

m = refractive index of particles

M = plume mass concentration

M_o = background mass concentration in "clean" air

n = number of particles per unit volume per unit radius interval

n_r = relative density of particle-size distribution (fraction of number of particles per unit radius interval)

N = cumulative particle number concentration (number of particles larger than a given radius)

P_N = detector output component due to background and internal noise

P_S = detector output component due to backscattered signal return

P_T = peak power emitted into the atmosphere

Q_b = backscatter efficiency factor

Q_e = extinction efficiency factor

r = radius of stack orifice (= 4.25 m for Keystone)

R = range

R_o = reference range

ΔR = range increments of digitized lidar data

S = normalized, range-corrected signal return function

T = atmospheric transmission factor

T_a = ambient atmospheric temperature at stack top

T_c = beam convergence factor

T_s = stack gas exit temperature

T_t = air temperature at height of plume top

$\bar{U}$ = mean wind speed over height interval where plume rise occurs

U_a = wind speed at height of stack top (H_s)

U_t = wind speed at height of plume top (H_t) after maximum rise

V_s = stack gas exit velocity

x = particle size parameter (= $2\pi a/\lambda$)

β = volume backscatter coefficient (per steradian)

λ = wavelength of the laser energy

μ = 10^{-6} m; also used generally as 10^{-6}( )

ξ_b = backscattering optical cross section per unit mass per steradian (= β/M)

ξ_e = total scattering (extinction) optical cross section per unit mass (= σ/M)

π = 3.1416

ρ = density of the particulate matter

σ = volume extinction coefficient

τ = pulse duration

FOREWORD

This work was carried out as part of the Large Power Plant Effluent Study (LAPPES) conducted by the National Air Pollution Control Administration, and was sponsored by the Division of Meteorology of that agency under Contract PH 22-68-33.

We are grateful for the logistical and meteorological support and experimental coordination provided by Frank Schiermeier, LAPPES Field Manager, and by Larry Niemeyer and Charles Hosler of the Division of Meteorology, National Air Pollution Control Administration.

We also acknowledge the able assistance of the following Stanford Research Institute personnel: Hisao Shigeishi, Charles Brabant, and Stephanie Briggs in the computer data processing and analysis phase; Al Smith and John Alder in the manual analysis phase; and John Oblanas, Norman Nielsen, and William Dyer in the experimental program. Thanks are also due to Ron Collis, Director of the Aerophysics Laboratory, for his helpful suggestions in the writing of this report, and to William Evans for the contribution of his ideas on data display and analysis techniques.

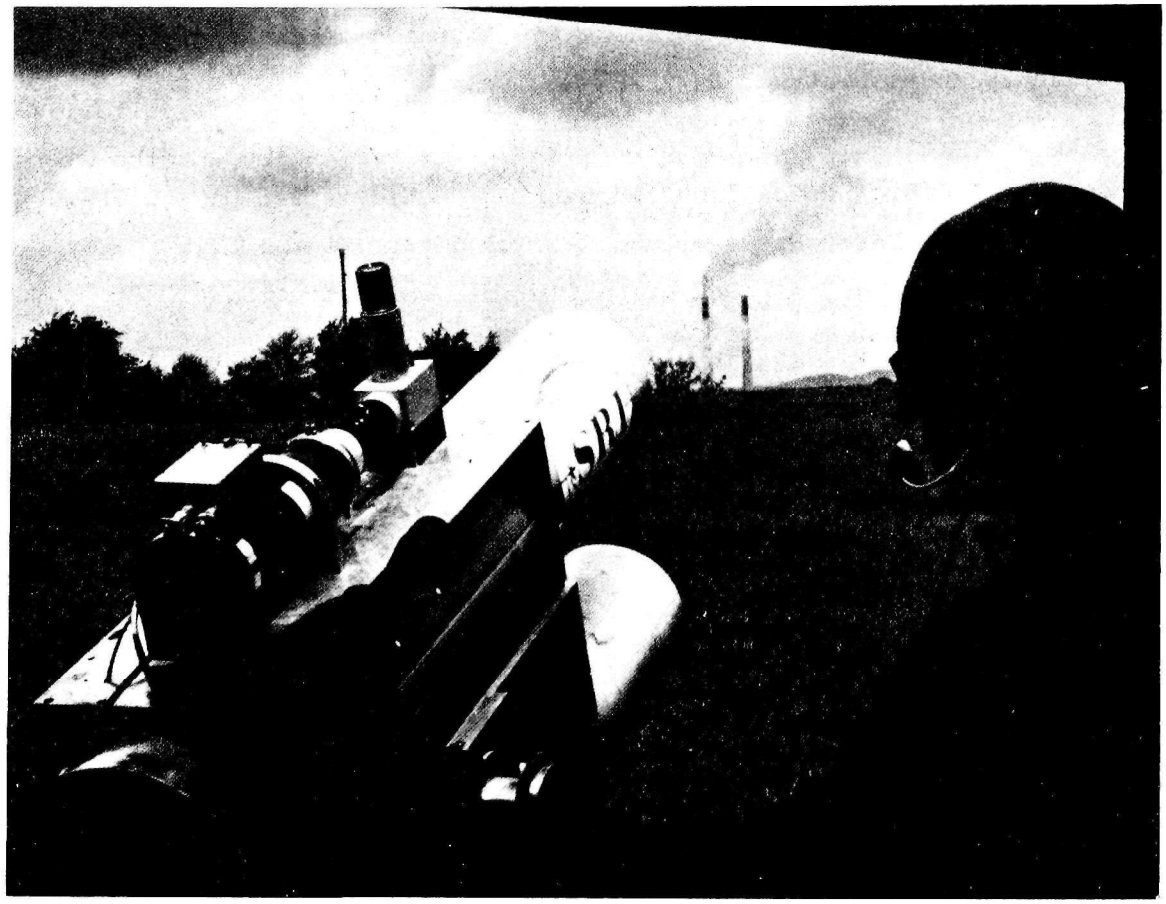

FRONTISPIECE MARK V LIDAR IN OPERATION DURING KEYSTONE STACK PLUME STUDY NEAR SHELOCTA, PENNSYLVANIA

I INTRODUCTION

The lidar, or laser radar, which was developed for meteorological use by Stanford Research Institute in 1963, has important applications in air pollution research and control activities (see Johnson, 1969; Hamilton, 1966; Barrett and Ben-Dov, 1967).* This report covers a recent experimental program, carried out for the National Air Pollution Control Administration, involving mobile lidar observations of the diffusion of the smoke plume from a 245-m stack at Keystone Generating Station in western Pennsylvania. Such tall stacks are becoming increasingly necessary in order to lower the ground concentrations of pollutants from large plants. However, these stacks cost in excess of $3000 per meter to build, and it is important to determine their efficiency, in practice, in preventing high air-pollution levels. In addition, in order to refine diffusion models used to predict pollutant concentrations from high stacks, more data are needed. Most existing diffusion models were developed before the advent of the tall stack, and the accuracy of the theoretical predictions for this application has not yet been adequately verified due to the shortage of suitable data (Smith, 1968). The new lidar technique promises to fill this need and facilitate advances in the theory of high-stack diffusion.

Using a mobile, truck-mounted lidar system, a field team from Stanford Research Institute participated in the LAPPES† experimental program during two periods: 25 May-1 June and 15-24 October 1968. Lidar observations of the smoke plume from the stack of coal-burning Keystone Generating Station were obtained on 17 days; a total of 175 vertical plume cross sections, consisting of 3806 individual lidar observations, were collected. The quality of about one-third of these data were degraded by poor weather conditions. Of the remainder,

---

*References are listed at the end of the report.

†Large Power Plant Effluent Study.

approximately 10 percent were selected for detailed manual analysis (first field program) and 46 percent were analyzed objectively using computer techniques. Representative examples of these derived plume cross sections will be presented here to illustrate the significant information which lidar observations can furnish regarding plume geometry and behavior. Although particulate emission is not the major air pollution problem associated with power plants because of the efficacy of modern ash removal devices, the smoke serves as a convenient tracer for the study of diffusion processes. Since the particles are small, their diffusion should be essentially identical with that of a gas such as SO_2.

II SUMMARY AND CONCLUSIONS

The results of the Keystone plume study with regard to plume behavior in particular, and lidar capabilities and limitations in general, are briefly itemized below, with conclusions included as appropriate.

A. Plume Characteristics

In general, the lidar observations confirmed and underscored the known and suspected complexities of plume behavior. Complicating factors--such as those mentioned below--that have been largely ignored in present theories should now be intensively studied for possible incorporation, if the theory is to stay abreast of the experimental state of the art.

Plume tilting and fanning caused by vertical wind direction shear probably affects plume rise, and definitely requires reconsideration of the definition of plume rise.

Fanning is a very common feature of plumes from high stacks observed under stable conditions and must be included in any realistic diffusion theory.

The marked effects of elevated inversions and other levels of increasing stability with height were observed frequently and need thorough consideration. Close correspondence was found between such levels and plume tops, as well as with haze tops when no plume was observed.

Plume fumigation occurs often, probably more often than previously suspected. Typically, however, only a portion of the plume fumigates at a given time, with the remainder tilted and elevated.

The meteorological regime best suited for model validation, namely nonstable conditions, also presents the most difficult observational situation for lidar. This is because of the diffuse, rapidly changing nature of plumes under these conditions. (See the instrumentation discussion later in this section.)

B. Lidar Data Analysis Considerations

The value of lidar for observing plumes was clearly established. For many applications, such as the use of particulates in a plume as tracers for the study of diffusion processes, lidar-observed relative mass concentrations, uncorrected for attenuation, should be sufficient to furnish the required information.

However, quantitative results in terms of absolute mass concentration were also obtained. A computed sample cross section corrected for attenuation gave a cross-axial integrated mass concentration of 680 g/m of plume length, compared with 875 g/m as calculated from the power plant data and wind measurements.

Our method of calculation of absolute particulate mass concentrations from the lidar data is based on the following:

(1) The same particulate relative size distribution and optical properties are assumed to hold in the clean air and plume. (The MRI data appear to confirm this.) This is a convenient but not essential assumption for obtaining a solution.

(2) The relative size distribution and optical properties are assumed to be known (measured or estimated).

(3) Mie scattering theory is assumed to be valid (this is reasonable, since the fly ash particles are spherical). Thus ξ_e, the extinction optical cross section per unit mass, can be computed.

(4) The clean air outside the plume is assumed to be homogeneous and to have a known mass concentration M_o (measured or estimated).

The integration procedure used in this method is fairly sensitive to errors in the values used for the solution parameters ξ_e and M_o.

The known errors and limitations associated with the use of collecting-type particle samplers tends to make such data incompatible with lidar data. Optical particle samplers might give more comparable

results, although there could be difficulties with any direct-sampling instrument that disturbs the medium.

The best prospects for obtaining routine quantitative data seem to lie in the direction of deriving additional information on the solution parameters by means of advanced lidar techniques, such as multiple-wavelength instruments, which may be able to eliminate the need for independent particle measurements.

C. Instrumentation Considerations

For plume cross sections built up from many individual lidar observations, an accurate shot-to-shot referencing system is essential to correct the data for pulse-to-pulse variations in transmitted power.

Higher pulse repetition rates, on the order of one to ten shots per second, are needed to observe rapidly changing plumes under unstable conditions adequately and faithfully. A water-cooled system is suggested by this requirement.

Better data handling, processing, and display capabilities are necessary to assimilate larger quantities of data properly. New techniques, ideally of the real-time analog type, are needed to provide a capability of averaging many cross sections to obtain an hourly mean concentration distribution with which to check diffusion theories.

The usefulness of lidar data would be considerably enhanced if instrumentation with higher power output and lower noise susceptibility, and thus greater range, were used. A lidar with an effective above-noise range (for the clear-air return) of about 8 km would be ideal for plume studies. The neodymium system used in this study has an effective range for clear-air return of about one to two km,* and thus could observe only the denser parts of "clean"† plumes at ranges greater than

---

*This range is variable, depending upon the level of background illumination.

†When all electrostatic precipitators were operating.

this. The Mark V ruby lidar would give much better results in this respect due to its shorter wavelength, narrower spectral region, and greater receiver sensitivity, but the pulse repetition rate needs to be increased.

In this connection, it is encouraging to note that neither the ruby nor neodymium versions of the SRI Mark V lidar approach the limits of current technology, and systems with the recommended performance can readily be developed.

III DESCRIPTION OF THE EXPERIMENTAL PROGRAM

A. Instrumentation

The SRI Mark V lidar (Fig. 1) was used during both field programs in a mobile, truck-mounted configuration. The characteristics of this instrument are detailed in Appendix A. As are all lidars, the Mark V is basically composed of a laser transmitter, which emits a very brief, high-intensity pulse of coherent monochromatic light, and a receiver, which detects the energy at that wavelength backscattered from the atmospheric aerosol as a function of range.

The transmitter of this instrument employs either a neodymium-doped glass laser rod or a ruby rod, at wavelengths of 1.06 and 0.694 μ respectively. The neodymium laser was used for the plume study because of its faster pulse repetition rate (approximately 10 pulses/min vs 3 pulses/min for the ruby). However, due to the much lower quantum efficiencies and higher dark currents of the best available photomultiplier tubes at 1.06 μ, and the wider filter bandpass needed for this system, overall receiver sensitivity, signal-to-noise ratio, and thus range is significantly reduced over that obtainable with the ruby system.

The lidar data were recorded on both a video magnetic disk recorder* and on an oscilloscope equipped with a 35-mm recording camera. A second oscilloscope used in conjunction with the disk recorder permitted an "instant replay" of each lidar shot, thereby providing real-time monitoring of the data. A 3-MHz low-pass filter is used with the disk recorder to minimize noise; the range resolution† is about 40 m, while that for the 35-mm film record is less than 20 m. The 35-mm film records were used for the manual analyses, while the machine analyses employed the magnetic disk records.

---

*MRV Corp. Model 100M.

†The range resolution as used here is defined as the minimum separation distance at which two individual targets can be resolved.

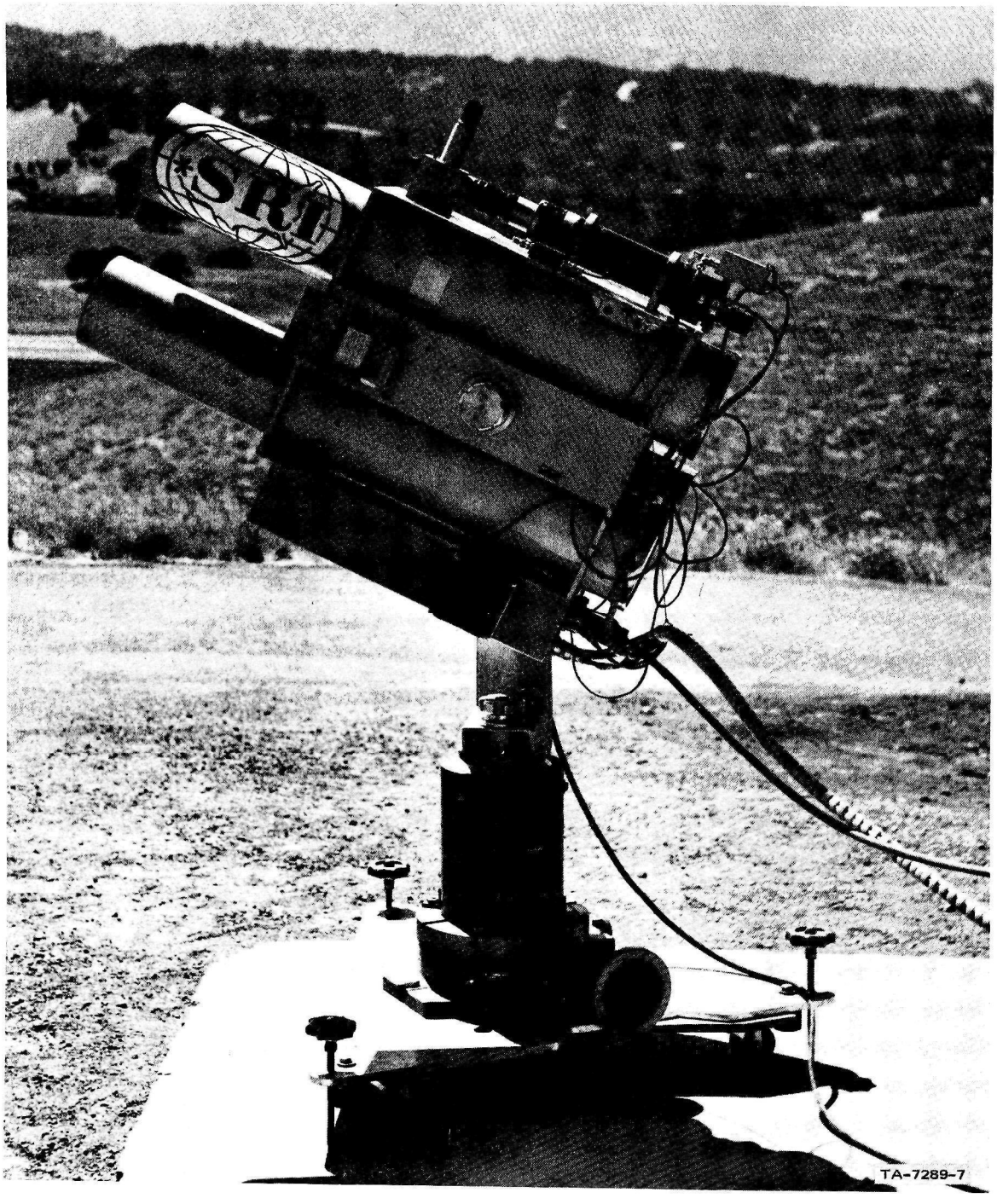

FIGURE 1 SRI MARK V LIDAR

B. Experimental Procedures

For each series of observations, the lidar was situated at any one of a number of preselected points, depending upon the location of the plume. The sites used during the two observation periods are depicted in Fig. 2. Where possible, the lidar was positioned so that it could be aimed in a direction approximately perpendicular to the plume axis. At each site, vertical cross sections through the plume were normally obtained at several downwind distances from the stack.* The technique employed consisted of scanning vertically with elevation angle increments of 0.3° to 10°, depending upon the vertical extent of the plume as determined from preliminary observations. Such scans were then repeated at other azimuth angles. The neodymium lidar permitted observations at intervals as short as five seconds. A complete vertical scan of 20 to 30 lidar shots required about two to five minutes to complete, and a set of three cross sections could be obtained within 10 to 15 minutes.

When the lidar was located at a considerable distance downwind from the stack, such as at Sites 16 (9 km), 17 (14 km), and 21 (21 km), the vertical cross sections were limited to only one azimuth angle (i.e., one vertical plane), because of the extended width of the plumes and the frequently directly overhead plumes.

In order to make the stack plume visible for direct observations with aircraft associated with other experiments, 50 percent of the electrostatic precipitators at Keystone Generating Station were normally shut down during most of the observations. However, to test the capability of the neodymium lidar to observe the "clean" plume, all of the precipitators were put into operation during certain periods on 21 and 22 October. As shown in Table I, six lidar plume cross sections were obtained under these conditions, and the results are presented in Sec. V.

---

*Although the Keystone Generating Station has two stacks, each 245 m high, only one stack was in operation during each of the observation periods.

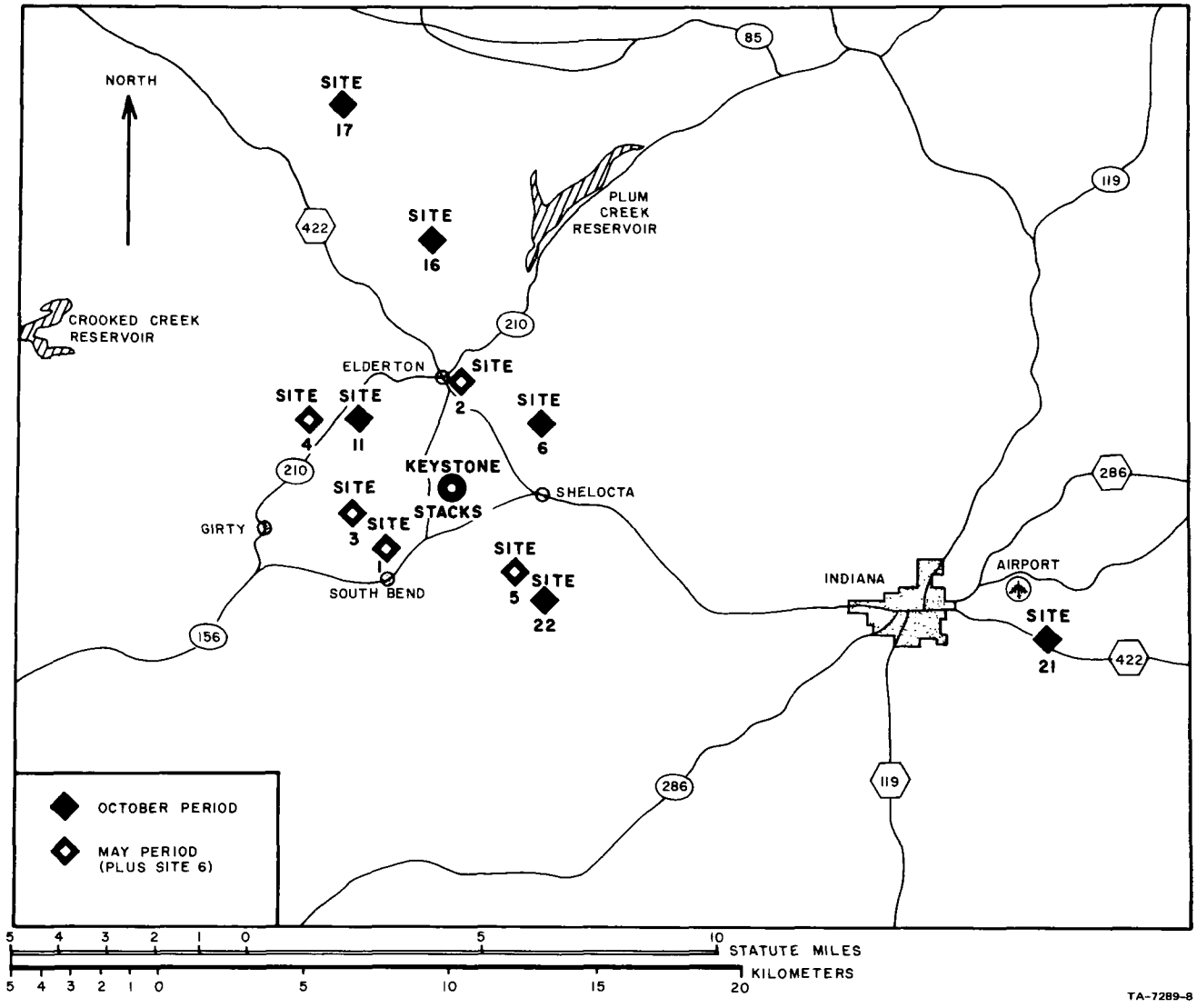

FIGURE 2 LIDAR SITES USED DURING FIELD EXPERIMENTS

Table I

KEYSTONE PRECIPITATOR CONDITIONS DURING LIDAR OBSERVATIONS OF PLUME (FROM SINGLE STACK)

(Precipitators on indicated by X)

Date (1968)	Lidar Cross Section Numbers	Bank 1								Bank 2							
		Inlet				Outlet				Inlet				Outlet			
		1	2	3	4	1	2	3	4	1	2	3	4	1	2	3	4
25 May	All	X	X	X	X	X	X	X	X								
26 May	All	X	X	X	X	X	X	X	X								
15 October	All	X	X	X	X	X	X	X	X								
16 October	All	X	X	X	X	X	X	X	X								
17 October	All	X	X	X	X	X	X	X	X								
18 October	All	X	X	X	X	X	X	X	X								
20 October	All	X	X	X	X	X	X	X	X								
21 October	46, 47, 48	X	X	X	X	X	X	X	X	X	X	X	X	X	X	X	X
	All Others	X	X	X	X	X	X	X	X								
22 October	60, 61, 62	X	X	X	X	X	X	X	X	X	X	X	X	X	X	X	X
	All Others	X	X	X	X	X	X	X	X								
23 October	All	X	X	X	X	X	X	X	X								
24 October	All	X	X	X	X	X	X	X	X	X				X			

The lidar observation periods were limited in length by prior arrangement in order to forestall any possible interference between the lidar and other experiments utilizing aircraft. One of the considerations here was lidar eye-safety, which is discussed in Appendix E.

C. Summary of Lidar Data

The lidar observations obtained during the two experimental periods, 25 May-1 June 1968 and 15-24 October 1968, are summarized in detail in Appendix B, and in condensed form in Table II, along with the distribution of the analytical effort among the data. Data obtained during several days during the May period when there was rain, low ceilings or fog have been omitted, since no analysis was attempted. Data obtained on occasions when the cooling tower plume merged with the smoke plume also were not analyzed.

Table II

CONDENSED DATA SUMMARY, LIDAR OBSERVATIONS

(For detailed summaries, see Appendix B)

Date (1968)	Time (EDT)	Site Number	Elevation (m)	Location from Stack	Number of Cross Sections		Analysis Method*	Remarks
					Observed	Analyzed		
25 May	0912-0925	1	329	3.5 km SW	3	3	M, C	Spatial
	1034-1048			(Az. 227°)	3	3	M	series
	1423-1453				4	0	--	
26 May	0854-0926	2	387	3.5 km N	6	3	M	Spatial
	1145-1208			(Az. 002°)	5	2	M	series
15 October	0932-1007	6	394	3.75 km NE	6	3	C	Time and
	1032-1150			(Az. 055°)	8	5	C	spatial series
16 October	0852-0946	16	418	8.50 km N	6	2	C	Plume
	1149-1206			(Az. 355°)	5	0	-- over	almost overhead
17 October	0903-0942	16	418	8.50 km N	5	2	C	Plume
	1151-1216			(Az. 355°)	3	0	--	overhead
18 October	0917-0944	17	448	13.7 km NNW (Az. 344°)	4	2	C	Plume overhead
20 October	0909-0941	21	448	21.1 km ESE	4	2	C	Plume
	1018-1040			(Az. 104°)	2	1	C	overhead
21 October	0854-0935	22	448	4.90 km SE	11	6	C	Dirty vs
	1023-1036			(Az. 120°)	3	3	C	clean plume
22 October	0900-0945	6	394	3.75 km NE	9	9	C	Dirty vs
	1134-1201			(Az. 055°)	6	0	--	clean
	1227-1245				6	3	C	plume
23 October	0850-0918	6	394	3.75 km NE	7	3	C	Time and
	0941-0949			(Az. 055°)	2	0	--	spatial
	1155-1227				5	0	--	series
24 October	0930-1204	11	418	3.95 km NW (Az. 306°)	19	12	C	Time series

*M--Manual Analysis, C--Computer Analysis.

IV BASIC ANALYSIS OF LIDAR BACKSCATTER SIGNATURES

A. General Discussion

An example of an oscilloscope photograph of a typical lidar shot recorded on the magnetic disk is given in Fig. 3. Here the magnitude of the backscattered signal return from the airborne aerosol is log-amplified and displayed on a logarithmic scale (in order to maintain a wide dynamic range of recording) versus time (or range) on a linear scale.

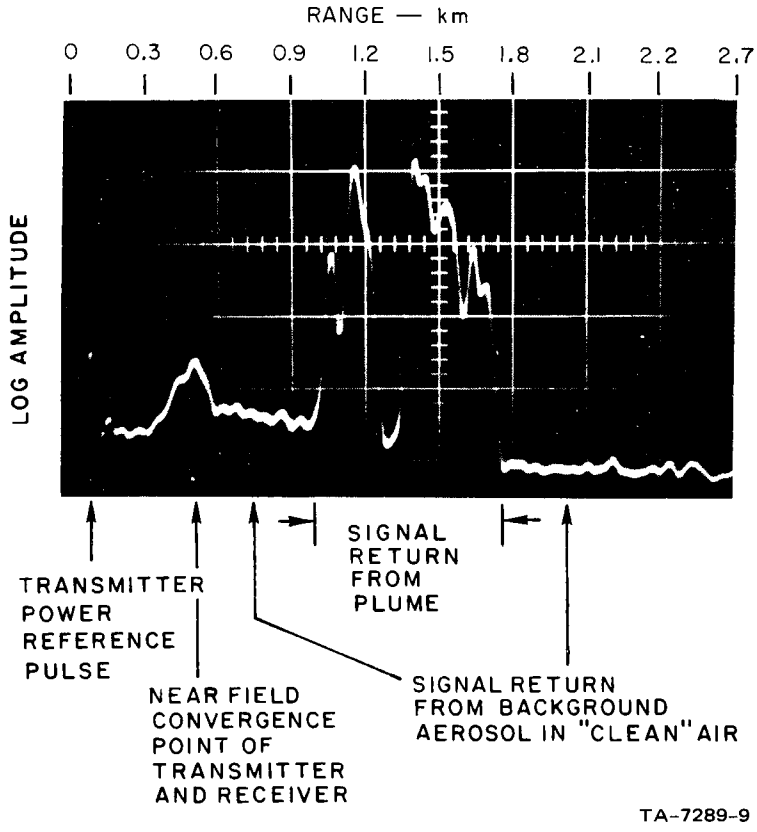

FIGURE 3 BASIC LIDAR OBSERVATION OF SMOKE PLUME

For inspection, inventory, and editing purposes, ten lidar observations are displayed simultaneously by the magnetic disk recorder, as shown in Fig. 4. One complete vertical "slice," or cross section, through the plume is represented by two to four of these ten-trace

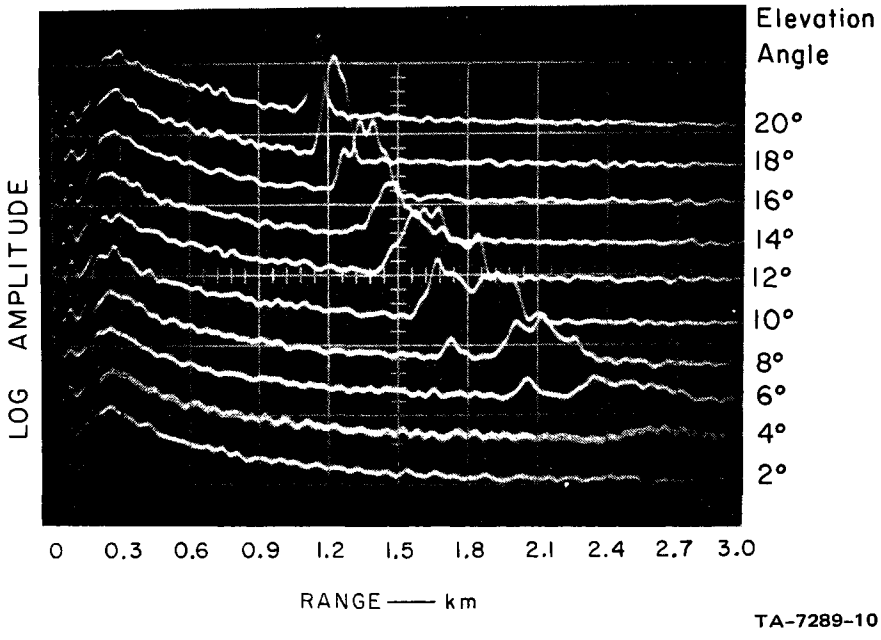

FIGURE 4 EXAMPLE OF MULTIPLE-TRACE FORMAT USED FOR EXAMINATION OF MAGNETIC DISK RECORDS

photographs. The "artificial" peak in the received signal at close range in Figs. 3 and 4 is typical of a bistatic system,* and is due to the oppositely acting effects of signal increase with increasing degree of intersection of the transmitter beam and receiver field of view, and signal drop-off due to increasing range (a function of the square of the range).

These traces represent the basic raw lidar data, which can be used directly to obtain plume boundaries easily and accurately. However, meaningful quantitative information on the concentration distribution within the plume requires further reduction and analysis. For each plume cross section consisting of 20 to 40 lidar observations, the data must be adjusted and corrected for:

(1) Range effect,

(2) Log-amplifier transfer function, and

(3) Pulse-to-pulse variations in transmitted power.

---

*Current lidars have separate, noncoaxial transmitter and receiver optics

Allowance for these factors is fairly straightforward, and results in a cross section of normalized signal return (S) values. These S-values are directly proportional to particulate mass concentrations (expressed in logarithmic units), if the particle size distribution and optical properties are spatially uniform, as is often a reasonable assumption (McCormick and Kurfis, 1966), and if attenuation is negligible. Correction for the attenuation effect requires considerable effort, and is detailed in Sec. VII.

Manual analysis was initially employed for the May data. Using a specially prepared gridded template, range-corrected values of signal return (in dB, relative to the background signal level from the ambient aerosol) were extracted from the 35-mm film record. These values were then corrected for the shot-to-shot variations in transmitted power, plotted, and the resulting cross sections analyzed by hand at a contour interval of 6 dB (representing an increase by a factor of four). In line with the preceding discussion, these S-contours represent (in logarithmic units) approximate relative mass concentrations within the plume.

These manual analyses are quite tedious, and an objective analysis procedure was developed to process the October data and to check the hand analyses of the May observations. This procedure is documented in Fig. 5 (and Appendix C) and is discussed below.

B. Lidar S-Function Analysis

The signal received on the face of the Mark V detector, originating from backscattered energy at range R, may be expressed as

$$P_s(R) = P_T \frac{c\tau}{2} \frac{A}{R^2} T_c(R)\ \beta(R)\ T^2(R) \qquad (1)$$

where

P_T = peak power emitted into the atmosphere

c = speed of light

τ = pulse duration

STEP 1—ANALOG-TO-DIGITAL CONVERSION

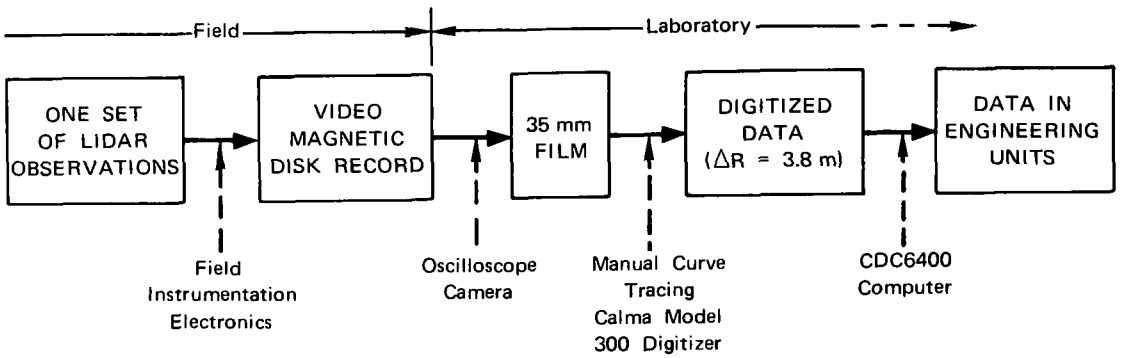

STEP 2—CONDITIONING, EDITING, AND BASIC ANALYSIS

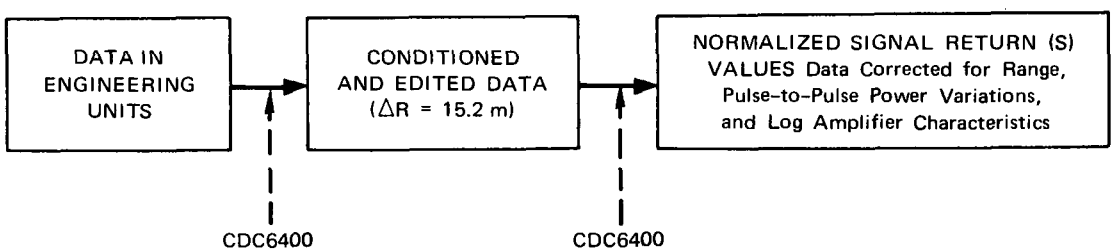

STEP 3—CONTOUR ANALYSIS AND ATTENUATION STUDY

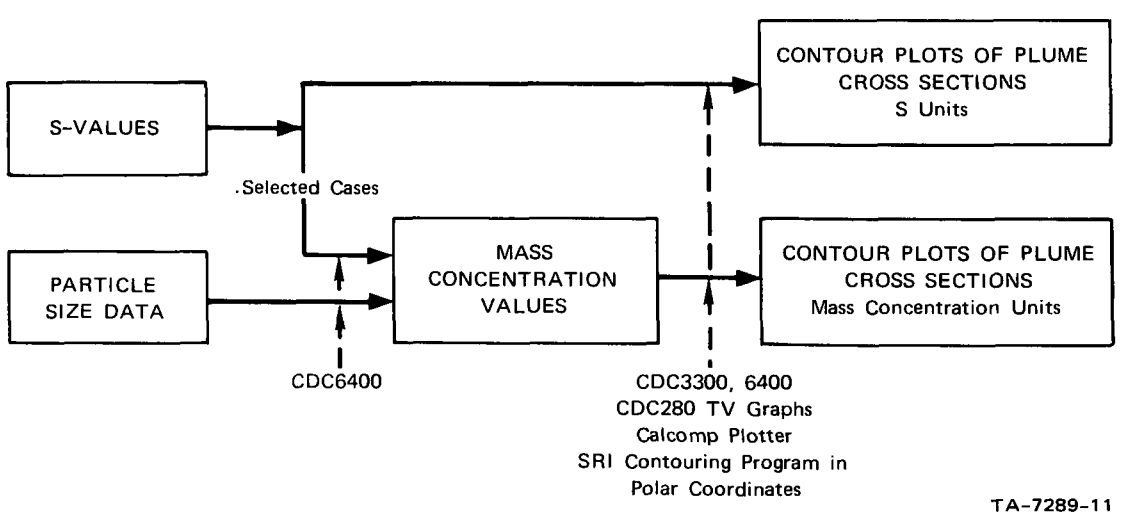

FIGURE 5 LIDAR DATA ANALYSIS PROCESS. See Appendix C for additional details on Steps 1 and 2.

A = effective receiver area

T_c = beam convergence factor

β = volume backscatter coefficient (per steradian)

T = atmospheric transmission factor.

As previously mentioned, the resulting detector signal was routed through a logarithmic (log) amplifier and recorded on a video magnetic disk, as well as on a backup 35-mm recording camera system.

All signal strengths were referenced to the detector level in the absence of the applied backscatter signal P_s, which is denoted by P_N. The atmospheric return level recorded on the disk may then be expressed (in decibel notation) as

$$H(R) = 10 \log^* \frac{P_s(R) + P_N}{P_N} \tag{2}$$

where $\log^*$ is the log amplifier transfer function, which differs slightly from the true log function. As indicated in Fig. 5 and detailed in Appendix C, the analysis phase was initiated by digitizing recorded H(R) traces, using a CALMA Model 300 digitizer. Intensity values at the digitizer standard increment (equivalent to 4 m) were recorded on magnetic tape. A CDC6400 computer was then employed to obtain a range-corrected, normalized signal return (S) function defined as

$$S(R) = 10 \log \frac{P_s(R)\, R^2}{P_s\left(R_o\right) R_o^2} \tag{3}$$

where R_o is a reference range [normally chosen as the first data point of the H(R) digitization], and $P_s \gg P_N$. This S function also incorporates a correction for the transfer function of the log amplifier.

From Eqs. (1) and (3), the normalized signal return function S(R) may be related to the atmospheric optical parameters by

$$S(R) = 10 \log \frac{\beta(R)\, T^2(R)}{\beta\left(R_o\right) T^2\left(R_o\right)} \quad , \tag{4}$$

where $T_c(R \geq R_o) = 1$ is assumed; i.e., the H(R) digitization process was initiated at a point on the trace for which the transmitted beam is fully encompassed by the diverging receiver field of view. The S function then represents a relative backscatter function, which is uncorrected for atmospheric transmission losses.

S-function contours were generated from a computer program (developed at Stanford Research Institute) that uses linear interpolation of data gridded in polar coordinates. The polar grid of data points need not be equal-incremented in range or angle, thus permitting processing of lidar data collected at unequal increments of elevation angle. The output from the contouring program was subsequently machine plotted on a Benson-Lehner or Calcomp plotter, or electronically graphed on the CDC280 CRT/film system. These contour plots and their significance are presented in Sec. V.

The lidar S function is dependent only on the atmospheric optical properties when $P_s(R) \gg P_N$. However, when $P_s(R) \leq P_N$ (i.e., when the atmospheric return is at or below the noise level), then $S(R) \propto 10 \log R^2$. Invalid data of this type were omitted from the contouring program. This omission, illustrated in Fig. 6, explains the open contours that may be expected when plume return occurs at a range for which the clear-air return would be below the noise level. While the S-function contour analyses give a surprisingly good picture of plume relative concentration distributions from laser energy returns (see Fig. 23), they are biased to varying degrees by the fact that some energy is lost from the laser pulse as a function of distance along the path, i.e., the atmospheric transmission of the laser energy varies along the pulse path. Accounting for this attenuation effect requires additional information on the atmospheric scattering particles and/or an explicit relationship between the atmospheric transmission and backscatter properties at the laser wavelength. This aspect of the analysis is discussed further in Sec. VII.

Since plume mass concentrations--and thus lidar echoes--cover such a wide dynamic range, contouring a plume cross section in linear units presents a problem. As illustrated in Fig. 7, the linear display (a)

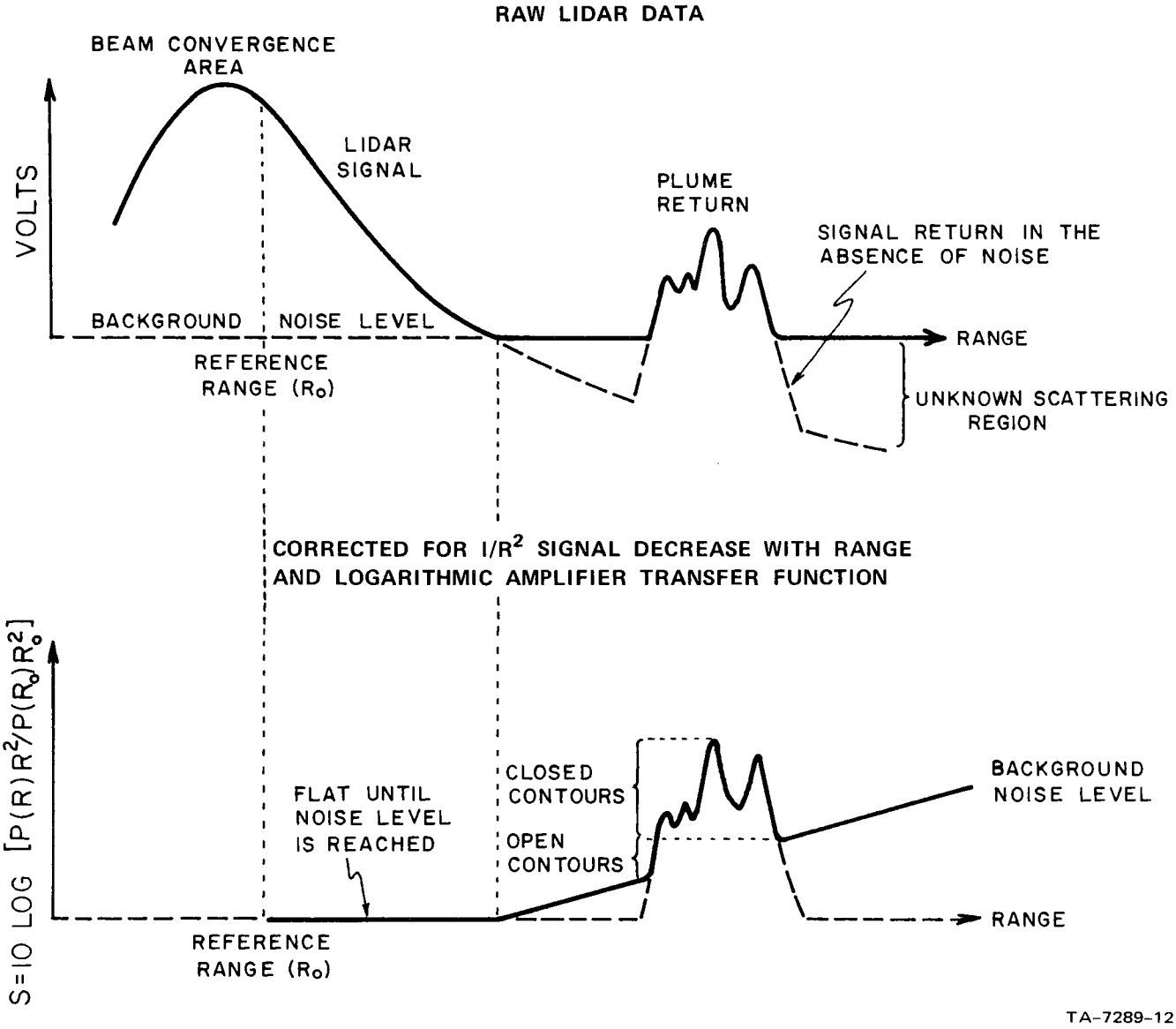

FIGURE 6 EFFECT OF RANGE CORRECTION UPON PLUME SIGNAL RETURN AND RECEIVER NOISE LEVEL. For simplicity, a perfectly transmitting homogeneous medium has been assumed for the clear air.

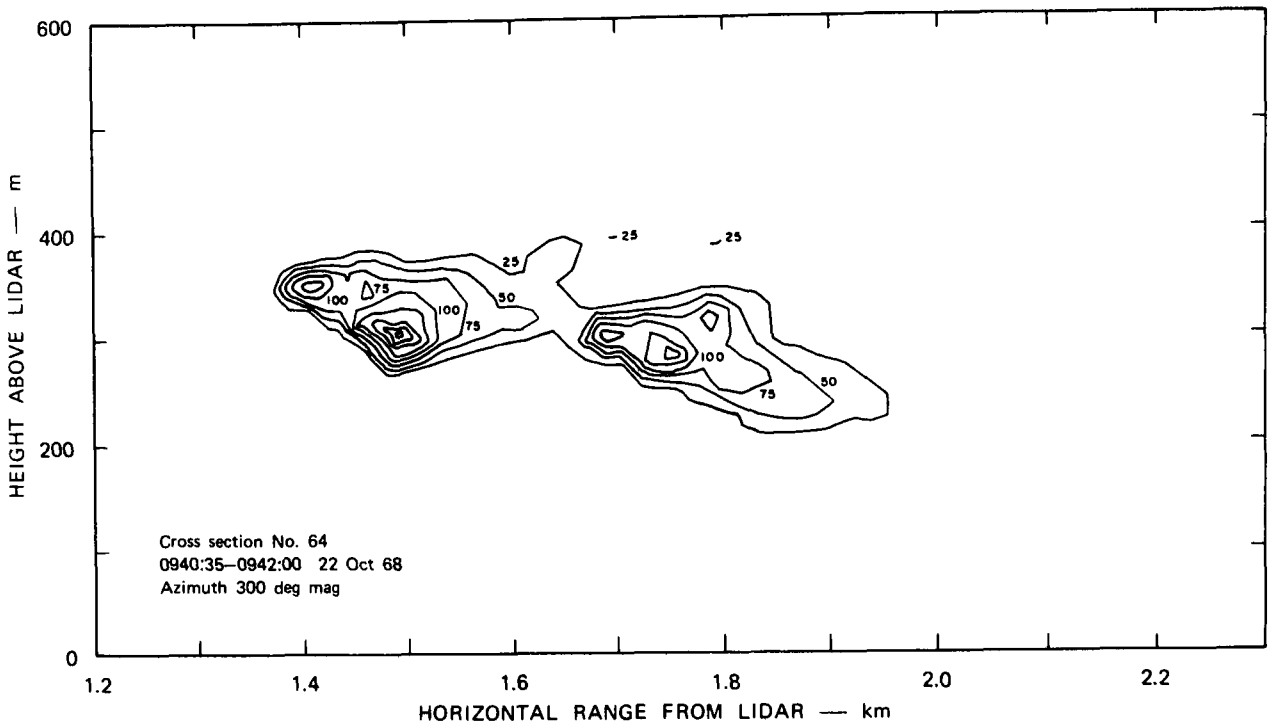

(a) Linear display—M/M_0—contour interval 25

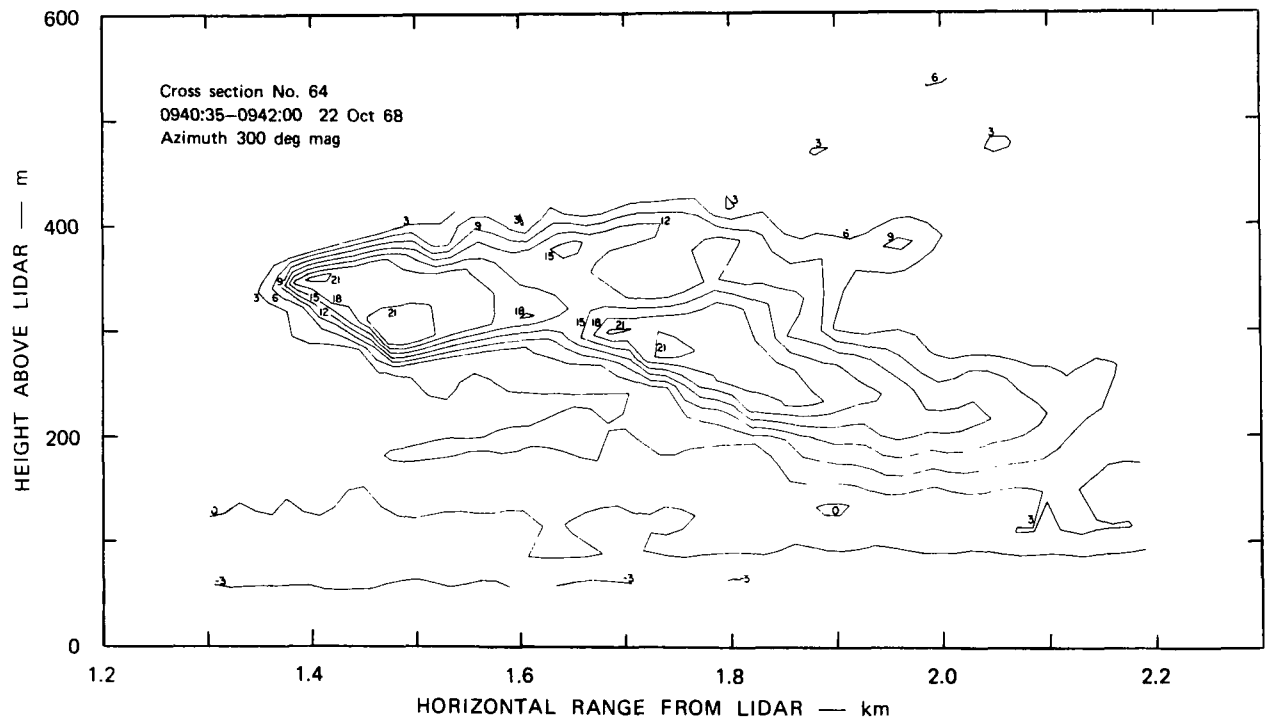

(b) Logarithmic display—10 $\log_{10}$ (M/M_0) — contour interval 3 db

TA-7289-13

FIGURE 7 COMPARISON OF PLUME CROSS SECTIONS CONTOURED IN LINEAR UNITS (a) AND LOGARITHMIC UNITS (b)

loses definition at the boundary of the plume, compared with a logarithmic display (b) with contours in decibels. The latter documents the plume edge more accurately, and permits reasonable contour spacing.

In the linear display in the figure, the contour units are in multiples of the clean-air background mass concentration (M_o), or M/M_o, where M is the plume mass concentration. [For this case, M_o was taken to be 100 $\mu g/m^3$, on the basis of the visibility estimate and the work of Noll, et al. (1968).] It may be seen that the contour spacing, and thus the outer contour value, must be set at no lower than about 25 in order to prevent contour crowding. On the other hand, the logarithmic display with units of dB = 10 $\log_{10}$ (M/M_o) has a contour spacing of 3 dB, which gives an outer boundary of $M/M_o \approx 2$ without excessive contour crowding. (Each contour increment of 3 dB corresponds to a change by a factor of approximately two from the adjacent contours.) Because of these advantages, logarithmic contour intervals have been used exclusively in the lidar cross sections.

Because of the effect of the finite above-noise range of the lidar as explained in Fig. 6, many contours in the cross sections to follow later do not close around the plume; with increasing range they begin contouring the background noise and become meaningless. In addition, contours frequently appear in the clear air beneath the plume, which are usually probably real, but have no particular value. Both of these effects are shown in Fig. 7(b). To add clarity to the plume cross sections, these extraneous portions of the contours have been deleted from the illustrations. Figure 33 in Sec. VIII shows the nature of this editing process. Considerable care was taken to ensure that this process did not remove any portion of the plume cross section or any other information of value.

V RELATIVE CONCENTRATION CROSS SECTIONS OF KEYSTONE STACK PLUME

A. May 1968 Observation Period

The emphasis during the May observation period was on lidar plume observations within five miles (8 km) of the stack. The analyses for the May data were performed manually. All lidar observations during this period were taken when one of the two precipitator banks for the active stack was shut down, allowing 50 percent of the effluent to pass out through the stack untreated. The resulting plume color was a light gray-brown.

In the plume cross section illustrations to follow, both for the May and October data, it should be noted that the lidar is at the point (0,0), and the horizontal range scale is usually discontinuous. Also, heights are taken above the lidar; Fig. 8 illustrates the height relationships involved. To facilitate height transformations, the height of the top of the stack is indicated on the ordinate scale for each cross section by means of a horizontal arrow. (Lidar site elevations are given in Table II, Sec. III.) Calculated plume rise heights (ΔH) are also shown for those cross sections for which reasonably concurrent temperature profiles were available, and will be discussed in Sec. VI.

Figures 9-12 show four sets of sequential vertical cross sections through the smoke plume during the mornings of 25 May (Figs. 9 and 10) and 26 May (Figs. 11 and 12). The contours in Figs. 9 through 12 represent range-corrected signal return in decibels relative to that from the ambient background aerosol, including background noise, and can be taken to represent (approximately) the relative particulate concentrations. The effects of attenuation are neglected. The inset in each figure indicates the geometry of the observations. Poor weather conditions prevailed during the 43 cross sections obtained during the remainder of the May period. The cross sections in Fig. 9 were obtained about 1-1/2 hours earlier than those in Fig. 10, while the observations in Fig. 11 precede those in Fig. 12 by almost three hours. Vertical temperature profiles closest in time

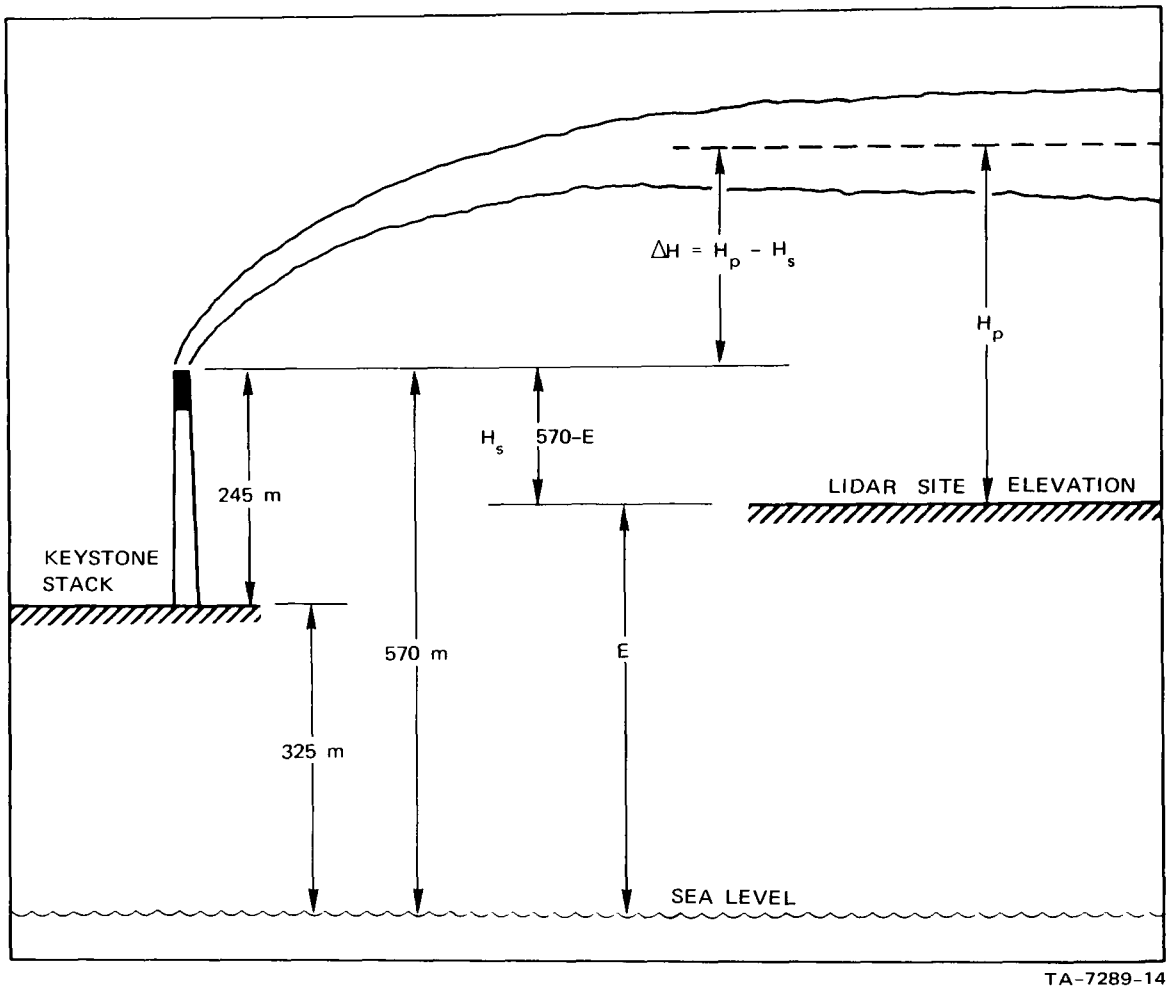

FIGURE 8 RELATIVE HEIGHT CONSIDERATIONS ASSOCIATED WITH LIDAR PLUME OBSERVATIONS. Lidar site elevations, E, are given in Table II; values of H_s are indicated on each plume cross section.

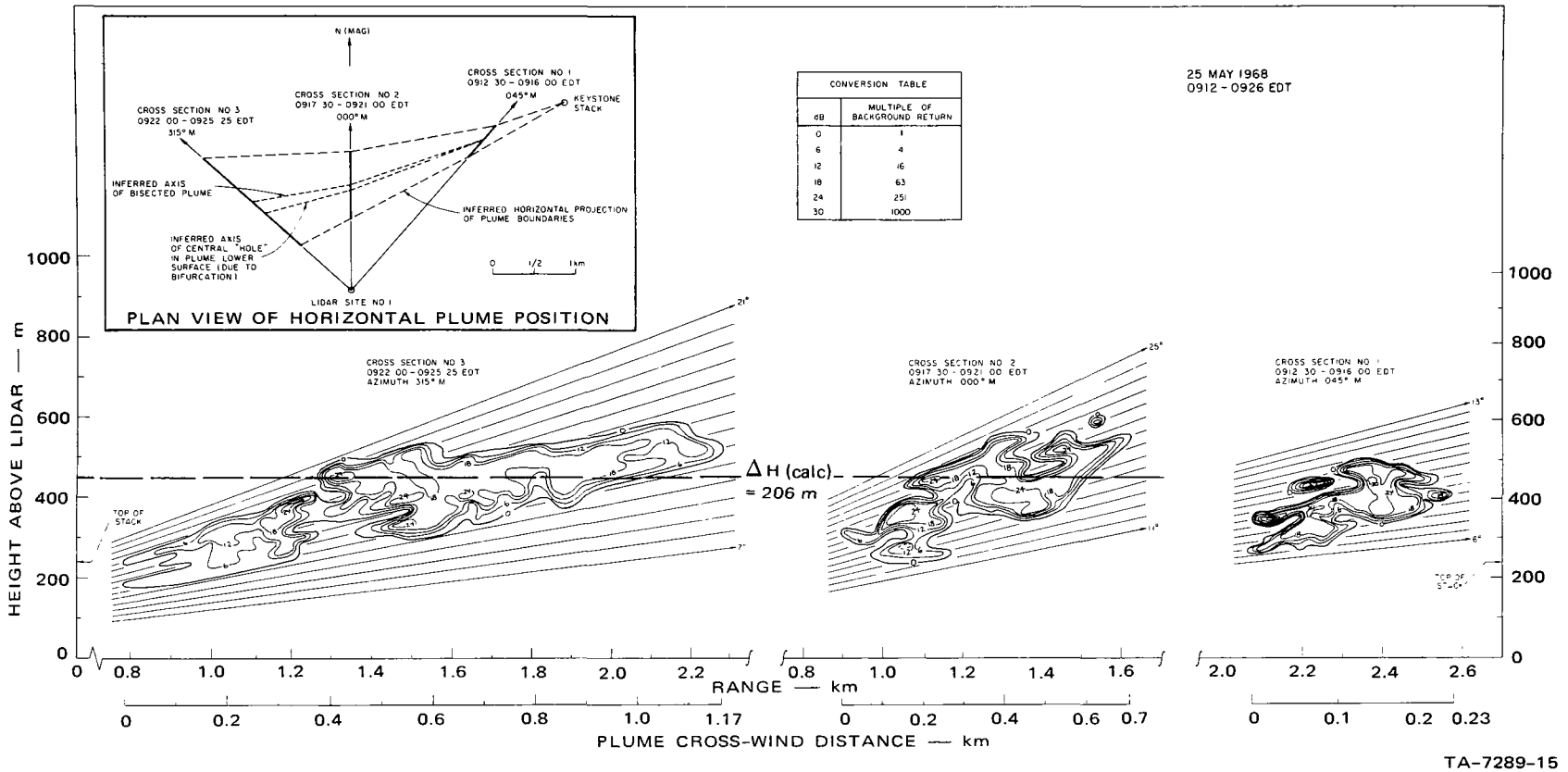

FIGURE 9 SPATIAL SERIES OF LIDAR-OBSERVED VERTICAL CROSS SECTIONS UNDER STABLE CONDITIONS, 25 MAY 1968, FROM SITE 1, 3.5 km FROM STACK. The contours represent range-corrected signal return in decibels relative to that from the ambient background aerosol, including background noise, and can be taken to approximately represent relative particulate concentrations. Attenuation has been neglected. See inset for horizontal positions of cross sections.

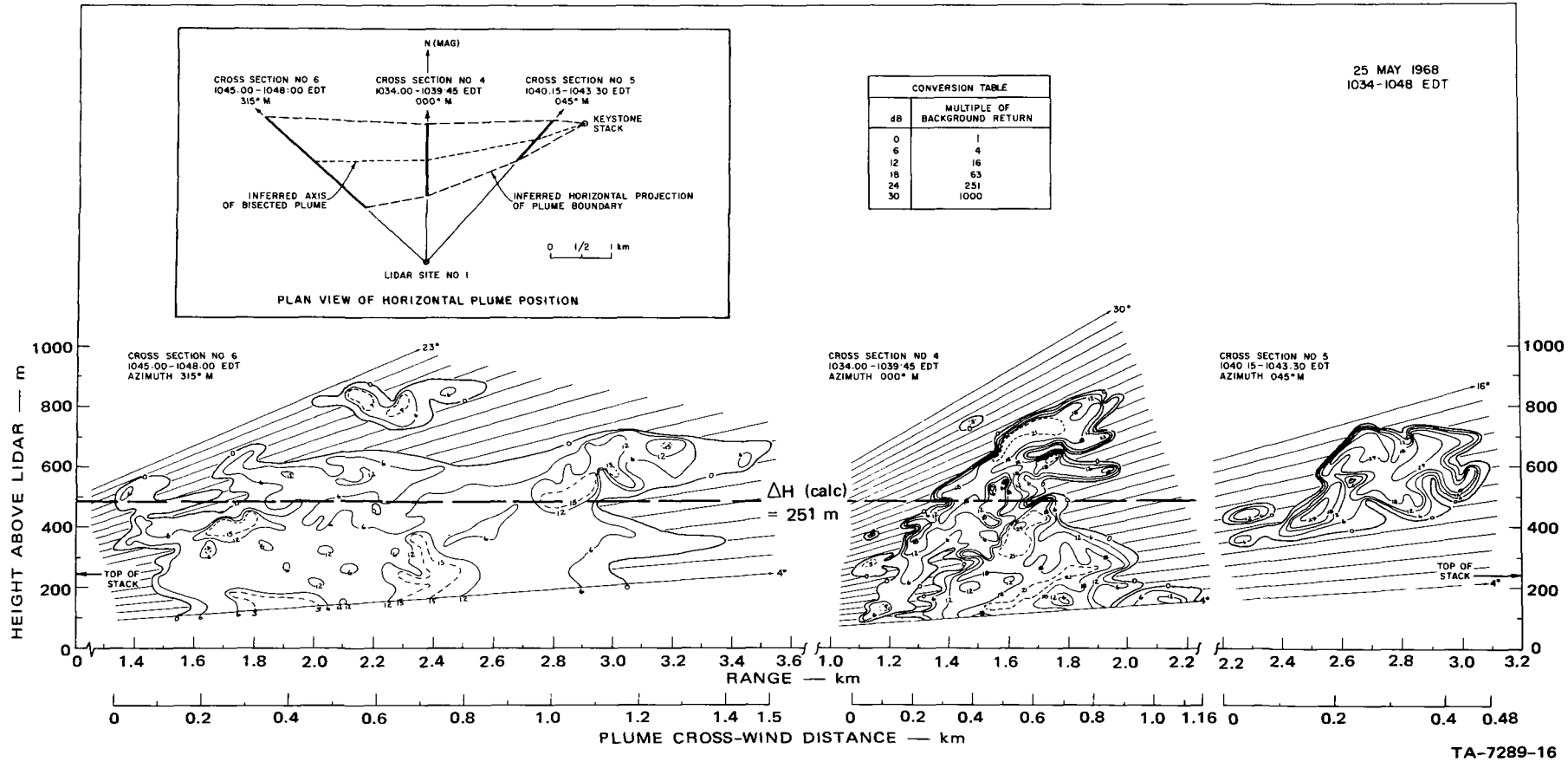

FIGURE 10 SPATIAL SERIES OF LIDAR-OBSERVED VERTICAL CROSS SECTIONS UNDER MODERATE DIFFUSION CONDITIONS, 25 MAY 1968, FROM SITE 1, 3.5 km SOUTHWEST OF STACK

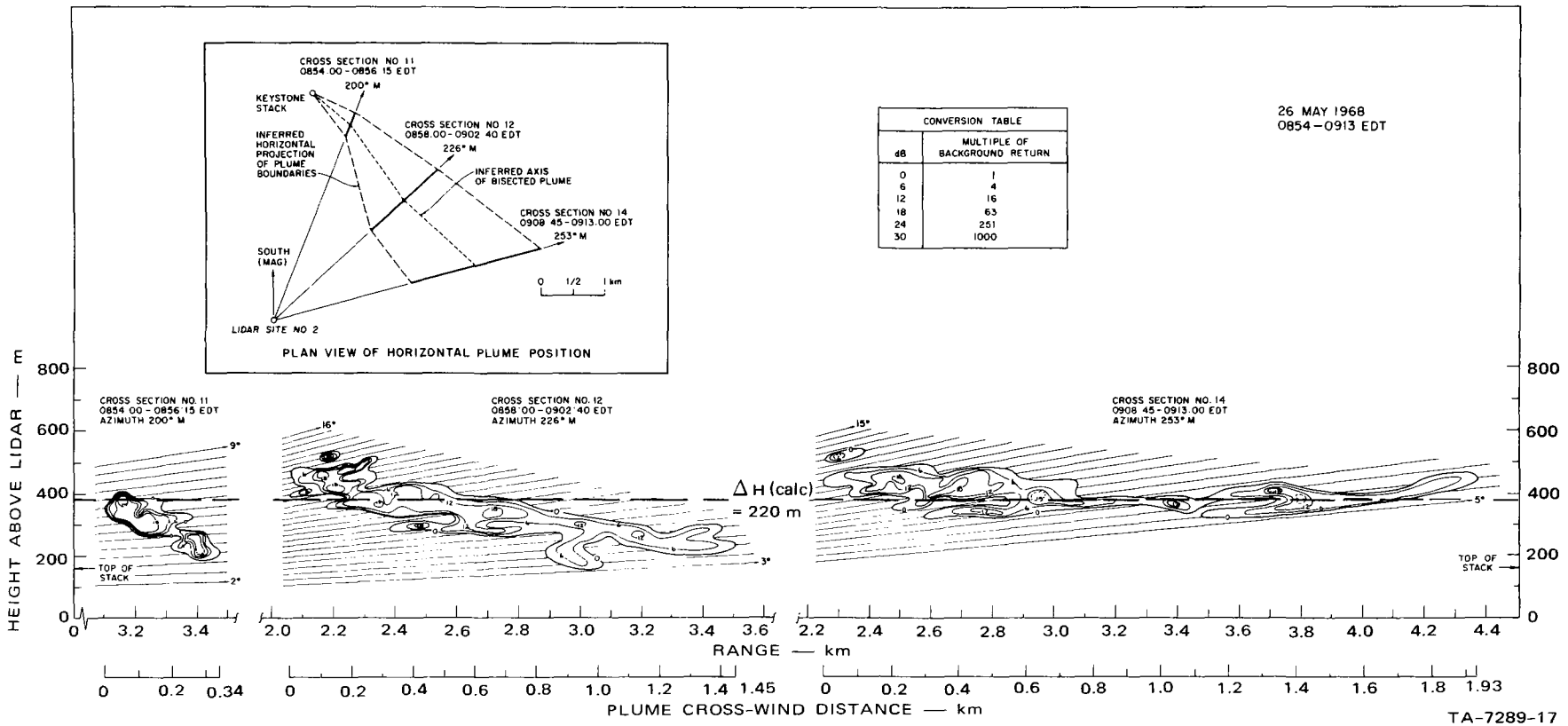

FIGURE 11 SPATIAL SERIES OF LIDAR-OBSERVED VERTICAL CROSS SECTIONS UNDER STABLE CONDITIONS, 25 MAY 1968, FROM SITE 2, 3.5 km NORTH OF STACK

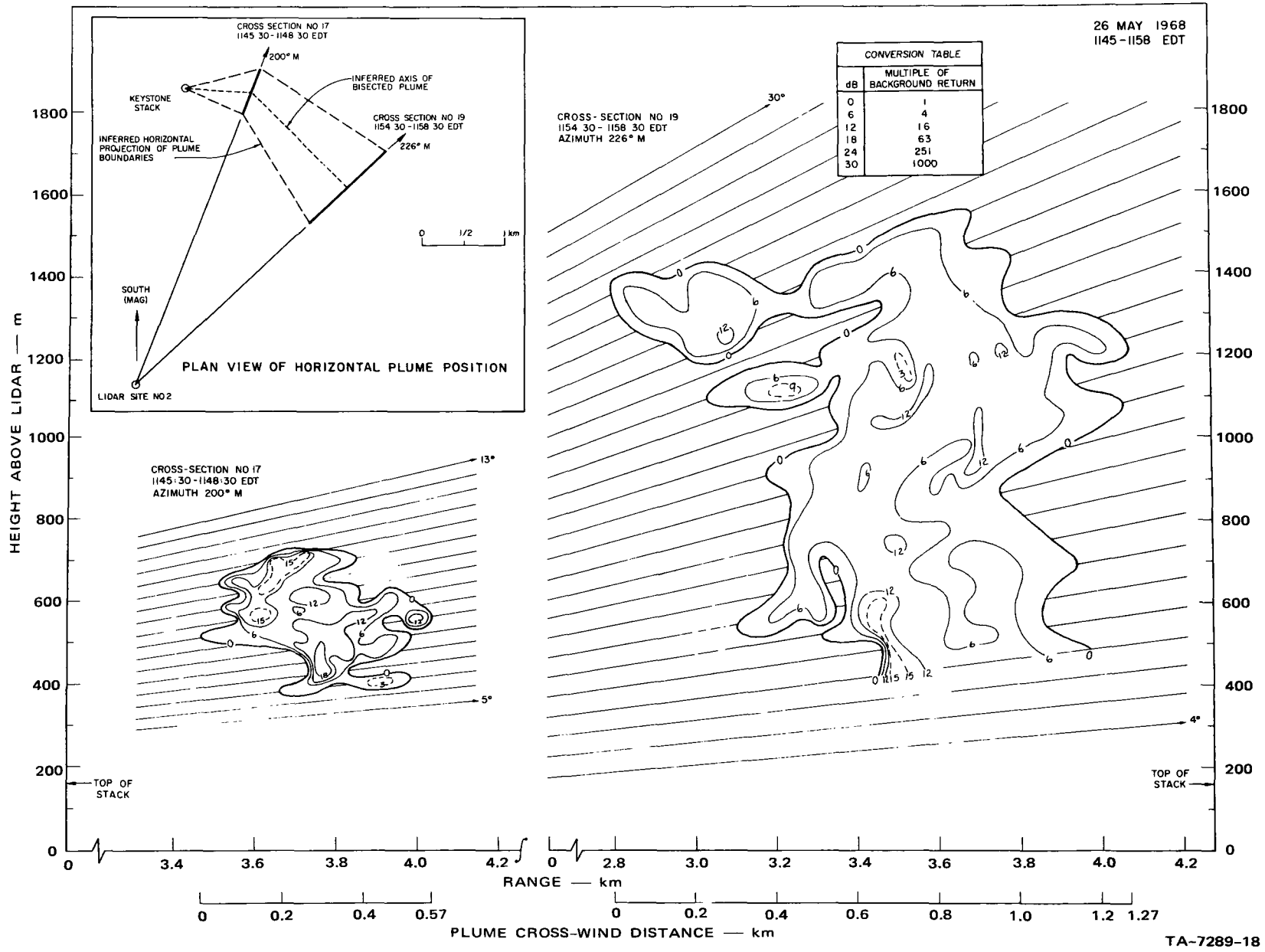

FIGURE 12 SPATIAL SERIES OF LIDAR-OBSERVED VERTICAL CROSS SECTIONS UNSTABLE (LOOPING) CONDITIONS, 26 MAY 1968, FROM SITE 2, 3.5 km NORTH OF STACK

to the lidar cross sections are given in Fig. 13. On both mornings, the sky was essentially clear.

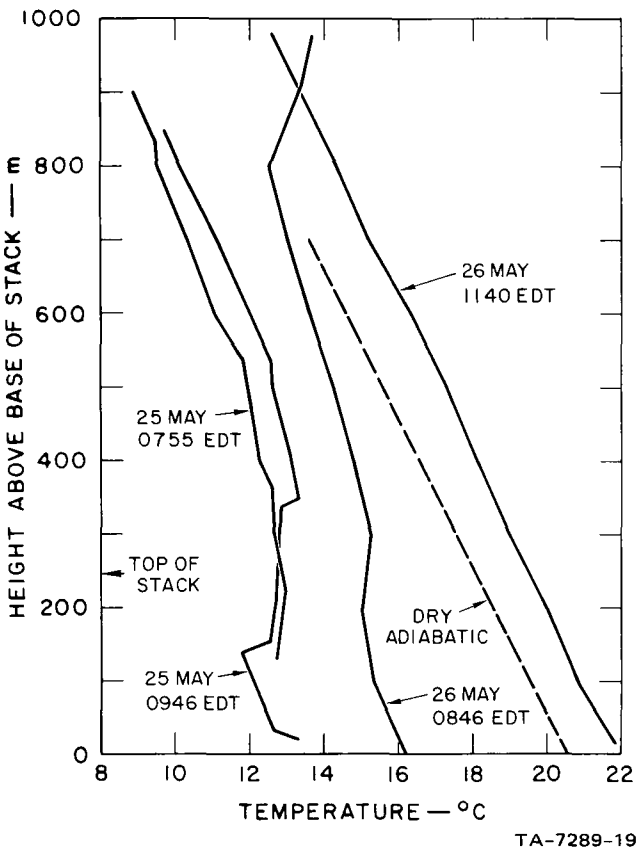

FIGURE 13 VERTICAL TEMPERATURE PROFILES ASSOCIATED WITH LIDAR OBSERVATIONS, 25–25 MAY 1968

Several general features of these cross sections are apparent. The contours, which are in logarithmic units (decibels), represent approximate relative particulate mass concentrations as previously discussed. Maximum concentrations are usually observed near the top of the plume, apparently associated with the greater buoyancy there. This effect was also found by Hamilton (1966), who took ruby-lidar observations of the plume from an oil-fired power plant. There is considerably consistency in the observed shape and structure of the Keystone plume from cross section to cross section in each set, and individual features may be followed for several kilometers downwind from the stack. This is particularly pronounced for the early-morning, nondiffusive cases. For

example, in Fig. 9, the central clear cavity, or vault, on the bottom of the plume, evidently associated with the bifurcation process, is readily apparent in all three cross sections.

For the stable cases (Figs. 9 and 11), the characteristic horizontal spreading (fanning) and tilting of the plume due to vertical wind direction shear (wind veering with height) is evident.

In Fig. 11, there is some evidence that terrain channeling of the air flow acted to horizontally spread the effluent, in addition to the effects of wind direction shear. The northeastern portion of the plume (nearest the lidar) appears to follow a valley that is about 100 m lower than the hills which are traversed by the southwestern portion of the plume (farthest from the lidar), possibly accounting for part of the rapid increase in the cross-wind (or cross-axis) dimension* of the plume from 340 m at 0.8 km downwind to 1450 m at a downwind distance of 2.2 km. Lifting by the hills could explain the 160-m rise of the southwestern portion of the plume (at the extreme right in Fig. 11) from Cross Section 12 to Cross Section 14.

The cross sections pictured in Fig. 10 probably represent a case of fumigation, in that downward diffusion is fairly strong, while upward diffusion of the plume apparently is limited. This situation could be caused by a temperature inversion at 900-1000 m, above the maximum height of the observed temperature profile. Note that relatively high concentrations are brought to very low levels within 3 km from the stack.

The rapid upward diffusion of a looping plume is illustrated in Fig. 12. For the most part, the relative concentrations in Cross Section 19 are less than those in Cross Section 17 by about 6 dB, which represents a decrease to about one quarter of the previous levels. The temperature sounding for this time (Fig. 13) shows an approximately dry-adiabatic lapse rate up to the maximum height sampled, 1000 m above the base of the stack.

---

*This dimension is indicated on the secondary abscissa scale for each cross section during the May period.

Since these cross sections were built up from lidar observations spanning a period of two to five minutes, some distortion is unavoidable when the plume structure is changing with time, as during unstable conditions (Figs. 10 and 12). In the future, lidar systems capable of one or two pulses per second and with automatic positioning should eliminate such problems by furnishing essentially instantaneous plume "slices."

B. October 1968 Observation Period

Due to the large quantity of lidar data obtained during this period, an objective, computer-oriented data reduction and analysis process was developed, as described in Sec. IV. This process permitted the analysis of about half of the cross sections observed. A number of illustrative examples have been selected for presentation here. There are various minor flaws in these analyses that would not have occurred if the work had been carried out by hand, but the time saving is quite significant.

For example, occasional small areas of the cross sections (indicated in the figures) were not contoured due to a minor program error. In addition, the cross sections illustrated do not always represent the total plume width as recorded on the original data records (photographs), although the portion shown is correct. This truncation occurred because of a problem in digitizing and processing those photographs that were obtained with an oscilloscope sweep speed of 5 μs/cm, corresponding to a full-scale range of 7.5 km.

Because of this difficulty, which could not be overcome within the time and effort limitations of the project, the photographs taken at 2 μs/cm were used exclusively, which limits the ranges of the analyzed data to 3-km maximum. In order to retain the information on total horizontal plume extent, maximum distances of plume return were scaled off the original 35-mm film and are indicated on the figures by vertical arrows (horizontal arrows when off scale) labeled with the range to the farthest observed edge of the plume.

Several of the May (hand-prepared) cross sections were reanalyzed by machine for comparison purposes. An example is given in Fig. 14. The agreement is good, despite the fact that two different data records

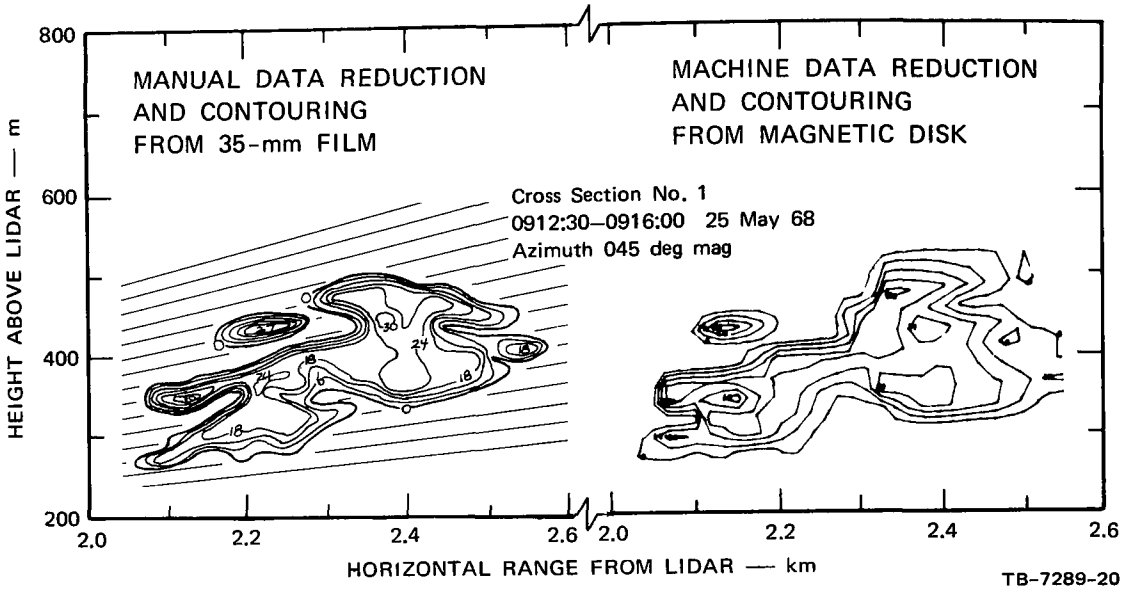

FIGURE 14 COMPARISON OF MANUAL AND MACHINE ANALYSES. Note that two different records are used, with the 35-mm film having considerably better spatial resolution than the magnetic disk. One lidar observation is missing at the top of the machine cross section.

were used: the 35-mm film (spatial resolution about 20 m), and the magnetic disk (spatial resolution about 40 m). In addition, it was later discovered that some data (the uppermost lidar observation) was missing from the disk record; this caused the shape of the machine cross section to differ at the top of the plume from that in the manual analysis.

The cross sections in Fig. 15 are in the same (approximately crosswind) vertical plane at the same azimuth angle from the lidar, and are spaced about one hour apart; thus, they document the changing crosswind structure of the plume with time during the morning of 15 October. The direction to the stack is into the paper. (See Appendix D for plan views of the horizontal plume positions, to clarify visualization of the lidar/stack/plume orientation.) The typical tilting and fanning of the plume in stable conditions, due to veering (clockwise rotation) of the wind direction with height, is apparent. By 1147 EDT, the height of the mixed layer had apparently increased to the level of the lower part of the plume, causing fumigation of that portion. Unfortunately, no temperature profiles are available for this day.

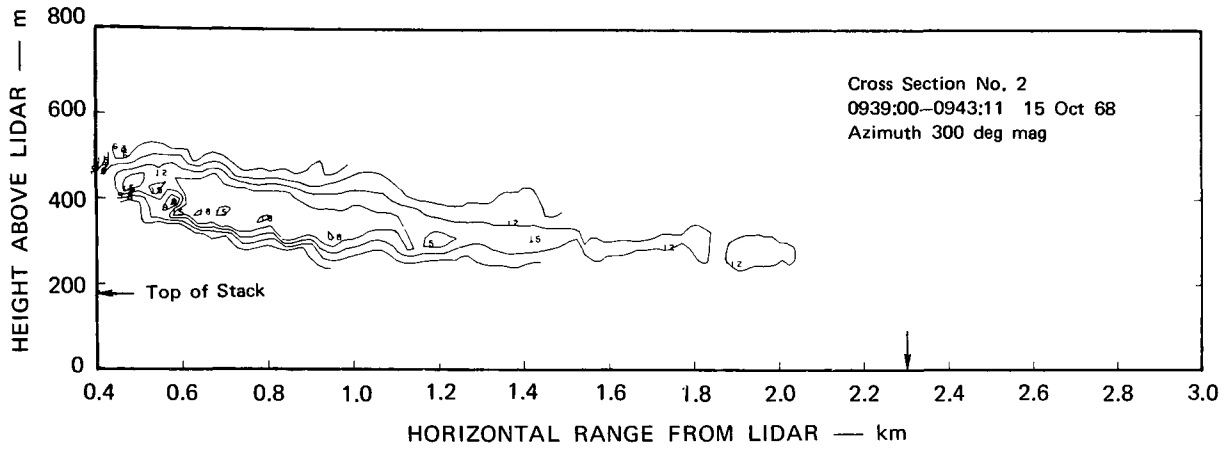

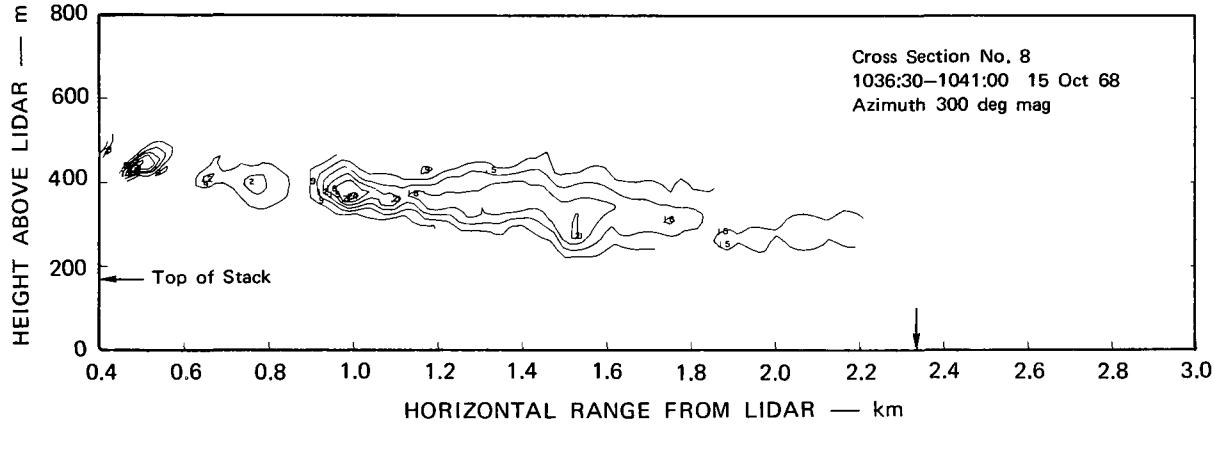

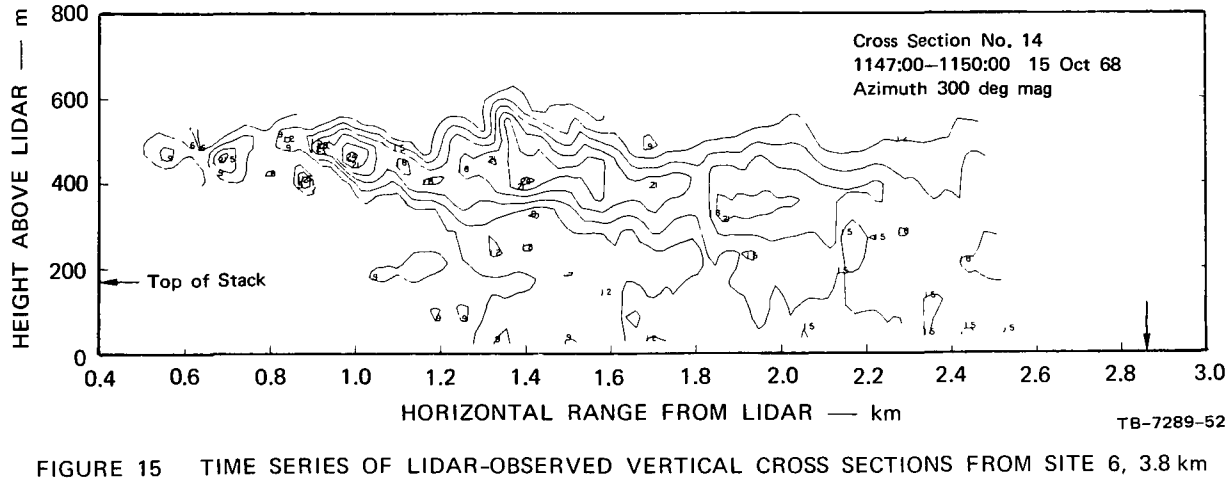

FIGURE 15 TIME SERIES OF LIDAR-OBSERVED VERTICAL CROSS SECTIONS FROM SITE 6, 3.8 km NORTHEAST OF STACK, PLUME OVERHEAD, 15 OCTOBER 1968. All times EDT. Lidar is located at Point (0,0). Horizontal arrows represent height of stack; vertical arrows represent horizontal extent of plume as indicated by original record. See also Figure D-1.

Figures 16-18 illustrate the large plume widths at 8.5 and 14 km downwind caused by stratification and fanning of the plume during the early morning hours of 16-18 October, respectively. The "lumps" appearing in these cross sections (and in those of other stratified plumes) are caused by a bias effect in the computer contouring program* due to the particular gridding technique used. This bias effect only occurs for very shallow plumes. The vertical plane covered here is directly over the lidar.

The plume cross sections in Fig. 19 are the farthest downwind (21 km) that were observed during the experimental program. These cross sections are in a vertical plane directly over the lidar. Of special interest here is Cross Section 42, which shows no plume, but does show the haze top associated with the temperature inversion. Evidently the tenuous plume either meandered away or lost its identity by mixing downward.

Figures 20 and 21 illustrate the effect on plume density of all precipitators being in operation (Fig. 21) compared with 50-percent operation (Fig. 20 and others). In each figure, the cross sections are at different azimuth angles and thus different downwind distances from the plume. Cross Sections A44 and 46 are about 3.5 km downwind, Cross Sections B44 and 47, 4.5 km downwind (and approximately crosswind), and Cross Sections 45 and 48 are 6 km downwind. (It should be kept in mind that as illustrated in Appendix D, these cross sections are sometimes elongated and do not represent true plume width, except when oriented in the crosswind direction. Plume height, however, is always truly represented.)

Examining Cross Sections B44 (Fig. 20) and 47 (Fig. 21), the dirty and clean plume, respectively, we see that the maximum normalized signal return above the reference for the clean plume is 12 dB, which is 6 dB, or four times, lower than that for the dirty plume. The apparent size of the plume, as observed by the lidar, also shrinks, due to less of the plume return being above the receiver noise level (see Fig. 6, Sec. IV).

---

*The contouring program, developed recently by S. Briggs of SRI, was used in its available form for this work. This bias effect, as well as the cause for the contouring skips, could be eliminated from the program in future studies.

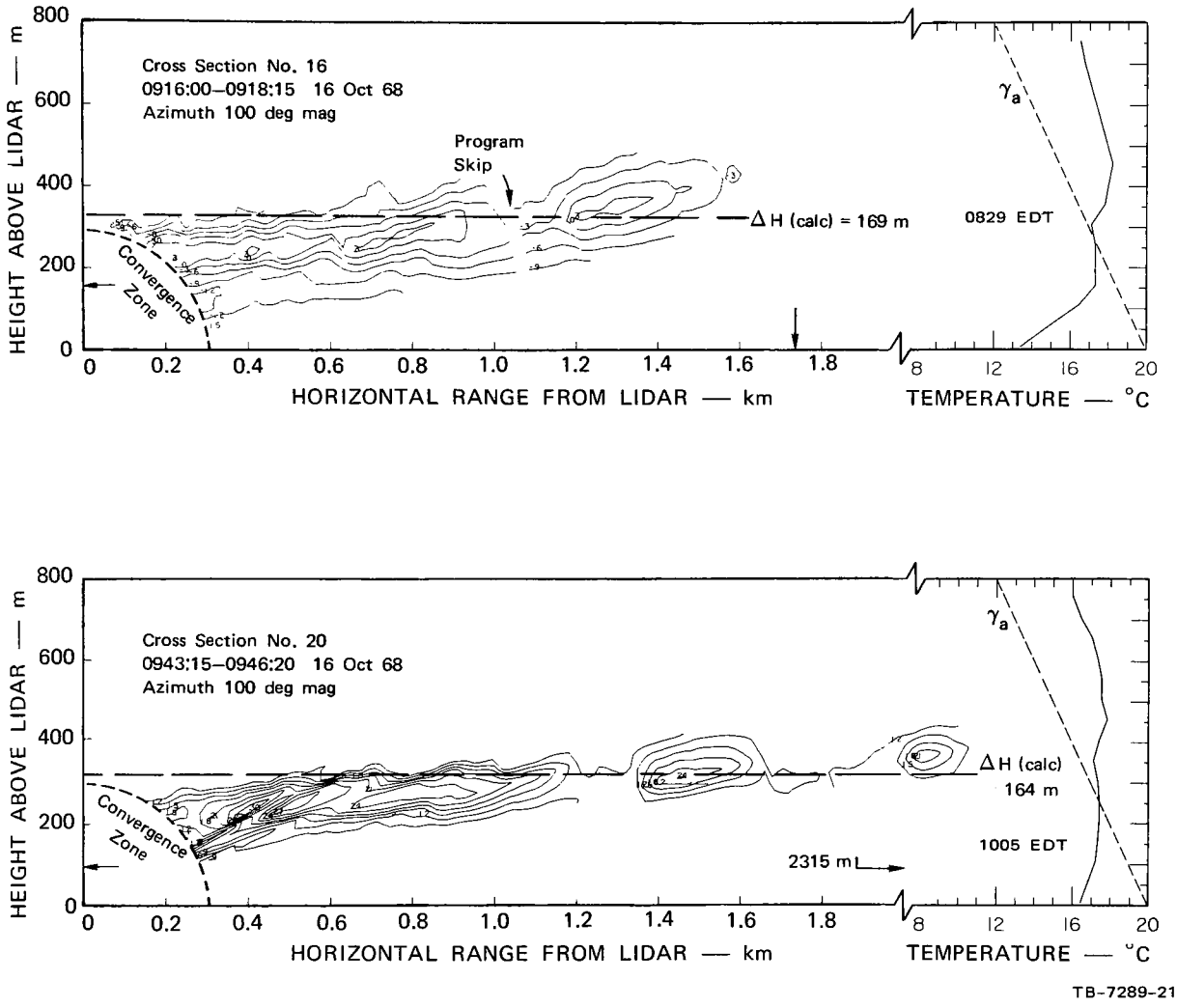

FIGURE 16 TIME SERIES OF LIDAR-OBSERVED VERTICAL CROSS SECTIONS FROM SITE 6, 3.8 km NORTHEAST OF STACK, PLUME OVERHEAD, 16 OCTOBER 1968. See also Figure D-2. Calculated plume-rise heights (ΔH) are shown as dashed lines.

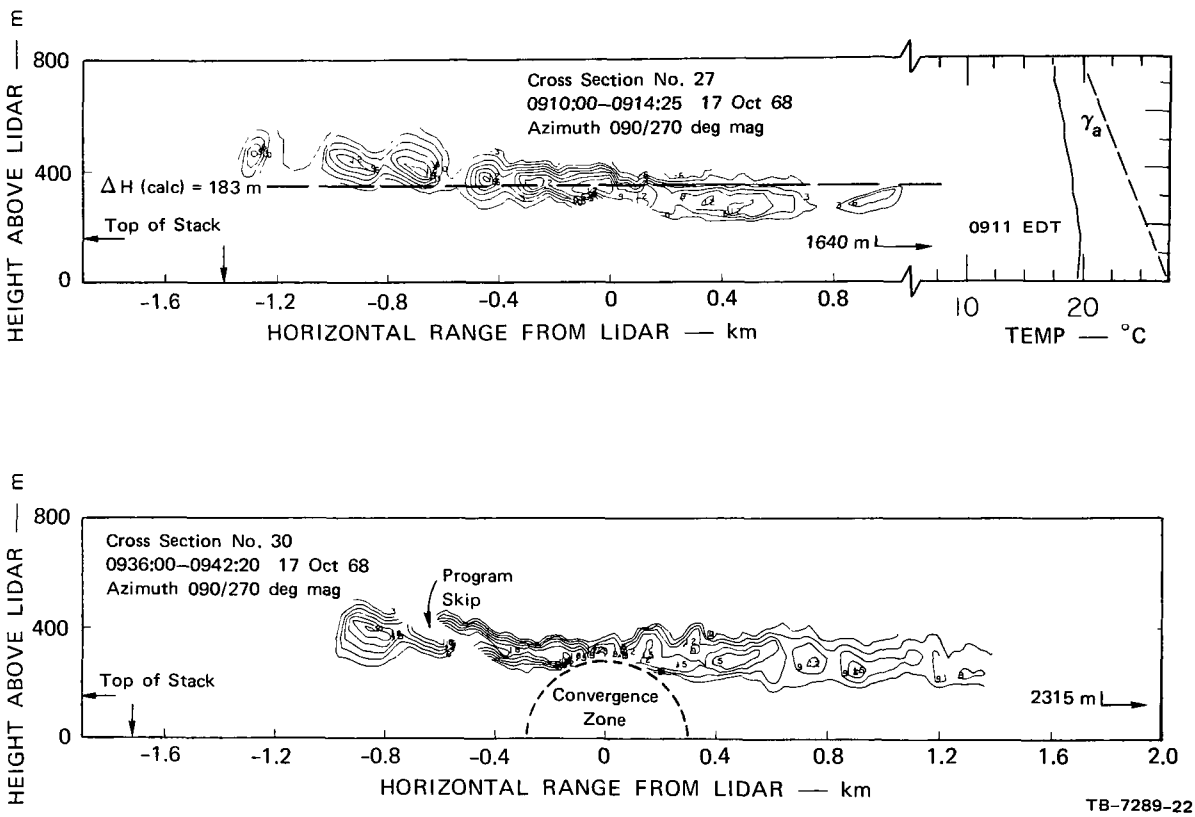

FIGURE 17 TIME SERIES OF LIDAR-OBSERVED VERTICAL CROSS SECTIONS FROM SITE 6, 3.8 km NORTHEAST OF STACK, PLUME OVERHEAD, 17 OCTOBER 1968. See also Figure D-3.

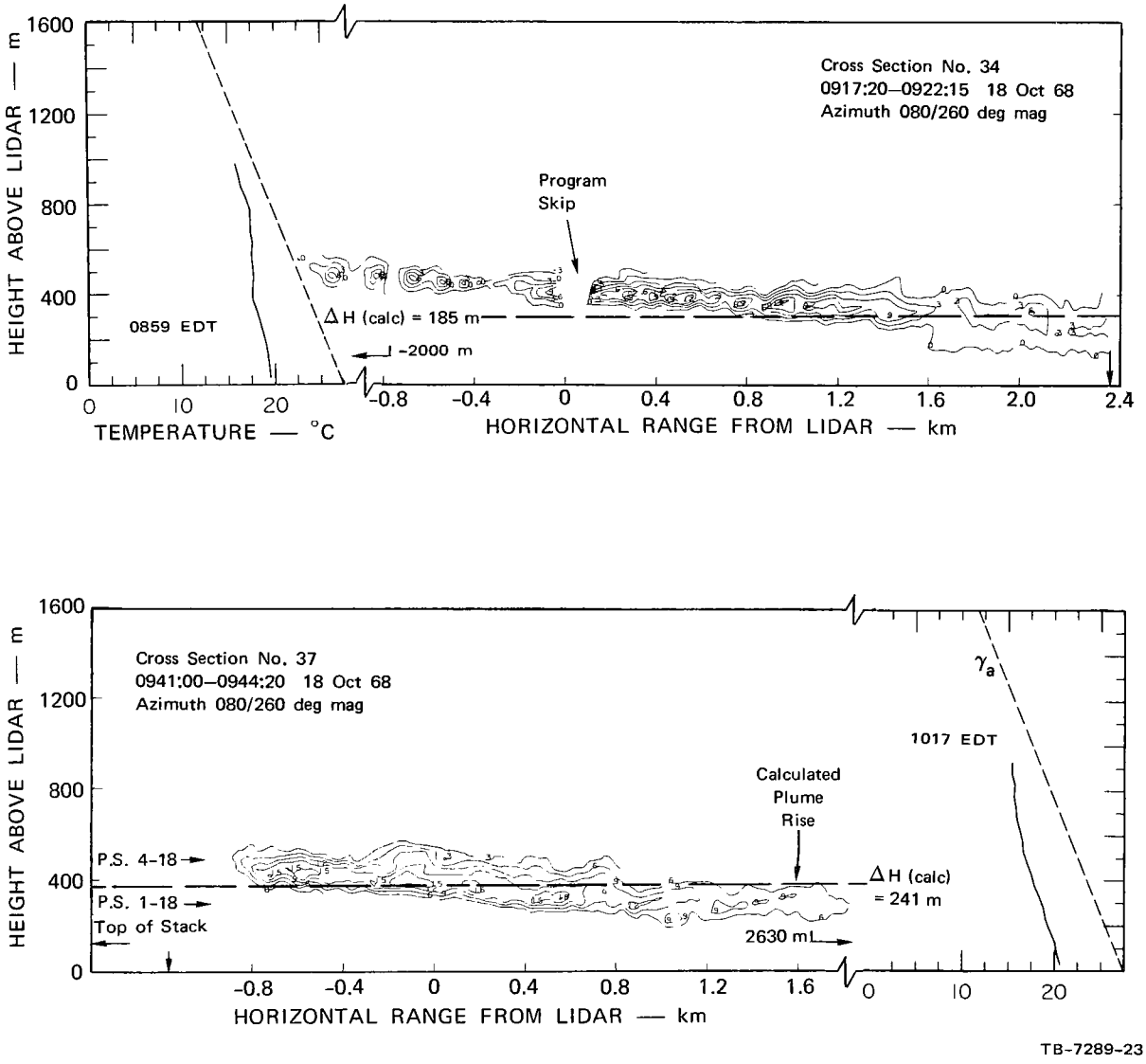

FIGURE 18 TIME SERIES OF LIDAR-OBSERVED VERTICAL CROSS SECTIONS FROM SITE 17, 13.7 km NORTH-NORTHWEST OF STACK, PLUME OVERHEAD, 18 OCTOBER 1968. See also Figure D-4. MRI particle sampling (P.S.) altitudes and run numbers are also indicated.

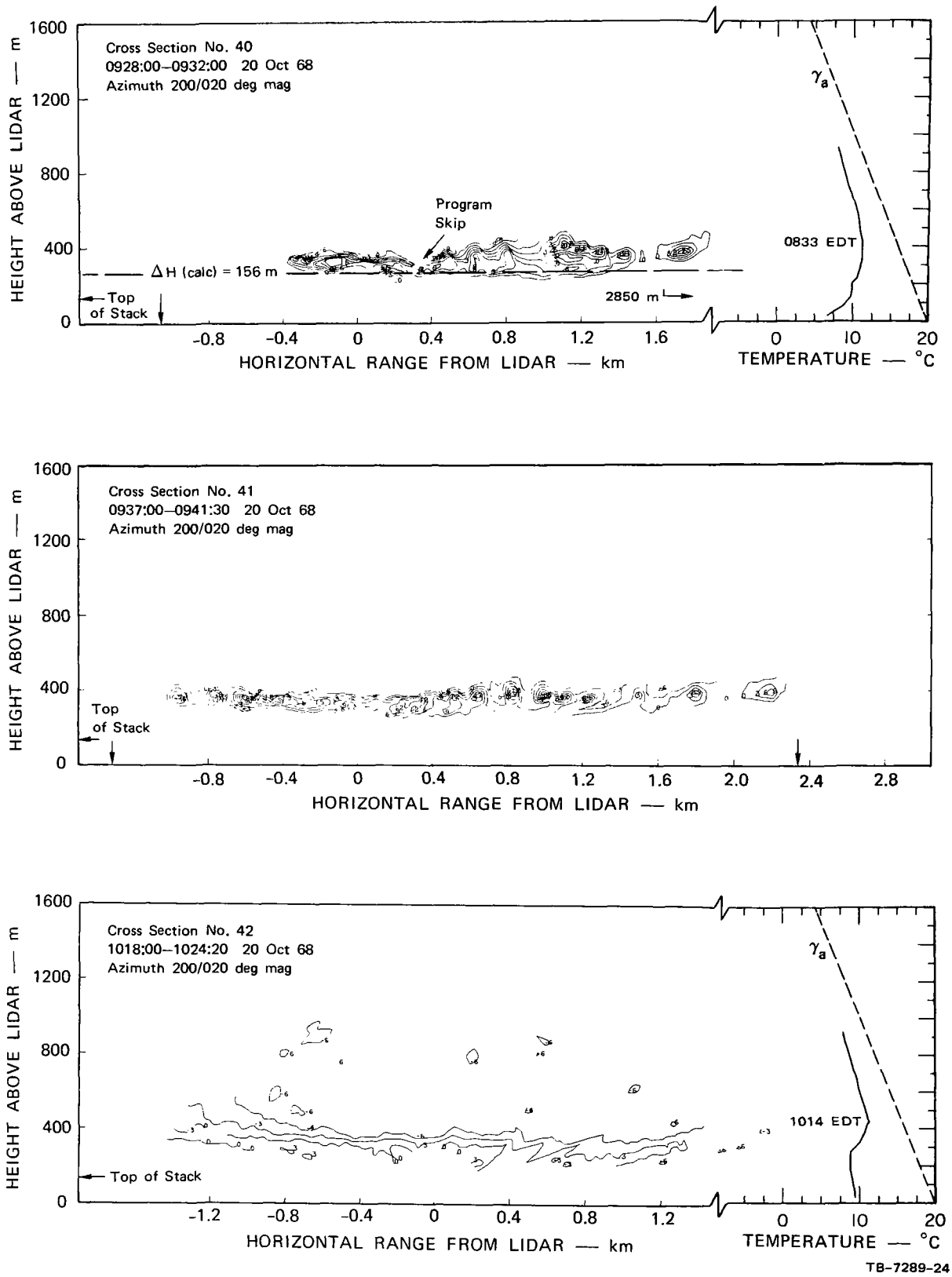

FIGURE 19 TIME SERIES OF LIDAR-OBSERVED VERTICAL CROSS SECTIONS FROM SITE 21, 21 km EAST-SOUTHEAST OF STACK, PLUME OVERHEAD, 20 OCTOBER 1968. See also Figure D-5.

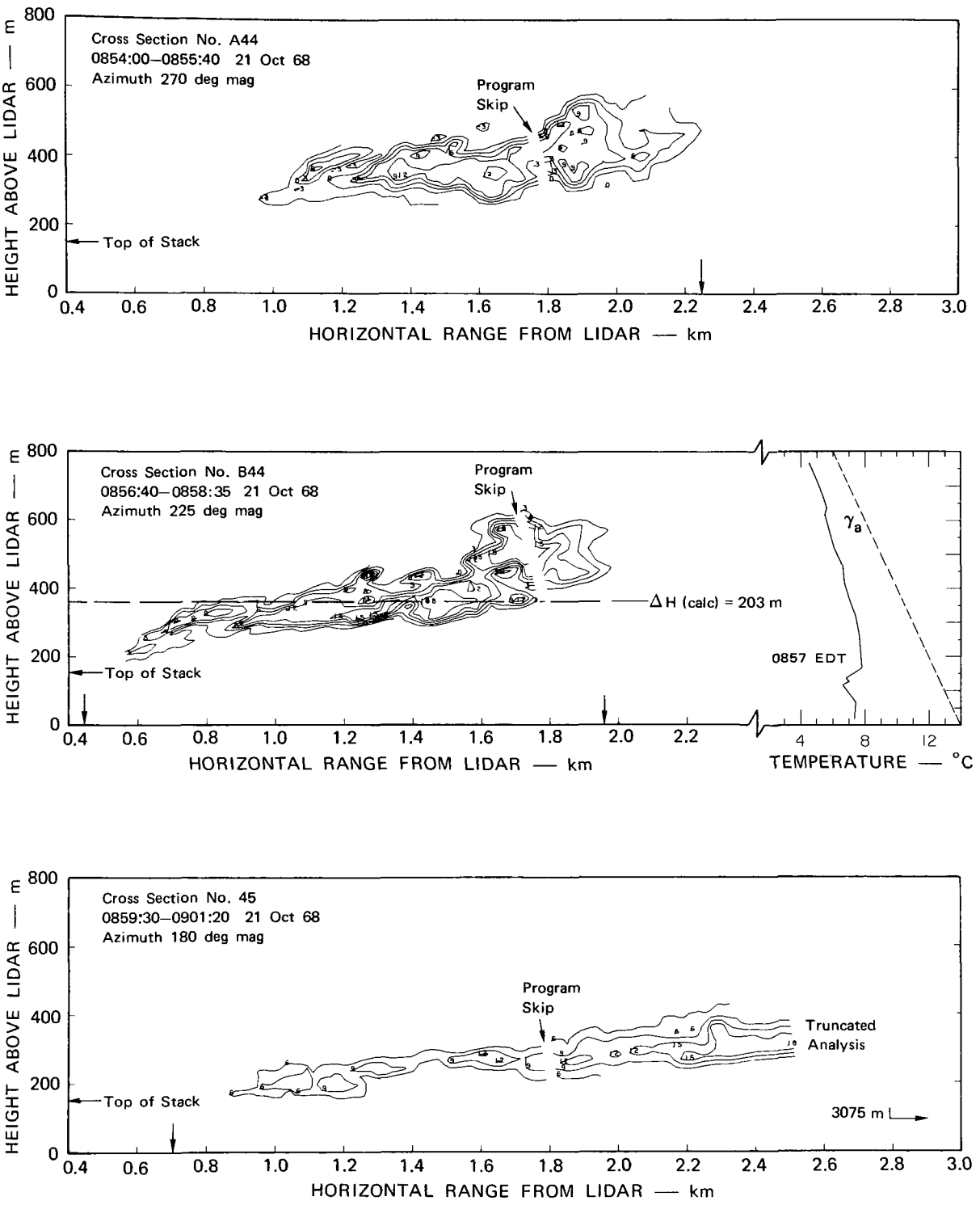

FIGURE 20 SPATIAL SERIES OF LIDAR-OBSERVED VERTICAL CROSS SECTIONS FROM SITE 22, 4.9 km SOUTHEAST OF STACK, 21 OCTOBER 1968, IMMEDIATELY PRIOR TO FULL PRECIPITATOR OPERATION. See also Figure D-6.

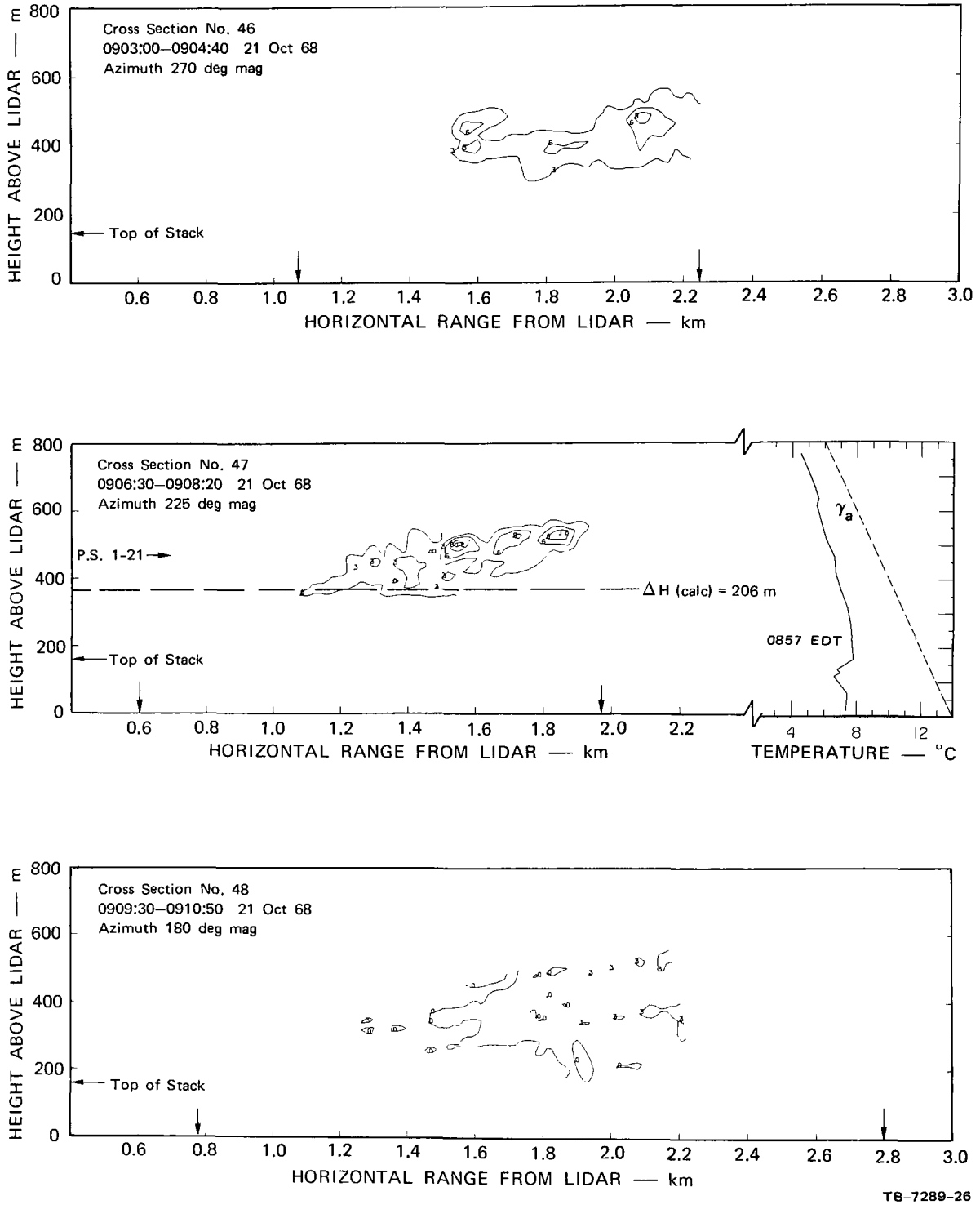

FIGURE 21 SPATIAL SERIES OF LIDAR-OBSERVED VERTICAL CROSS SECTIONS FROM SITE 22, 4.9 km SOUTHEAST OF STACK, 21 OCTOBER 1968, PRECIPITATORS IN FULL OPERATION. See also Figure D-6.

Later during the same morning, the cross sections in Fig. 22 were observed on the same azimuth angles. Here the lower portion of the plume is fumigating, while the upper portion remains relatively intact, probably due to the temperature inversion at 470 m.

Figures 23-26 illustrate various stages in the structure of the plume during the morning and midday of 22 October. In these figures the stack location is into the paper. Considering the cross sections located nearly crosswind (Cross Sections 58, 64, and 73), we see that at 0904 EDT the plume is compact and level (Cross Section 58), at 0941 EDT wind shear has set in and the plume is tilted, and at 1232 EDT fumigation of the lower portion is occurring. For the clean plume (Fig. 24), essentially no plume is apparent in the cross sections due to the weakness of the return signal in relation to the background noise level. Possibly because of the 3-MHz bandpass of the disk recorder, the data for clean plumes do not show up as well on these cross sections as on the 35-mm film, from which the plan views in Appendix D were obtained.

In Fig. 27, the plume apparently cannot penetrate the 1° C inversion at 500 m above the lidar, and is spreading out beneath with fumigation of the lowest portion. Cross Section 79 shows an interesting bubble at the top, which could be a thermal which has risen through the plume.

A series of approximately crosswind-oriented cross sections at about 15-minute intervals is shown in Figs. 28-30. The rapidly changing structure of the plume is apparent, as well as the trapping of the effluent by the stable layer at 400-500 m above the lidar. On this date, 24 October, the particulate output of the stack was reduced by 25 percent from previous days, since two additional precipitator sections were operating. As shown in Cross Section 104 (Fig. 29), there is some downward diffusion of the plume, but the stable near-ground layer apparently prevents the plume material from mixing to the ground.

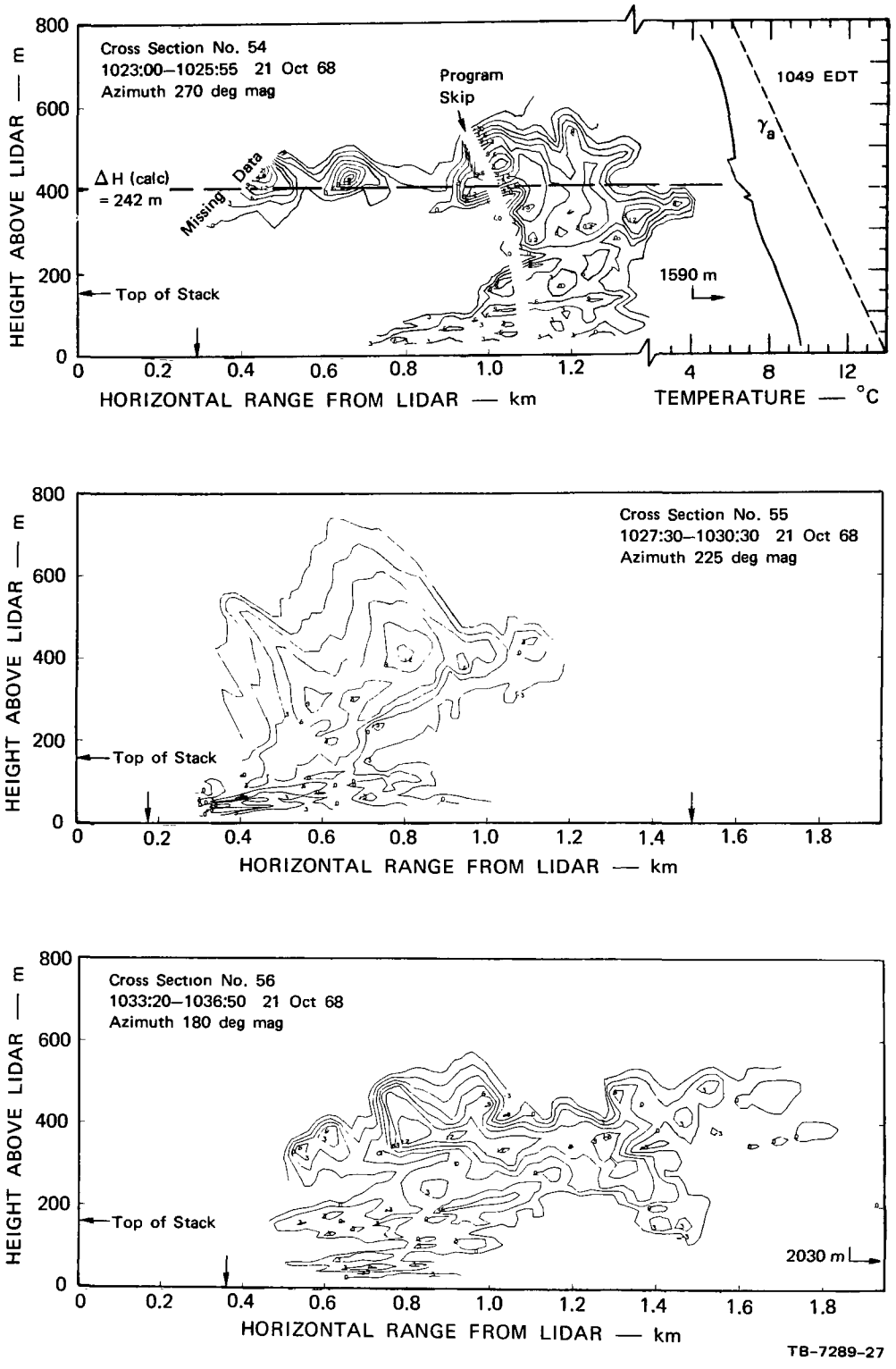

FIGURE 22 SPATIAL SERIES OF LIDAR-OBSERVED VERTICAL CROSS SECTIONS FROM SITE 22, 4.9 km SOUTHEAST OF STACK, 21 OCTOBER 1968. See also Figure D-6.

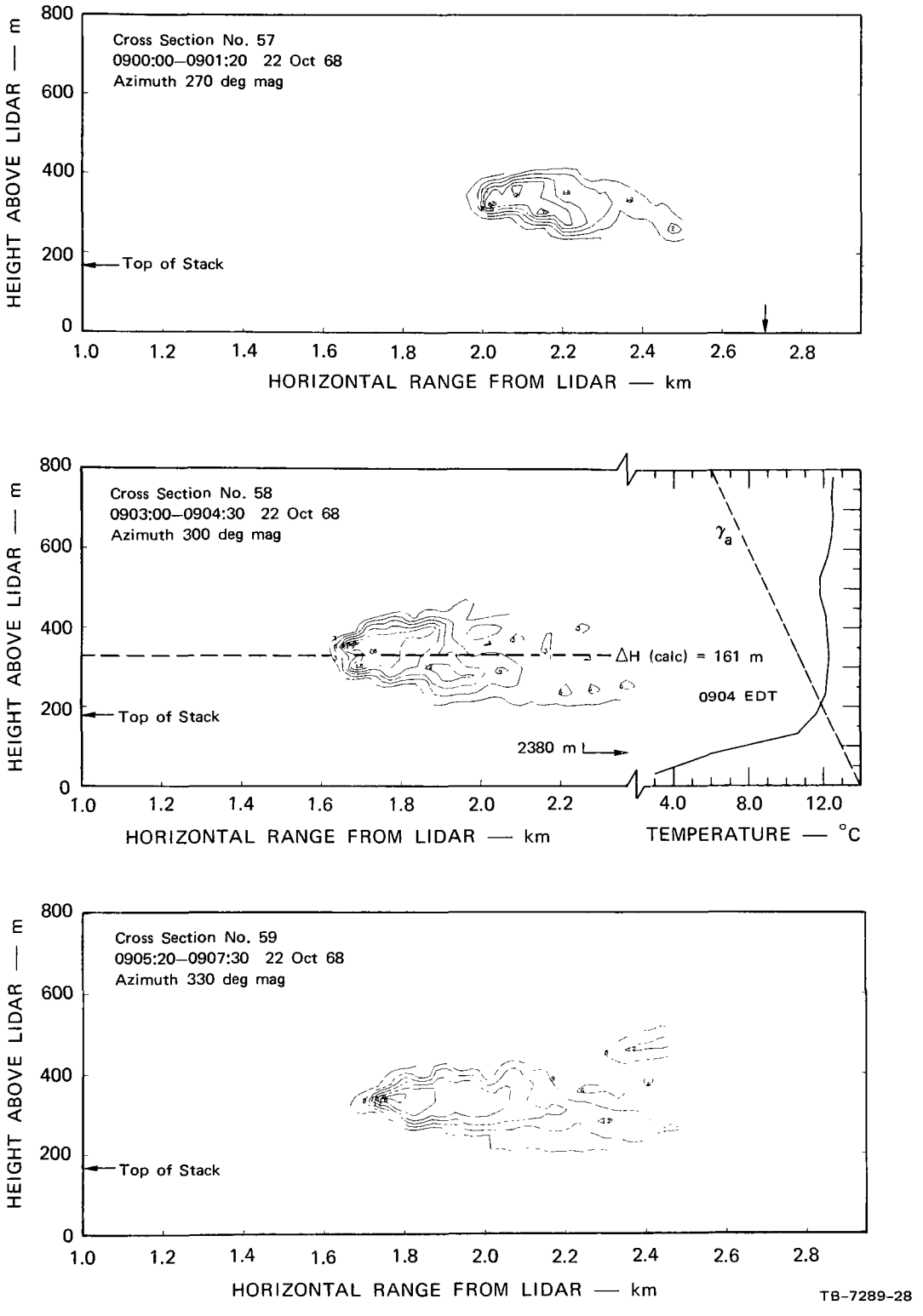

FIGURE 23 SPATIAL SERIES OF LIDAR-OBSERVED VERTICAL CROSS SECTIONS FROM SITE 6, 3.8 km NORTHEAST OF STACK, 22 OCTOBER 1968. See also Figure D-7.

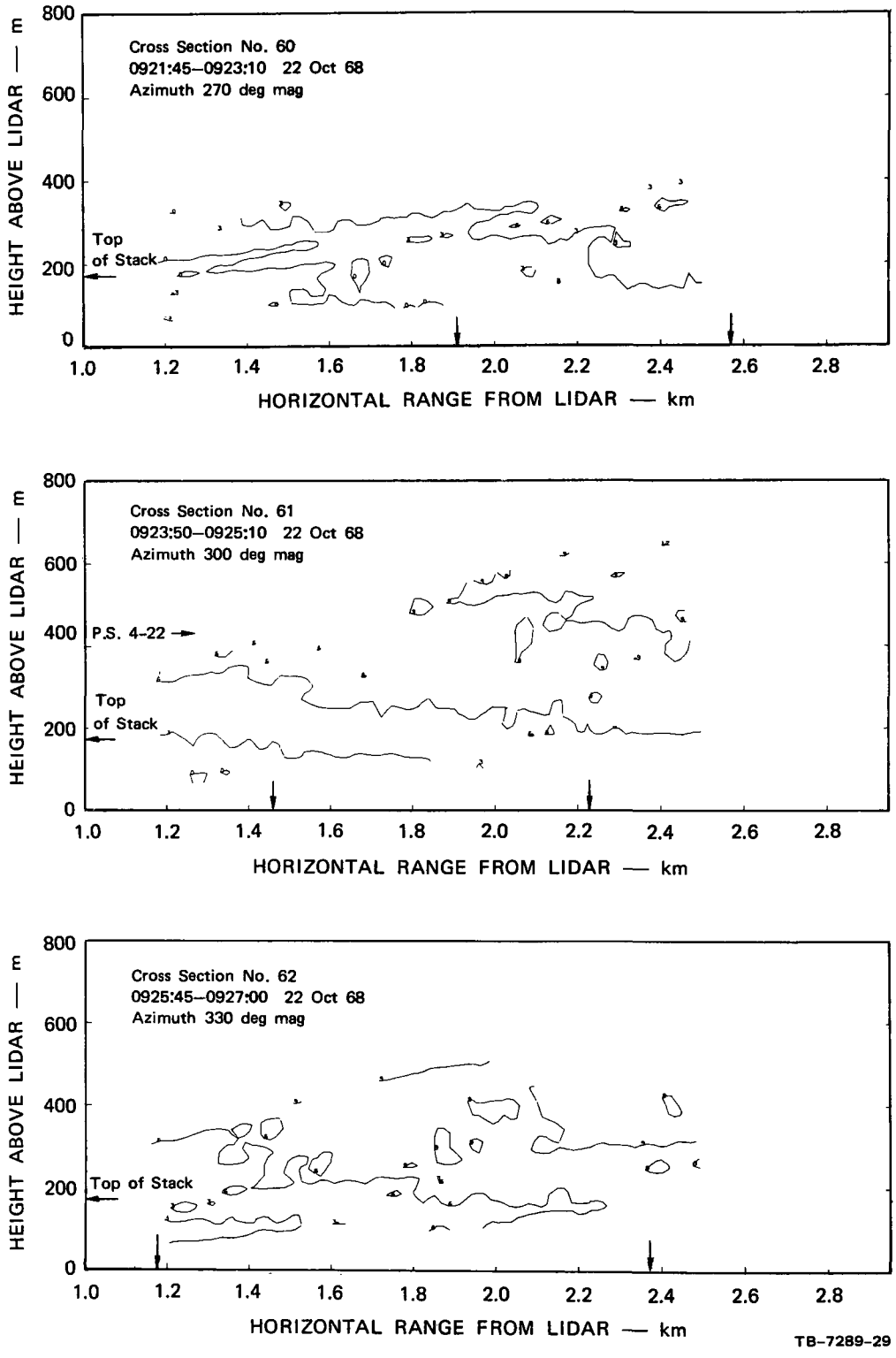

FIGURE 24 SPATIAL SERIES OF LIDAR-OBSERVED VERTICAL CROSS SECTIONS FROM SITE 6, 3.8 km NORTHEAST OF STACK, 22 OCTOBER 1968, CLEAN PLUME. See also Figure D-7.

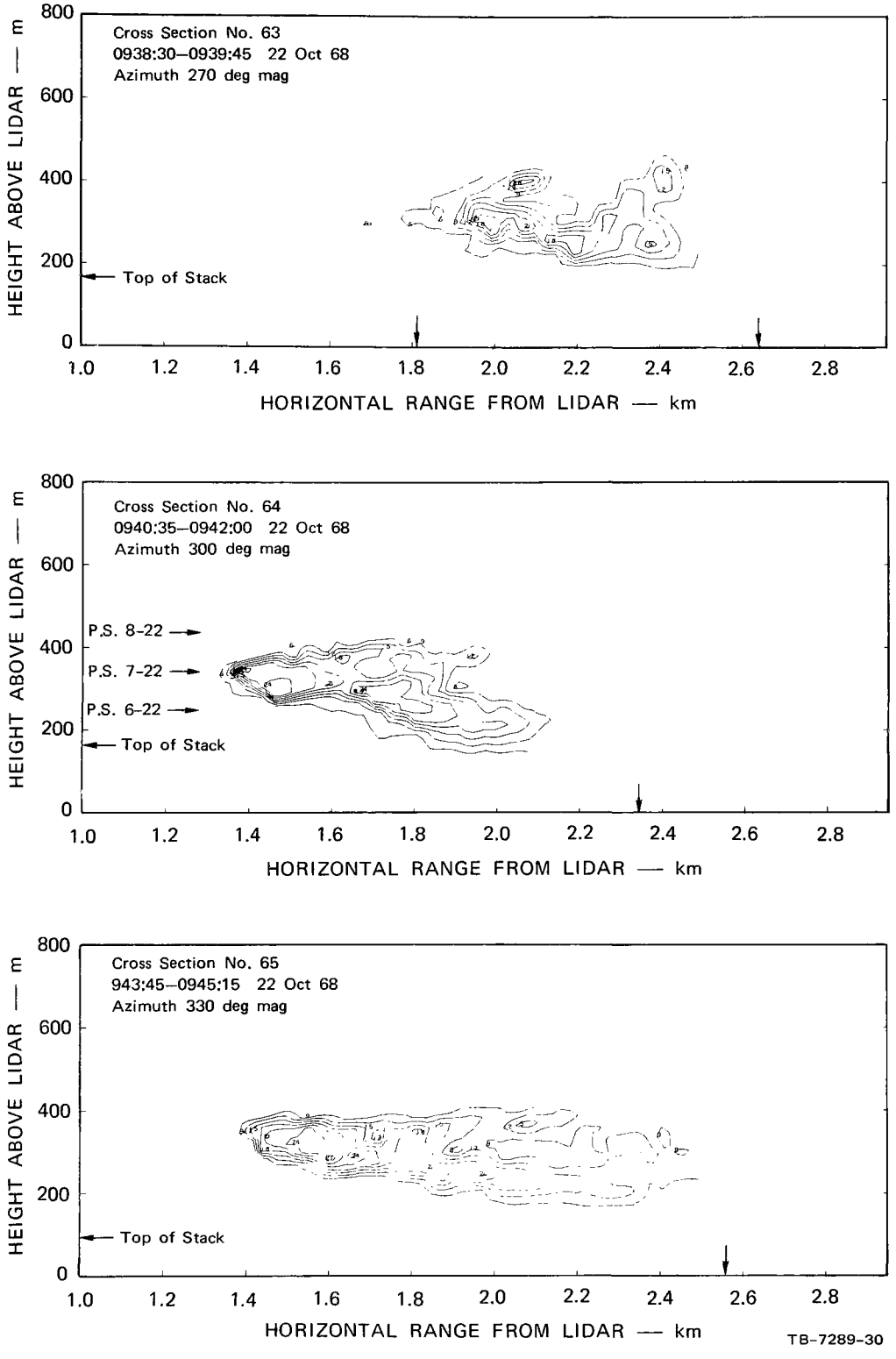

FIGURE 25 SPATIAL SERIES OF LIDAR-OBSERVED VERTICAL CROSS SECTIONS FROM SITE 6, 3.8 km NORTHEAST OF STACK, 22 OCTOBER 1968. See also Figure D-7.

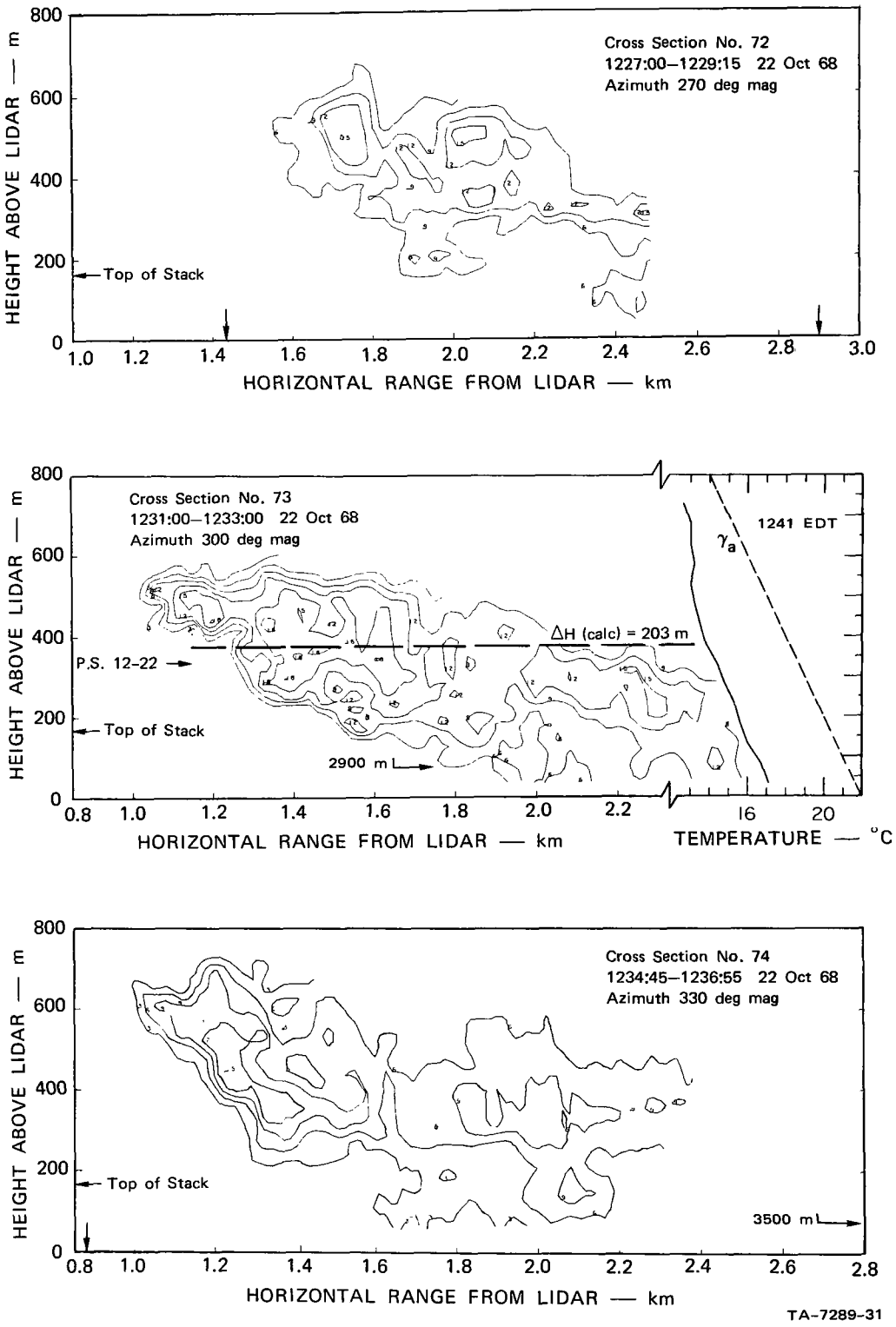

FIGURE 26 SPATIAL SERIES OF LIDAR-OBSERVED VERTICAL CROSS SECTIONS FROM SITE 6, 3.8 km NORTHEAST OF STACK, 22 OCTOBER 1968. See also Figure D-7.

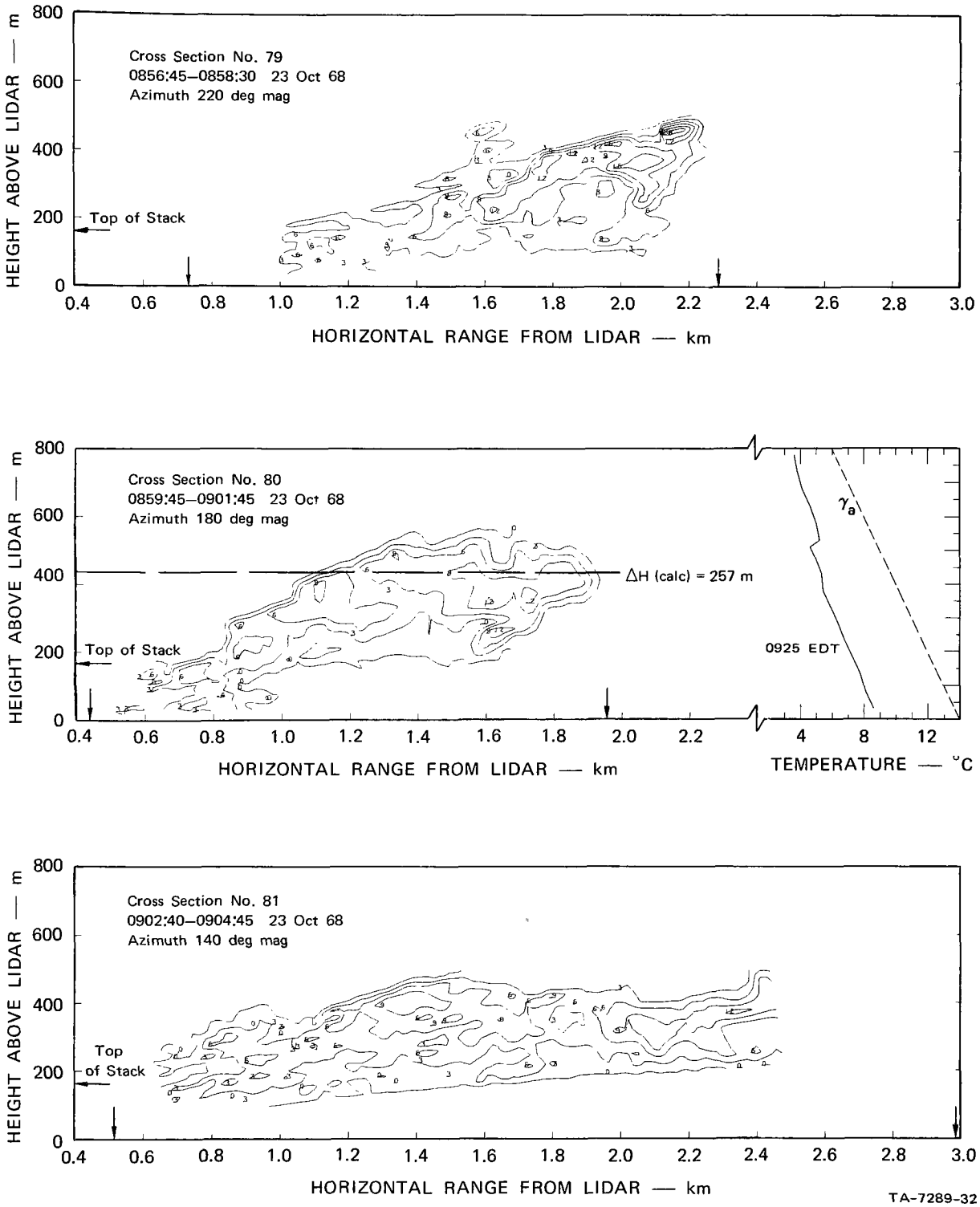

FIGURE 27 SPATIAL SERIES OF LIDAR-OBSERVED VERTICAL CROSS SECTIONS FROM SITE 6, 3.8 km NORTHEAST OF STACK, 23 OCTOBER 1968. See also Figure D-8.

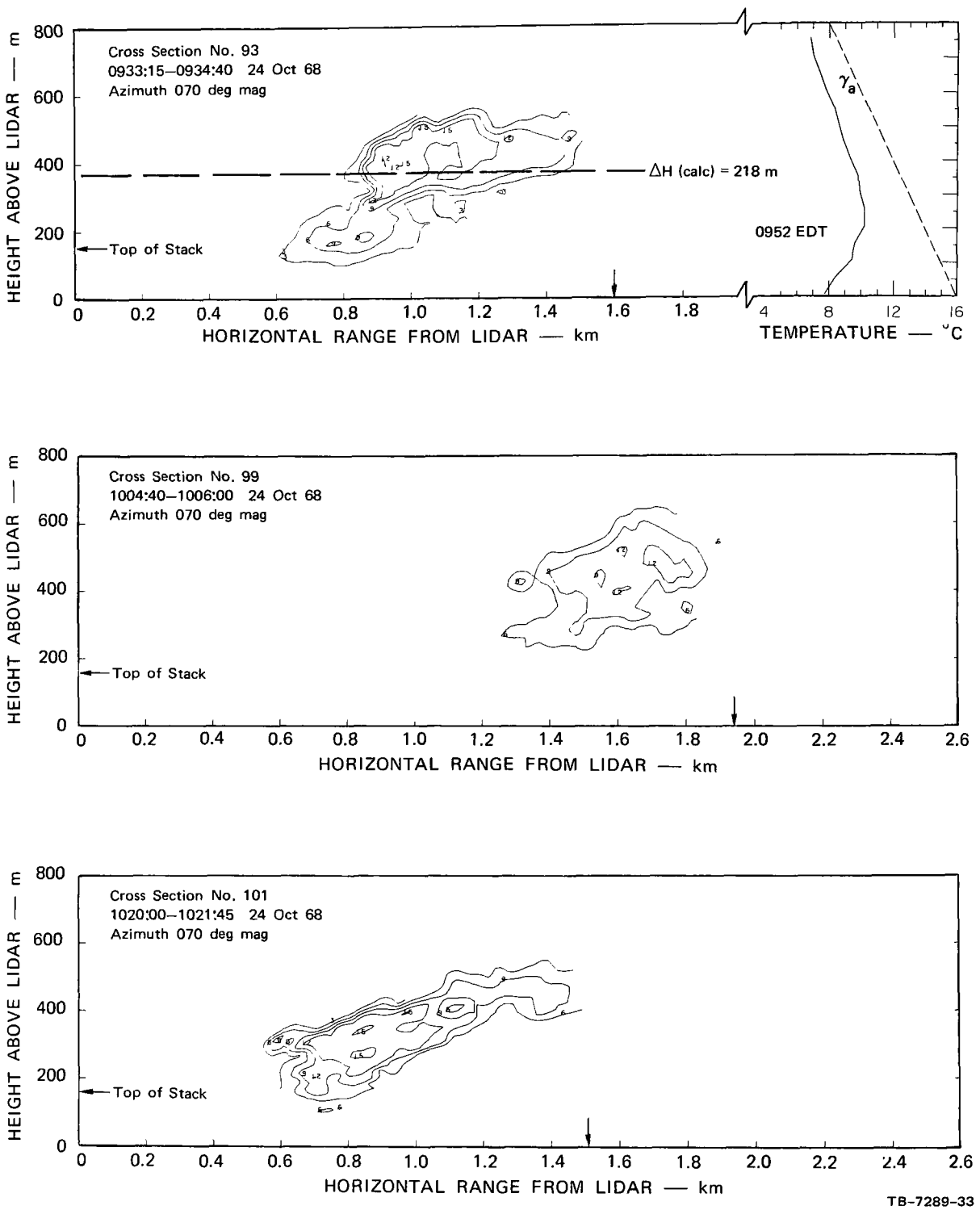

FIGURE 28 TIME SERIES OF LIDAR-OBSERVED VERTICAL CROSS SECTIONS FROM SITE 11, 4 km NORTHWEST OF STACK, 24 OCTOBER 1968. See also Figure D-9.

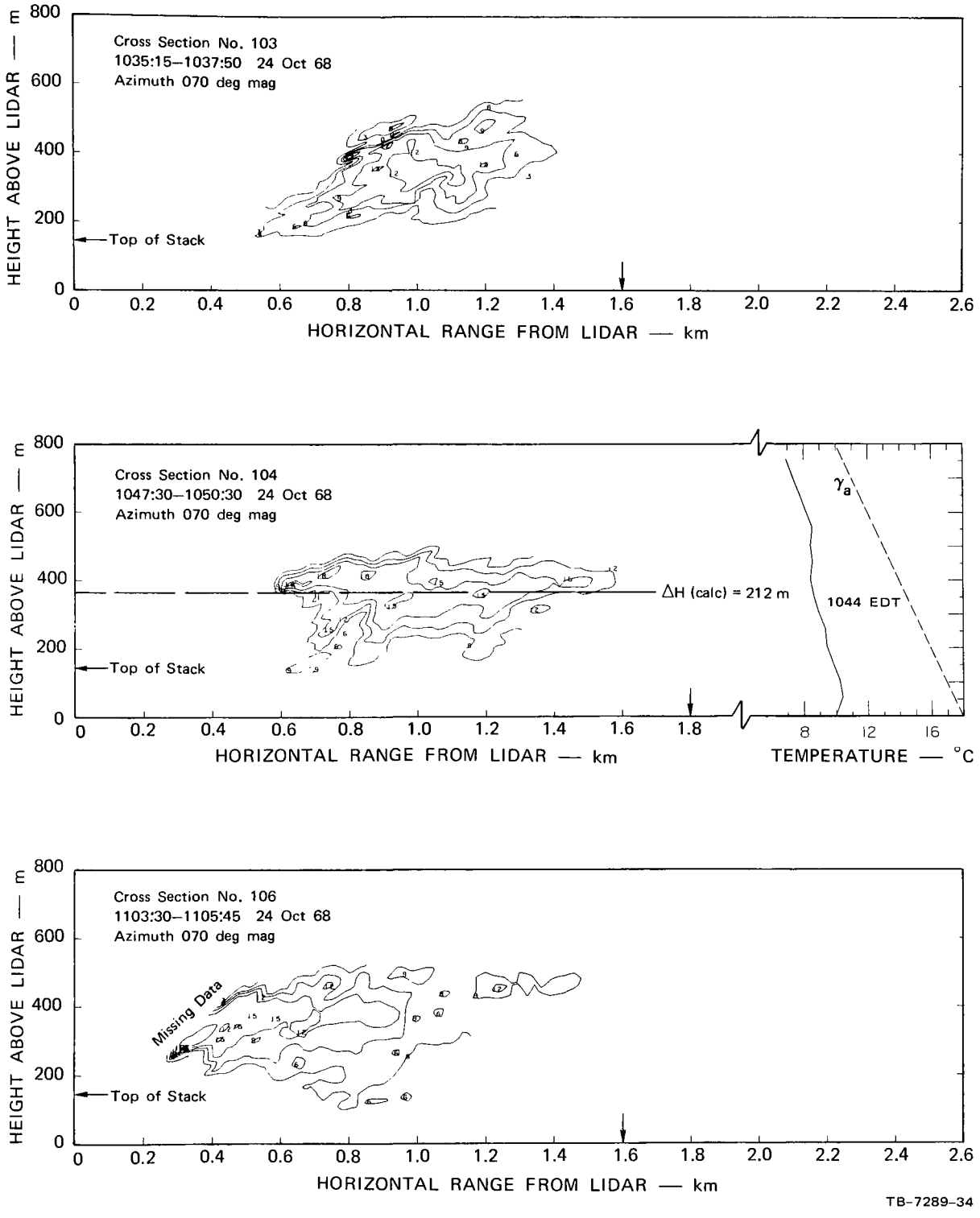

FIGURE 29 TIME SERIES OF LIDAR-OBSERVED VERTICAL CROSS SECTIONS FROM SITE 11, 4 km NORTHWEST OF STACK, 24 OCTOBER 1968. See also Figure D-9.

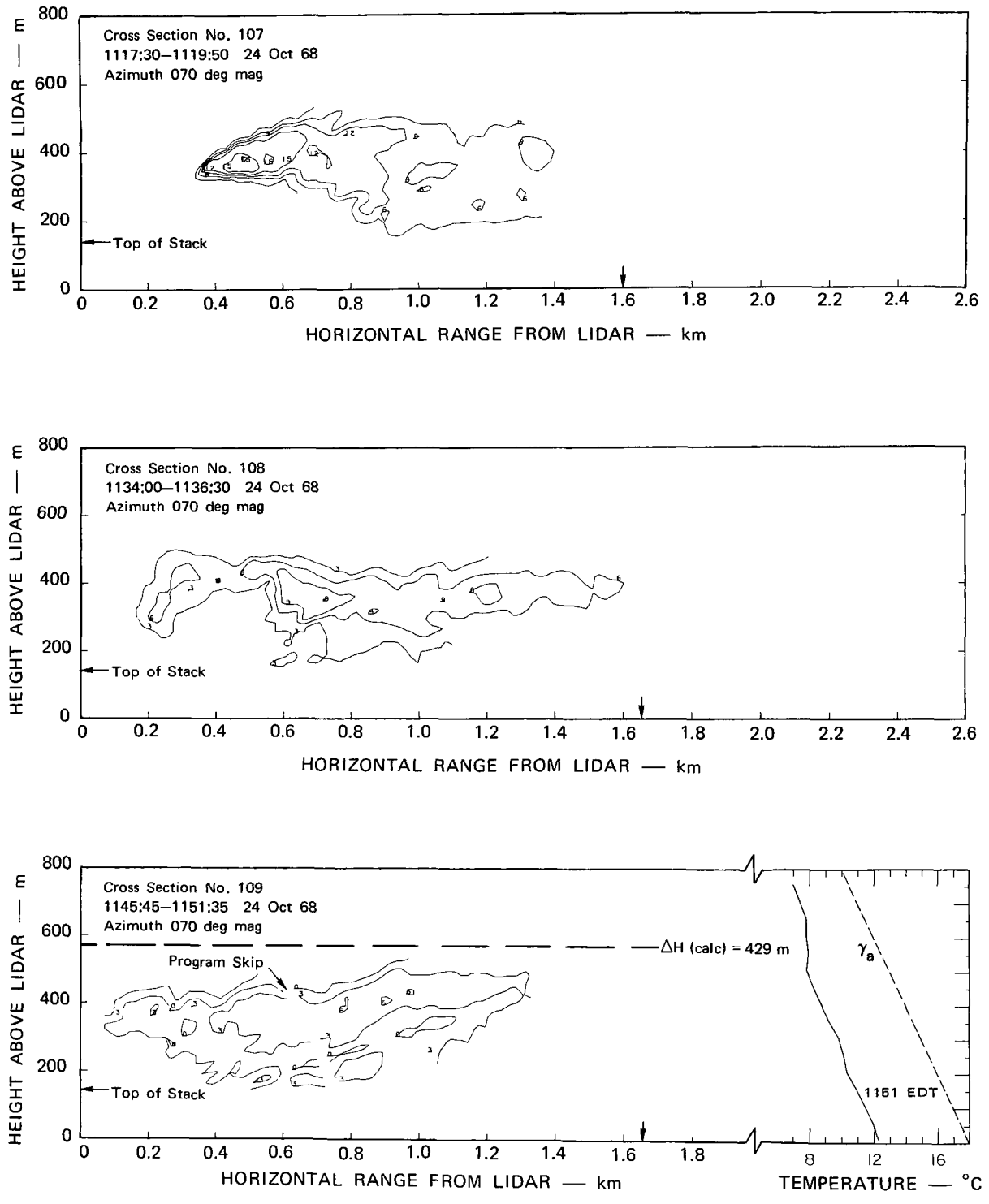

FIGURE 30 TIME SERIES OF LIDAR-OBSERVED VERTICAL CROSS SECTIONS FROM SITE 11, 4 km NORTHWEST OF STACK, 24 OCTOBER 1968. See also Figure D-9.

VI INTERPRETATION OF CROSS SECTIONS IN TERMS OF PLUME RISE AND DIFFUSION

The new capability to "see" the detailed structure and geometry of plumes, which lidar makes possible, gives the instrument decided potential in plume rise and diffusion studies. However, as often happens when a new technique enables us to obtain detailed observations where only sparse data were available before, the lidar data have underscored the complexities of plume behavior and made apparent the weaknesses of certain of the present concepts and theoretical assumptions.

After examination of the plume cross sections in Sec. V, it is apparent that plume tilting and fanning caused by wind direction shear is a characteristic feature of plume behavior in stable conditions. It then becomes difficult to identify any one level of the plume for use in computing plume rise. The concept of plume rise also tends to lose meaning under fumigation conditions, which were frequently observed, and under unstable (looping) conditions. Equally important as complicating factors are the temperature inversions and stable layers, which regularly occur aloft and tend to trap the plumes and prevent further rise. The lidar data for October show several instances of this. Thus the data emphasize that there typically are significant vertical variations in stability and wind structure that have profound effects upon plume behavior, and that are not taken into account by the plume rise theories.

Plume-rise values (ΔH) for the stable cases were calculated from the formula recommended by the ASME* Committee on Air Pollution Controls (Smith, 1968):

$$\Delta H = 2(F/G\bar{U})^{1/3} \qquad (5)$$

*American Society of Mechanical Engineers.

with

$$F = g\, r^2\, V_s \left(T_s - T_a\right)/T_a$$

$$G = \left(g/T_a\right)(\Delta T/\Delta Z + 0.01)$$

and

$$\bar{U} = \left(U_t + U_a\right)/2$$

$$\Delta T = T_t - T_a$$

$$\Delta Z = H_t - H_s \qquad \text{(after Proudfit, 1969)}$$

where

F = buoyancy flux

g = acceleration of gravity (= 9.8 m/s)

r = radius of stack orifice (= 4.25 m for Keystone)

V_s = stack gas exit velocity

T_s = stack gas exit temperature

T_a = ambient atmospheric temperature at stack top

G = stability parameter

$\bar{U}$ = mean wind speed over height interval where rise occurs

U_t = wind speed at height of plume top (H_t) after maximum rise

U_a = wind speed at height of stack top (H_s)

T_t = air temperature at height of plume top.

The computed values, as well as the values of the input parameters used, are listed in Table III.

In view of the complications discussed previously with regard to defining plume rise in a manner that permits objective determination from lidar plume cross sections, the calculated plume rise values have been indicated directly on the cross sections, Figs. 9-12 and 15-30.

Table III

VALUES OF INPUT PARAMETERS USED AND RESULTS FROM PLUME RISE CALCULATIONS USING ASME FORMULA FOR STABLE CONDITIONS

Date (1968)	Time (EDT)	Cross Section Number	V_s (ft/s)	T_s (°F)	T_a (°C)	T_t (°C)	H_t (m)	H_s (m)	U_t (m/s)	U_a (m/s)	ΔH (m)	$\Delta H + H_s$ (m)
5/25	0919	2	73.0	275.0	12.8	11.6	590	240	7.5 at 84°	6.2 at 70°	206	446
	1036	4	73.0	275.0	12.7	9.7	850	240	5.3 at 89°	4.5 at 49°	251	491
5/26	0900	12	68.5	270.0	15.4	13.4	540	160	11.0 at 157°	3.0 at 111°	220	380
10/16	0917	16	68.6	292.0	17.3	17.5	470	152	9.0 at 186°	5.9 at 153°	169	321
	0945	20	68.6	292.0	17.3	17.6	430	152	10.5 at 187°	5.2 at 150°	164	316
10/17	0912	27	68.7	292.0	19.7	18.3	530	152	12.4 at 176°	7.2 at 150°	183	235
10/18	0920	34	65.9	289.0	18.7	17.1	550	122	10.9 at 168°	7.2 at 136°	185	307
	0942	37	65.9	289.0	20.0	16.5	580	122	14.3 at 165°	7.2 at 136°	241	363
10/20	0928	40	67.1	267.0	9.6	11.0	460	122	6.8 at 248°	6.4 at 235°	156	278
10/21	0857	B44	67.0	278.0	7.5	5.5	620	162	9.1 at 326°	7.5 at 305°	203	365
	0907	47	69.0	278.0	7.5	5.8	570	162	7.8 at 328°	7.5 at 305°	206	368
	1024	54	69.0	278.0	8.6	5.9	580	162	8.1 at 325°	7.4 at 314°	242	404
10/22	0903	58	59.2	292.0	11.5	12.1	430	176	7.9 at 193°	5.5 at 153°	161	337
	1232	73	59.2	292.0	15.7	13.2	580	176	14.9 at 218°	6.0 at 196°	203	379
10/23	0900	80	73.1	285.0	7.3	4.7	550	176	9.0*	7.5 at 241°	257	433
10/24	0934	93	61.3	300.0	9.6	8.3	560	152	4.9 at 158°	5.7 at 127°	218	370
	1049	104	61.3	300.0	9.8	8.5	470	152	6.4 at 156°	6.9 at 137°	212	364
	1148	109	61.3	300.0	11.0	7.7	510	152	6.2 at 150°	5.8 at 127°	429	581

*Estimated.

In this way, detailed comparisons with the observed plume heights and shapes are possible.

In general, the ASME formula appears to predict plume rise reasonably well, although of course the frequent presence of temperature inversions at plume levels diminishes the relevancy of the theory in many instances. For the few cases where the vertical temperature gradient at plumes levels is approximately uniform with height, and vertical wind shear--and thus plume tilting--is weak (e.g., Cross Section 58, Fig. 23), the agreement between the theory and the observations is excellent. On the whole, there appears to be a weak indication that the ASME formula may predict slightly lower plume rises than observed.

The capabilities of lidar in computing diffusion parameters are fairly obvious, at first glance, from inspection of the horizontal plan views of plume positions in Figs. 9-12 (insets) and in Appendix D, which show the horizontal spread of the effluent with downwind distance. Again, however, wind direction shear and the attendant spreading of the plume by shearing are not adequately covered by present theories. The best application of current theory is probably for the neutral and unstable cases, when vertical wind shear is not usually so pronounced. Here another problem is encountered, in that most theories are only valid for mean concentrations over a period of 30 minutes to an hour (Gifford, 1961). To be most useful here, then, a lidar should be capable of taking fast, quasi-instantaneous cross sections through a plume at frequent intervals for extended periods on the order of an hour. The results of these cross sections would then be averaged to obtain a mean concentration distribution to compare with theory. The present equipment requires about two to three minutes for a complete cross section. Under unstable conditions when the plume position is rapidly changing, some distortion is introduced into the cross sections due to the lack of instantaneity of the individual lidar observations.

Another important consideration for studying plume diffusion with a lidar is the receiver signal-to-noise ratio at the range where the plume is observed. As seen in Fig. 6, a portion of the plume return is

truncated when the plume is observed at a range beyond that at which clear-air return is detected above the noise. This decreases the observed size of the plume, and hence affects the diffusion calculations unless suitable allowances are made. A prime example of this effect is shown by Figs. 20 and 21 and the corresponding plume plan views in Appendix D.* Here a series of six cross sections were obtained within a time period of 15 minutes. The precipitators were all on when the last three cross sections were observed, furnishing a clean plume. Due to background noise considerations, this clean plume is "seen" by the lidar to be considerably smaller than the dirty plume. However, the diffusion regime was the same.

The Mark V lidar has an effective above-noise range for clear-air return on a typical bright day of about one to two km in the neodymium version, but this could be readily improved by using a ruby or YAG† laser and/or additional signal-to-noise enhancement equipment and techniques.

---

*The effect is not as pronounced in the plan views due to the greater recording resolution of the 35-mm film system.

†Ytrrium aluminum garnet, wavelength 1.06 μ.

VII EVALUATION OF PARTICULATE MASS CONCENTRATIONS FROM LIDAR NORMALIZED SIGNAL RETURN (S) VALUES

As discussed in Sec. IV, the conversion of S values to absolute mass concentrations requires allowance for the effect of attenuation of the laser beam as it passes through the atmosphere and the plume. This problem is best approached by solving the differential equation derived from Eq. (4) (Sec. IV):

$$\frac{dS}{dR} = 4.34 \frac{1}{\beta} \frac{d\beta}{dR} - 8.7\ \sigma \tag{6}$$

where Bouquer's law of attenuation

$$T(R) = \exp\left[- \int_o^R \sigma(\ell)\ d\ell \right] \tag{7}$$

has been assumed and $\sigma(\ell)$ is the volume extinction coefficient at a distance ℓ along the path. The solution of Eq. (6) for particulate mass concentration along the laser beam path requires relating the optical parameters σ and β to the particulate mass concentration. For this purpose the ratio of each optical parameter to the particulate mass concentration M(mass/volume) is defined as

$$\xi_e \equiv \frac{\sigma}{M} \quad , \quad \xi_b \equiv \frac{\beta}{M} \quad . \tag{8}$$

Substitution of Eq. (8) into the lidar differential equation [Eq. (6)] results in an expression relating mass concentration to the lidar normalized signal return:

$$\frac{dM}{dR} - \frac{1}{4.34} \frac{dS}{dR} M - 2\ \xi_e M^2 = 0 \quad , \tag{9}$$

where ξ_b has been considered independent of range. The validity of this assumption will be discussed later. This nonlinear equation may be solved by first employing the linearization transform $\eta \equiv M^{-1}$ with the

result

$$M(R) = \exp\left[C_1 S(R)\right]\left[M_o^{-1} - 2\,\xi_e \int_{R_o}^{R} \exp\left[C_1 S(\ell)\right] d\ell\right]^{-1} \tag{10}$$

where $C_1 = 1/4.34$. This solution principally assumes that

(1) ξ_e and ξ_b are invariant with range and the value of ξ_e can be computed, and

(2) a boundary or clear-air particulate mass concentration, M_o, is known or can be estimated.

Microscopic analysis of the Keystone fly ash clearly shows that the particles are glass spheres, apparently formed from the mineral content of the coal by the intense heat of the combustion process; hence, the use of Mie theory in deriving estimates of ξ_e and ξ_b is justified. To a high degree of accuracy, the volume extinction coefficient at the lidar wavelength of 1.06 μ may be considered to be essentially dependent only on the atmospheric particulate matter, and the ξ values may be expressed* as:

$$\xi_e = \frac{\int_o^\infty \pi\, a^2\, Q_e(x,m)\, n(a)\, da}{\int_o^\infty \frac{4}{3}\pi\, a^3\, \rho\, n(a)\, da} \tag{11}$$

$$\xi_b = \frac{\int_o^\infty \pi\, a^2\, Q_b(x,m)\, n(a)\, da}{\int_o^\infty \frac{4}{3}\pi\, a^3\, \rho\, n(a)\, da} \tag{12}$$

*To be precise, the parameters ξ_e and ξ_b defined by Eqs. (11) and (12) are exactly equivalent with those defined by Eq. (7) only when multiple scattering effects are absent. This is a good assumption for this study because of the narrow field of view of lidar systems (<1 mrad).

where

a = particle radius

Q_e = extinction efficiency factor

Q_b = backscatter efficiency factor

x = size parameter = $2\pi\ a/\lambda$

m = refractive index of particles

λ = wavelength of the laser energy

n = number of particles per unit volume per unit radius interval, and

ρ = density of the particulate matter.

The efficiency factors may be computed from Mie theory for a given particulate matter refractive index, the real part of which in this case was estimated to have a value of approximately 1.5, based upon the known mineral composition of coal. The requirement that ξ_e and ξ_b be independent of range is satisfied when the relative particle-size distribution is invariant with range; i.e.,

$$n(R,a) = C(R)\ n_r(a) \quad , \tag{13}$$

where $C(R)$ is the number concentration and $n_r(a)$ is the relative size distribution. Also, with this assumption only the relative particle size distribution is required to evaluate the ξ values. However, $n_r(a)$ is rarely completely independent of range, and the question may be asked as to how small changes in the relative size distribution are reflected in the ξ values. Since the ξ values are expressed in terms of integrals over the range of particle sizes, monodispersed (single-sized) particles would cause largest ξ variations with slight changes in the particle size. Mie computations of ξ_e and ξ_b are presented in Fig. 31 for the case of monodispersed particles consisting of material with a density of 2.1 g/cm^3 (as measured at the Institute from a Keystone fly ash sample) and a refractive index of $m = 1.5\text{-}i0$ for incident radiation of wavelength 1.06 μ.

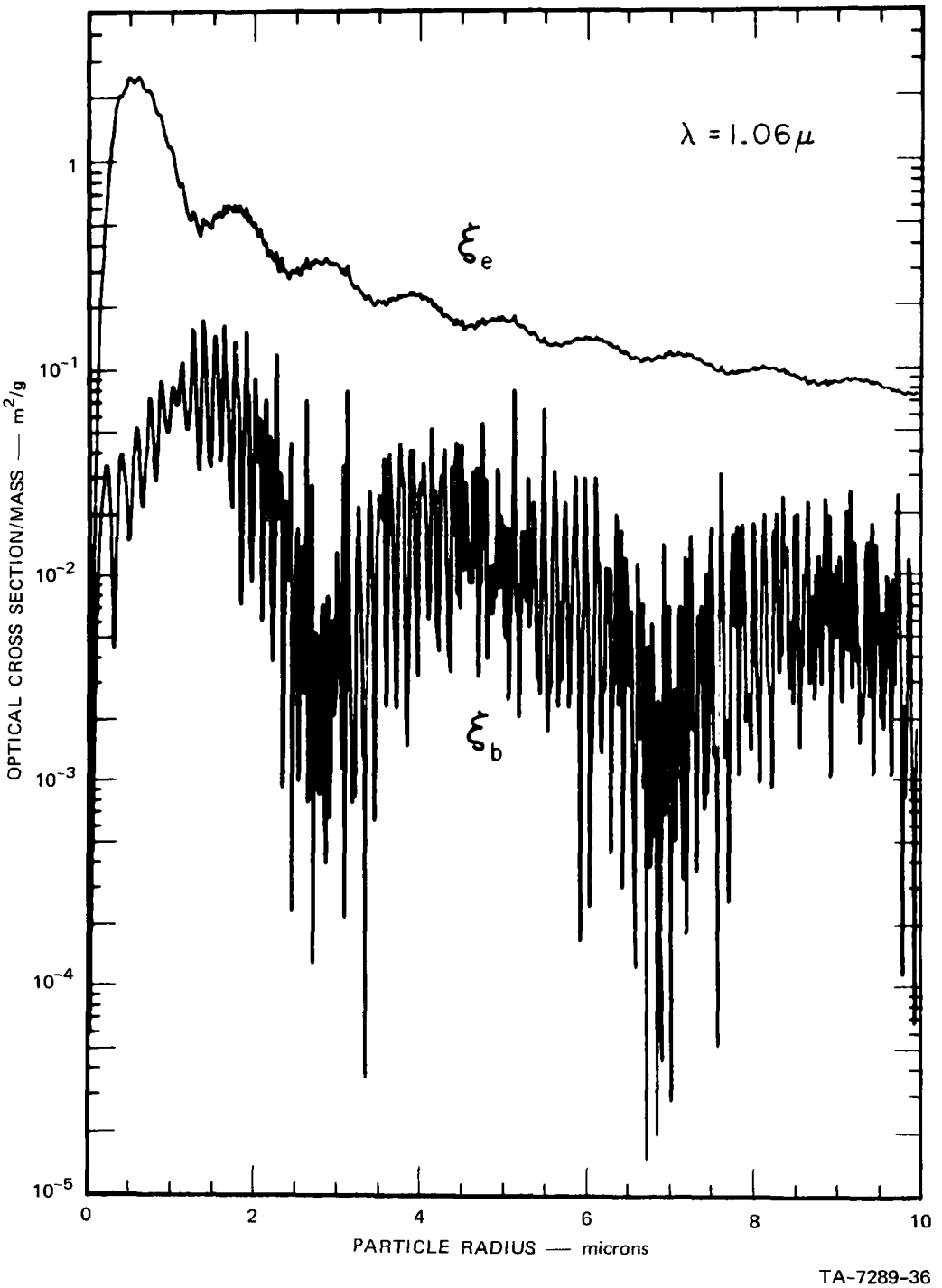

FIGURE 31 DEPENDENCE UPON PARTICLE SIZE OF TOTAL SCATTERING—EXTINCTION—OPTICAL CROSS SECTION PER UNIT MASS (ξ_e), AND BACK BACK-SCATTERING OPTICAL CROSS OPTICAL CROSS SECTION PER UNIT MASS PER STERADIAN (ξ_b). For mono-disperse particles with refractive index of 1.5-iO and density of 2.1 g/cm^3

As shown, slight variations in particle size can cause large variations in ξ_b and smaller but significant variations in ξ_e. Because of this, and the fact that P_s is more sensitive to variations in β than σ [Eq. (1)], the requirement that ξ_b remains constant with range also satisfies the less stringent requirement that ξ_e remains invariant.

A real aerosol contains particles of many sizes, so the variations in the ξ curves tend to be smoothed out when a weighted integral for all sizes present is computed. The next section will explain the methods developed to handle the supplementary particle-size data obtained during the Keystone study for use with the lidar observations.

VIII ANALYSIS OF ATTENUATION EFFECT USING PARTICLE-SIZE CHARACTERISTICS

The Keystone stack plume particulates were sampled with an airplane-mounted Goetz moving slide impactor (Goetz, 1969) by Meteorology Research, Inc. (MRI), at times nearly concurrent with the SRI lidar observations. Tentative relative particle size distribution data for specified sampling periods were furnished SRI (see Table IV) along with information required to evaluate the number of particles per unit volume per unit radius interval for increments of 0.25 μ in radius. The relative size distribution is sufficient to evaluate the optical parameters ξ_e and ξ_b for use with the lidar data.

Ideally, however, one would like to compare mass concentrations measured by the MRI sampler with those derived from the lidar data. This was not possible, since our conversions of the relative particle-size data to absolute size distributions (using the furnished sample-volume values) and then to mass concentrations give unrealistically large values of concentration for the clear air ($M_o > 1000\ \mu g/m^3$) upwind of the stack. Hence it has been necessary to use the empirical relationship derived by Noll, et al. (1968) to determine the clear-air background mass concentration (M_o) from visual estimates of atmospheric visibility.

The solution parameter ξ_e and the parameter ξ_b were evaluated from the furnished relative size distributions for each data sample listed in Table IV; these values are tabulated in Table V. In these computations, integrations over particle radii were performed by means of rectangular integration, with the size distribution assumed constant within each sampling interval. The parameters ξ_e and ξ_b were evaluated from sampling-interval-averaged optical cross sections defined as:

$$\bar{C} = \pi\overline{a^2 Q} = \left(\lambda^2/4\pi\right)\int x^2 Q(x)\,dx \Big/ \int dx \qquad (14)$$

where $x = 2\pi a/\lambda$ (see Sec. VII), and the integration was trapezoidal with 0.1 intervals in x ($0.106/2\pi$ radius intervals at $\lambda = 1.06\ \mu$).

Table IV

SUMMARY OF MRI PARTICLE-SIZE DISTRIBUTION DATA

(Compiled by Stanford Research Institute)

Count No.	Date (October 1968)	Time (EDT)	Slide No.	Slide Position	Photo Exposure Time (s)	Slide Exposure Time (s)	Aircraft Radial Position		Aircraft Altitude		Portion of Plume Sampled†	Precipitator Capacity On (percent)	Associated Lidar Cross Section No.
							Relative to Stack (km)	Relative to Lidar (km)	(Ft MSL)	(m above Lidar)			
1	16	0953	5-16	2	0.5	29	3 DW*	6 UW*	2320	289	Unknown	50	--
2	17	0853	2-17	4	0.5	29	3 DW	6 UW	2750	420	Unknown	50	--
3	17	0957	16-17	10	0.2	109	16 DW	7 DW	2650	390	Unknown	50	--
4	17	1219	22-17	17	0.2	106	8 DW	Over	3000	497	Unknown	50	33
5	17	1219	22-17	17	0.2	106	8 DW	Over	3000	497	Unknown	50	33
6	17	1223	23-17	2	0.1	106	8 DW	Over	1800	131	Unknown	50	33
7	17	1223	23-17	12	0.5	106	8 DW	Over	1800	131	Unknown	50	33
8	17	1230	24-17	5	0.1	226	8 DW	Over	3000	497	Unknown	50	33
9	17	1230	24-17	8	0.2	226	8 DW	Over	3000	497	Unknown	50	33
10	17	1230	24-17	17	0.5	226	8 DW	Over	3000	497	Unknown	50	33
11	17	1252	26-17	5	0.5	17	?	?	?	?	?	50	?
12	18	0951	1-18	3	0.5	116	14 DW	Over	2500	314	Bottom	50	37
13	18	1009	4-18	2	0.5	117	17 DW	3 DW	3100	497	Top	50	37
14	18	1009	4-18	2	0.2	117	17 DW	3 DW	3100	497	Top	50	37
15	18	1009	4-18	2	0.1	117	17 DW	3 DW	3100	497	Top	50	37
16	18	1009	4-18	7	0.5	117	17 DW	3 DW	3100	497	Top	50	37
17	18	1009	4-18	7	0.2	117	17 DW	3 DW	3100	497	Top	50	37
18	18	1142	6-18	5	0.5	244	5 UW	20 UW	1250 to 3750	Below 692	None§	50	--
19	21	0912	1-21	10	0.5	59	5 DW	Over	2800	446	Middle	100	47
20	22	0930	4-22	18	0.5	29	4 DW	Over	2700	429	Above(?)	100	61
21	22	0942	6-22	13	0.5	27	4 DW	Over	2100	246	Bottom	50	64
22	22	0944	7-22	13	0.2	28	4 DW	Over	2400	338	Middle	50	64
23	22	0945	8-22	2	0.5	28	4 DW	Over	2700	429	Above(?)	50	64
24	22	1233	12-22	7	0.5	?	4 DW	Over	2400	338	Middle	62	73

Notes: *DW = downwind, UW = upwind.

†Judging from MRI aircraft data and lidar cross sections.

§"Clear" air background upwind of stack.

Table V

VALUES OF OPTICAL PARAMETERS COMPUTED FROM RELATIVE PARTICLE-SIZE DATA

Count Number	ξ_e (m^2g^{-1})	ξ_b ($m^2g^{-1}ster^{-1}$)
1	0.63211	0.03647
2	0.64544	0.05744
3	0.70527	0.06434
4	0.56964	0.06138
5	0.85449	0.05519
6	0.36938	0.03603
7	0.93607	0.05103
8	0.97728	0.04638
9	0.55544	0.05882
10	0.51767	0.05197
11	0.59043	0.02630
12	0.32160	0.02109
13	0.37274	0.02622
14	0.47949	0.03176
15	0.45573	0.02401
16	0.54664	0.02836
17	0.84976	0.03571
18	0.39697	0.03233
19	0.35974	0.02950
20	0.21364	0.01382
21	0.51050	0.04480
22	0.25768	0.02137
23	0.38903	0.03518
24	0.68789	0.05680

It was indicated by MRI that the particle counting technique is insensitive to particles with radii less than 0.50 to 0.25 μ. The influence of this on the evaluated quantities, as well as the validity of the rectangular integration, was investigated by fitting a continuous Junge distribution function to the observed particle counts. Figure 32 illustrates the method used to evaluate the Junge parameters from the cumulative particle-size distribution of Count No. 21, which has been reduced to absolute values by the tentative MRI information. This particular sample has considerably fewer small particles ($a < 1.0\ \mu$) and also fewer large particles ($a > 3\ \mu$) than the indicated Junge model.

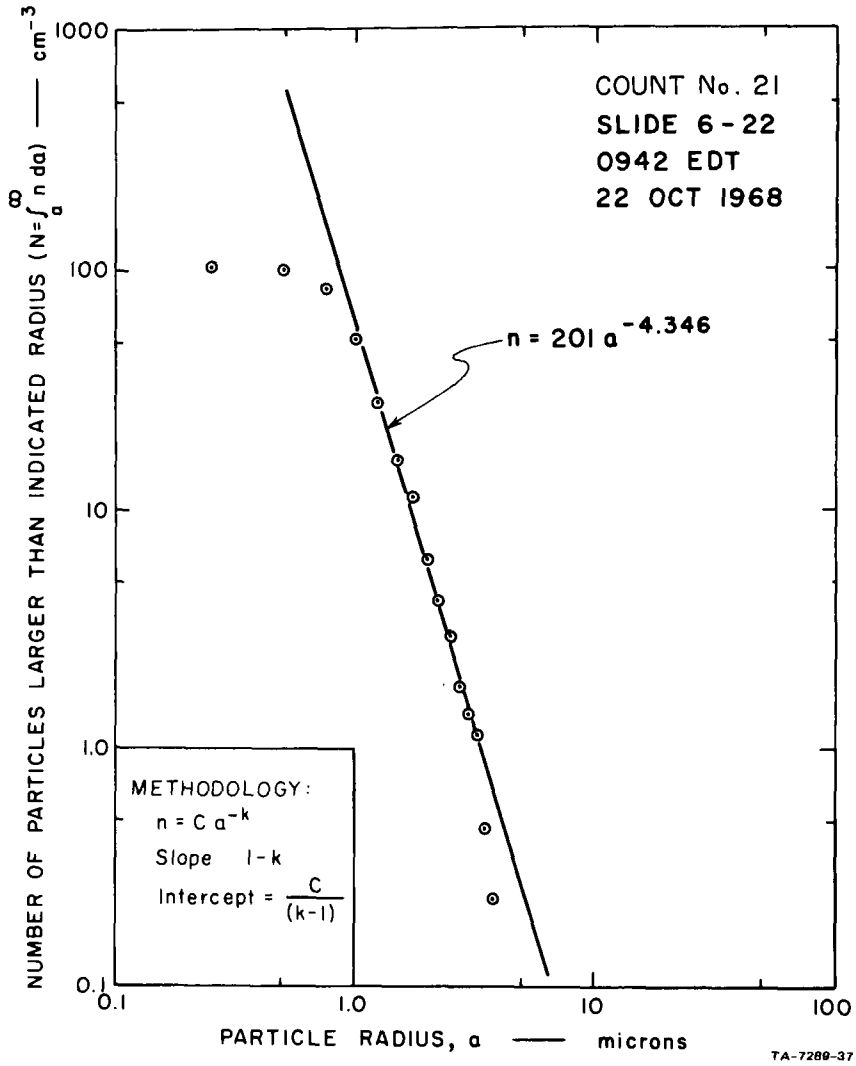

FIGURE 32 SAMPLE CUMULATIVE PARTICLE SIZE DISTRIBUTION AND JUNGE-TYPE ANALYTICAL FIT

Assuming that the Junge model is a satisfactory representation of the real aerosol, it can then be employed with a more exact trapezoidal integration of ξ_e (maintaining 0.1 increments in x). Integration with limits of a = 1.0 and 10.0 μ results in ξ_e = 0.37 m^2/g, slightly less than the rectangular integrated value (0.51), which is expected because of the increased number of larger particles in the Junge model. Integration with limits of a = 0.1 and 10.0 μ results in ξ_e = 0.87, the increase occurring because of the larger number of small particles in the Junge distribution.

The lidar and particle sampling of the Keystone plume were best coordinated for Cross Section 64, which is oriented approximately cross-wind, and this case was chosen to apply the mass concentration solution discussed in Sec. VII. The boundary parameter M_o was taken from the visibility estimate (7 to 10 miles), which gives $M_o = 100\ \mu g/m^3$, using the relationship of Noll, et al. (1968). The value of ξ_e was chosen in accordance with the computation (Table V) for Particle Count 22 as $0.2\ m^2/g$.* The results of these absolute mass concentration computations are presented in Fig. 33, which also illustrates the manner of the removal of extraneous clear-air and background noise contours from the plume cross sections, which is normally employed in order to better define the plume boundaries and shape. Figure 33(c) represents the results of the graphical subtraction of Fig. 33(a) from 33(b), and thus shows contours of mass concentration in decibels added to the back side of the plume by the attenuation correction. It may be noted that the maximum correction is 9 dB, which means that the mass concentration at that point was almost 10 times too low in the uncorrected cross section, Fig. 33(a). It may be seen that although the attenuation correction does change concentrations significantly in one part of the cross section, the general shape and structure of the plume remain the same.

A planimeter was used to integrate the total mass per unit plume length (cross-axial integrated mass concentration) represented by the cross sections in Fig. 33(a) and (b). The results were as follows: uncorrected cross section (a), 350 g/m of plume length; corrected (b),

---

*A value of $0.3\ m^2/g$ was tried also, but gave no solution due to the integration becoming unstable. Although solutions were not attempted for any other cross sections, many of the high values of ξ_e shown in Table IV would probably cause similar unsuccessful results. These high values are a consequence of the surprisingly small modal particle sizes reported by MRI. The cause of this apparent discrepancy between the lidar data and the particle-size data is unknown, but there are a number of possibilities, such as (1) the free-air particles could have a thin coating of water, which increases their optical size, (2) particle agglomerates may break up when introduced into the sampler, (3) some of the assumptions used in the lidar data analysis may be faulty, or (4) there may be an error in the particle-size measurements or analyses.

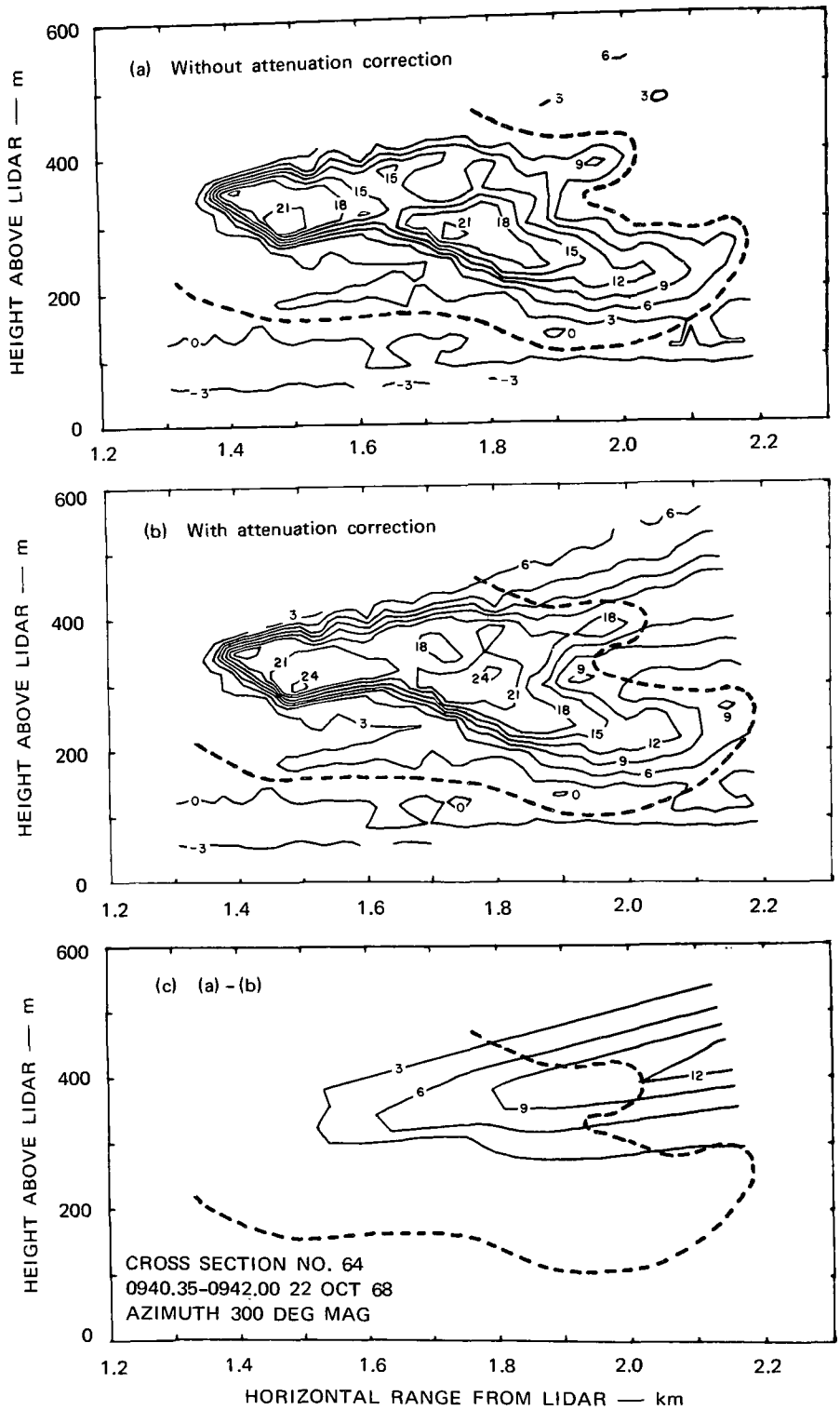

FIGURE 33 EFFECT AND MAGNITUDE OF CORRECTION OF PLUME MASS CONCENTRATION DISTRIBUTIONS FOR ATTENUATION. Contours represent 10 $\log_{10}$ (M/M_o) and thus are labelled in decibels. Solution parameters for (b) are clear-air concentration M_o = 100 x 10^{-6} g/m^3; ξ_e = 0.2 m^2/g; dashed line faired in by hand separates clear-air and background-noise contours from plume contours.

680 g/m, which shows that the mass correction was significant. These values were compared with an estimate of the particulate emission rate from the stack, obtained from the following parameters existing at the time the cross section was obtained:

Coal burning rate = 651×10^3 lb/hr

Fly ash content of coal = 17 percent*

Precipitator collection efficiency = 50 percent (half in operation)

Wind speed at plume level = 8 m/s.

Using these values gives a stack source strength of 7000 g/s, and a plume cross-axial integrated mass concentration of 875 g/m, compared with the 680 g/m measured by the lidar, after allowance for attenuation Although further evidence will be necessary from other comparisons, the close agreement of this initial example does indicate strongly that the lidar technique is capable of useful quantitative measurements.

*Full conversion to gas-borne fly ash particles is assumed.

IX RECOMMENDATIONS FOR FURTHER RESEARCH

This first feasibility study, although limited in scope and scale of effort, has demonstrated that lidar is of significant value in plume studies. The instrument can furnish information about plume rise and dispersion from tall stacks that is unobtainable in such detail by any other means. To take advantage of the full potential of the technique, additional work is needed in a number of areas. These fall for the most part within the general categories of

(1) Lidar instrumentation improvements,

(2) Additional data-handling and reduction capabilities,

(3) Improved experimental and analytical techniques, and

(4) Testing of advanced lidar concepts.

A number of specific suggestions for improving lidar usefulness in plume studies are itemized below.

A. Lidar Instrumentation

- The observations described in this report were made with SRI's general-purpose experimental Mark V lidar operating in its neodymium configuration. Although this provided a higher pulse repetition frequency (10-12 pulses/min) than the ruby version, the latter system is more sensitive and could thus have acquired data at longer ranges, or better information on "clean" plumes (i.e., with full precipitator operation). The lower pulse rate of the ruby system (3-4 pulses/min) would have seriously reduced the data rate.

These considerations well illustrate the problem confronting the designer of an optimum system for use in plume observations. It is important to recognize, however, that the SRI Mark V lidar is a relatively modest unit, and that with current technology considerably higher performance is readily attainable. The results of the present investigation, even allowing for the limitations of the equipment, are so

encouraging that the development of a more advanced lidar system appears to be fully justified.

Such a system could be readily developed with state-of-the-art technology based upon the experience of the present study. In selecting an optimum system, it would be necessary to investigate carefully the relative advantages of lasers of different wavelengths. Prime candidates are 0.694 μ (ruby), 0.9 μ (gallium arsenide), near infrared at 1.06 μ (neodymium glass and YAG--ytrrium aluminum garnet), or 0.53 μ (the second harmonic of the latter), all of which are immediately available. In making the choice, the factors of pulse repetition rate, availability of adequately sensitive detectors, and, of course, cost would all have to be carefully weighed.

Although at the moment indications are that a well-cooled ruby laser system* with a PRF of 1 to 10 pulses per second would provide the best compromise, a detailed systematic study would be a most valuable preliminary to building an advanced lidar system for plume studies.

- A study should be made of the feasibility of calibrating the lidar on an absolute basis so that the energy output (in joules) of each pulse were known. A completely calibrated lidar could furnish objective estimates of one of the attenuation solution parameters, M_o, the absolute particulate mass concentration in the clear air.

B. Data Handling and Reduction Capabilities

- Even at the present lidar firing rates, the large quantity of data collected is on the verge of becoming unmanageable. Each lidar observation is not just a point measurement, but a complete profile. Making full use of this information, particularly when using higher-PRF instruments, requires new and better ways of handling and processing lidar data.

---

*Recent tests with the SRI Mark V ruby system indicate that relatively modest improvements could permit it to be operated at a pulse rate comparable to that of the neodymium version, which could make this system an excellent interim solution.

- A big step in the right direction would be the development of an intensity-modulated range-height oscilloscope display of plume cross sections. This would be similar to the familiar radar RHI display, as simulated in Fig. 34, and would give an immediate, operationally useful photograph showing the plume shape and boundaries, as well as the internal relative concentration distribution in terms of varying degrees of brightness. For a more quantitative record, the video magnetic disk recorder would be used to take photos of the same cross section with

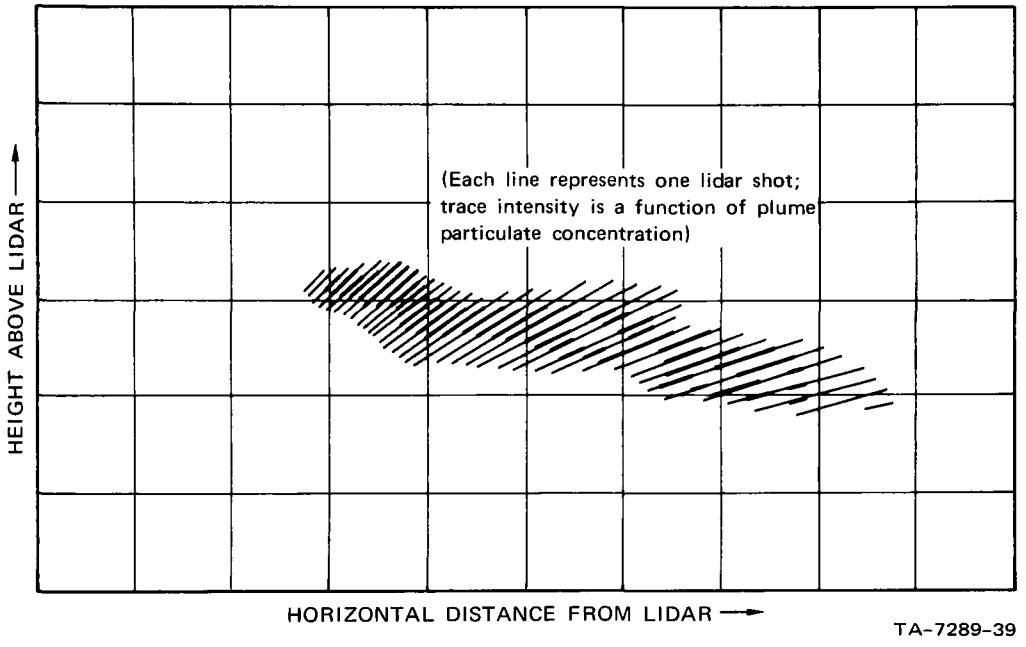

FIGURE 34 VISUALIZATION OF INTENSITY-MODULATED RANGE/HEIGHT OSCILLOSCOPE DISPLAY OF PLUME CROSS SECTION OBSERVED BY LIDAR

different oscilloscope intensity settings, giving a contour representation. Such a display would require that each lidar observation be corrected electronically for range and for equipment nonlinearities. These real-time analog techniques would greatly simplify the data-processing problem and reduce the number of digital computer analyses required.

- Since some of the lidar data will always need to be retained in quantitative form, an on-line analog-to-digital conversion and recording capability in the field would vastly facilitate later digital analyses.

C. Experimental and Analytical Techniques

- For better time continuity of the lidar plume observations, the limitations on duration of the observation periods, which were in effect during the experimental phase of this study, are undesirable and future arrangements should permit uninterrupted operations, if at all possible.

- Observations should also be obtained during the night hours, when lidar performance is optimum due to the low background illumination (noise) levels.

- Most of the effort in this study went into lidar data collection, processing, and analysis. More work is needed on the interpretation and use of plume cross sections in checking plume rise formulas, testing diffusion models, studying terrain effects, etc.

- In particular, a rationale is needed to deal with the effect of the background noise threshold in plume cross sections upon the testing of diffusion models using lidar data. This methodology could be similar to that developed by Gifford (1959) for use in diffusion estimates from smoke plume photography.

- Some provision for time averaging of the lidar data is required for use in testing diffusion models, which generally are designed to furnish one-half- to one-hour averages. This capability is especially needed for checking models for neutral and unstable conditions. It is possible that an analog means to do this can be devised using the previously discussed intensity-modulated range-height display.

- In future absolute concentration analyses, an attempt should be made to treat ξ_e, the ratio of the optical volume extinction coefficient to particle mass, as a variable with range.

D. Advanced Lidar Concepts

- There is great potential for exploiting the wavelength characteristics of laser energy in lidar applications for plume studies. Two possibilities warrant early investigation:

(1) The use of multiwavelength systems to determine absolute mass concentrations without independent information of the particle size distribution, and

(2) The extension of the multiwavelength differential absorption technique that has been applied to the determination of water-vapor (Schotland et al., 1962) to the evaluation of plume constituents.

In this connection the development of new types of lasers, such as the tunable dye laser, holds great promise.

REFERENCES

Barrett, E. W., and O. Ben-Dov, 1967: Applications of the lidar to air pollution measurements. J. Appl. Meteor., 6, 500-515.

Gifford, F. A., Jr., 1959: Smoke plumes as quantitative air pollution indices. Intern. J. Air Poll., 2, 42-50.

Gifford, F. A., Jr., 1961: Use of routine meteorological observations for estimating atmospheric dispersion. Nuclear Safety, 2, 48.

Goetz, A., 1969: A new instrument for the evaluation of environmental aerocolloids. Envir. Science and Tech., 3, 154-160.

Hamilton, P. M., 1966: The use of lidar in air pollution studies. Intern. J. Air and Water Poll., 10, 427-434.

Johnson, W. B., Jr., 1969: Lidar applications in air pollution research and control. J. Air Poll. Contr. Assoc., 19, March 1969.

McCormick, R. A., and K. R. Kurfis, 1966: Vertical diffusion of aerosols over a city. Quart. J. Roy. Meteor. Soc., 92, 392-396.

Noll, K. E., P. E. Mueller, and M. Imada, 1968: Visibility and aerosol concentration in urban air. Atmos. Envir., 2, 465-475.

Proundfit, B. W., 1969: Plume rise from Keystone Plant. Final Report, Contract PH 86-68-94, Sign X Laboratories, Inc., Essex, Connecticut.

Schotland, R. M., A. M. Nathan, E. A. Chermack, and E. E. Uthe, 1962: Optical sounding. Tech. Rpt., Contract DA 36-039 SC-87299, U.S. Army Electronics Research and Development Laboratory.

Smith, M. E. (Editor), 1968: Recommended Guide for the Prediction of the Dispersion of Airborne Effluents. American Society of Mechanical Engineers, 345 E. 47th Street, New York.

Appendix A

DESCRIPTION OF MARK V LIDAR

Appendix A

DESCRIPTION OF MARK V LIDAR

The optical system of the Mark V lidar is illustrated in Fig. A-1. The transmitter consists of a Q-switched, air-cooled, pulsed ruby or neodymium-doped glass laser with wavelengths at 6943 Å* (deep red) or at 10,600 Å (near infrared), respectively. Since the angular resolution of the lidar is determined by the transmitted beam divergence, 6-inch-diameter collimating optics are used to reduce the laser beam divergence and to produce an output beamwidth of 0.35 mrad. The corresponding spatial resolution of this beam is 0.50 m at a range of 1 km in the cross-beam direction, and about 2.3 m in range. The pulse repetition rate of the Mark V lidar is primarily limited by the cooling rate of the laser cavity. At present, the maximum firing rate is 3 to 4 pulses per minute for the ruby laser, and 10 to 12 pulses per minute for the neodymium. The characteristics of the Mark V lidar are summarized in Table A-I.

The lidar receiver consists of a 6-inch-diameter Newtonian telescope, identical to the transmitter optics. An adjustable field stop at the focal plane limits the receiver field of view to a maximum of 6 mrad. A multilayered narrow-band filter with a wavelength interval (bandwidth) of 13 Å (ruby) or 100 Å (neodymium) is inserted in the receiver optical path to reduce the output noise level produced by solar radiation scattered into the receiver field of view. The detector consists of an RCA 7265/S-20 photomultiplier tube for the ruby laser, and an RCA 7102/S-1 for the neodymium system.

The major electronic components of the lidar and the data-recording system are illustrated in the block diagram shown in Fig. A-2. A compressed-air-driven turbine rotates the laser Q-switching prism at

---

*10^4 Å = 1 μ.

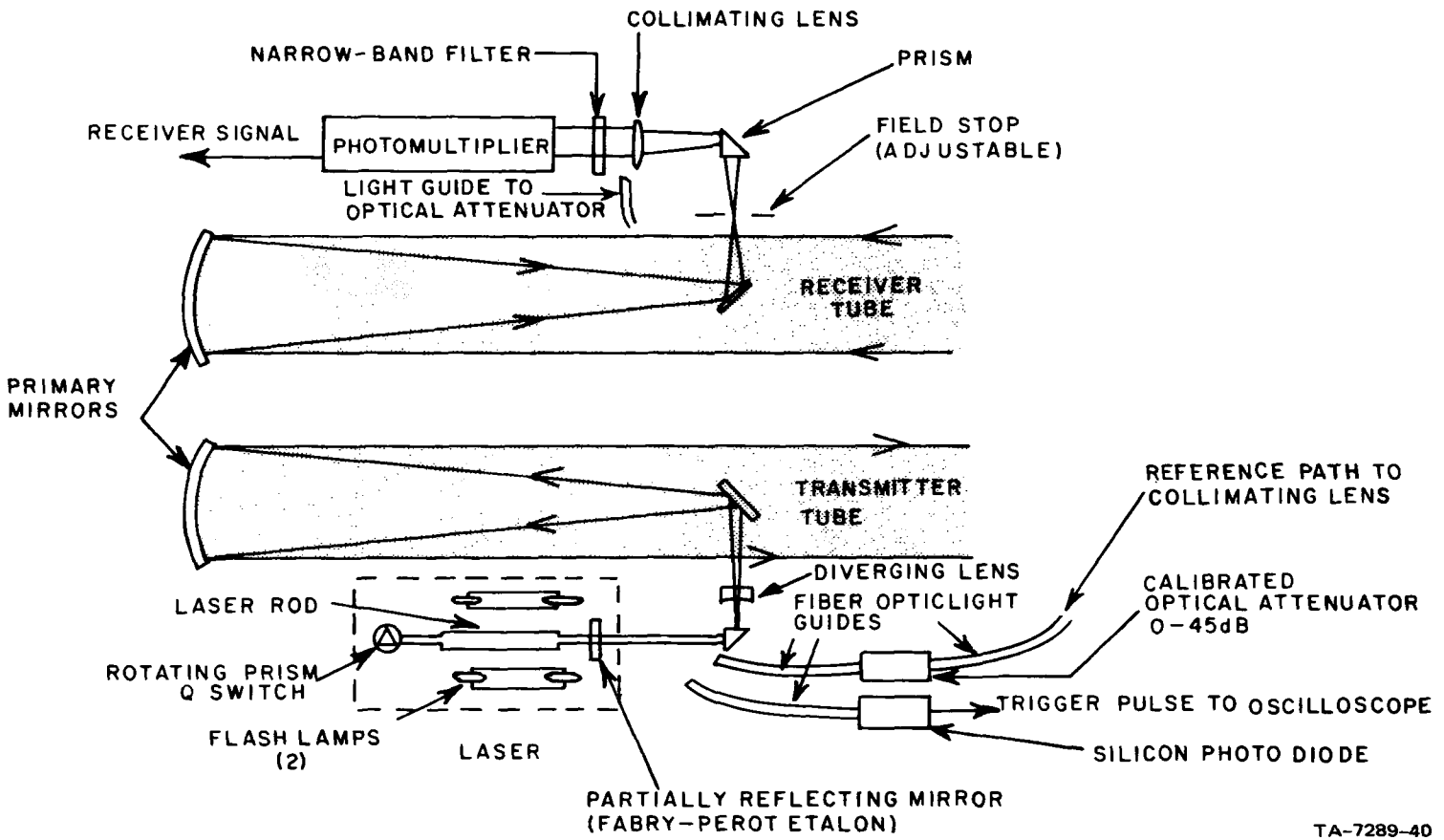

FIGURE A-1 OPTICAL SYSTEM OF MARK V LIDAR

Table A-I

CHARACTERISTICS OF SRI MARK V LIDAR

Characteristics	Wavelength	
	6943 Å	10,600 Å
Transmitter		
Laser Material	Ruby	Neodymium-Glass
Beamwidth (mrad)	0.35	0.2
Optics	6-inch f/4 Newtonian Reflector	
Peak Power Output (MW)	15	50
Pulse Length (ns)	15	12
Q Switch	Rotating Prism	Rotating Prism
Maximum PRF (pulses/min)	3 to 4	10 to 12
Receiver		
Optics	6-inch Newtonian Reflector	
Field of View (mrad)	1.5	3.0
Predetection Filter Wavelength Interval (Å)	13	100
Detector	RCA 7265 (S-20 Cathode)	RCA 7102 (S-1 Cathode)
Postdetection Filter Bandwidth (MHz)	30	30

500 revolutions per second. Upon receipt of a fire signal, the synchronizing generator triggers the flash lamp in step with a signal from the rotating prism. A capacitor bank charged to 3 kV supplies energy for the laser flash lamps. A photodiode senses the occurrence of the laser pulse and produces a trigger pulse to start the oscilloscope sweep. The output of the photomultiplier in the lidar receiver is fed to a pulse amplifier having a logarithmic transfer function, and then to an oscilloscope. A Polaroid recording camera mounted on the oscilloscope photographs the lidar return signal. Other data-recording options available include the use of an automatic recording 35-mm camera and a magnetic disk video recorder. The latter device furnishes a steady display on the face of the oscilloscope immediately after each shot, as well as a permanent record, and is very useful for real-time monitoring of observations.

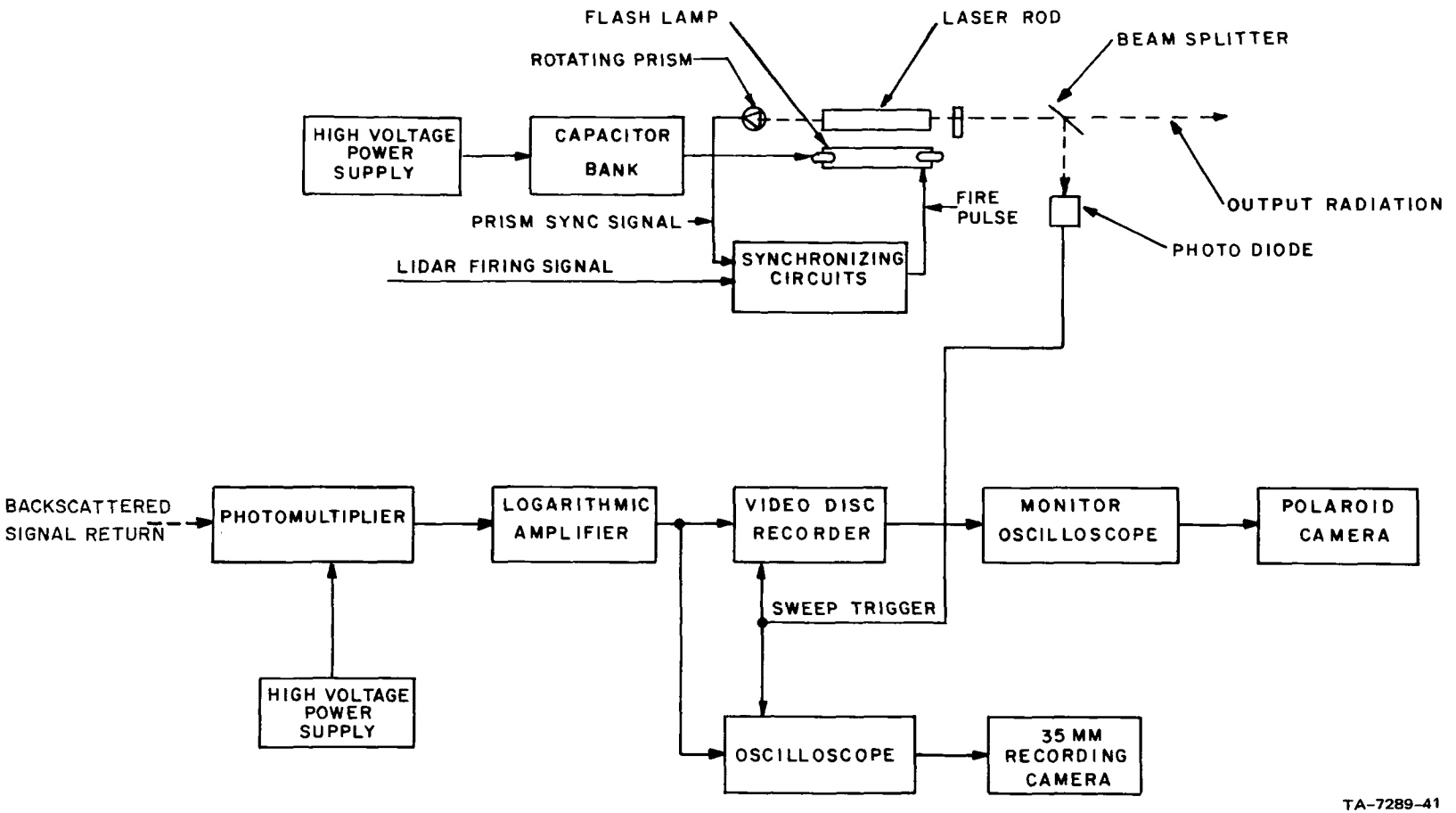

FIGURE A-2 ELECTRONICS SYSTEM OF MARK V LIDAR

Although the pulse-to-pulse variations of laser power output are not unduly severe, the presence of this random variation introduces a corresponding uncertainty in the amplitude of the received signal unless provision for monitoring the transmitter power is made. The Mark V lidar incorporates an optical feedback arrangement, using fiber-optic light guides, that samples the transmitted energy and injects it into the receiver optical path ahead of the narrow-band predetection filter (see Fig. A-1). This arrangement produces a pulse occurring at zero range on the receiver output. The pulse height is proportional to transmitted power. A variable neutral-density filter is inserted in the fiber-optic path to allow adjustment of the pulse height.

The use of a logarithmic video amplifier in the receiver is almost essential in order to compress the wide dynamic range of the detector (typically four or more orders of magnitude) to enable the received signal to be displayed on a single oscilloscope trace without loss of detailed information.

Appendix B

DETAILED LIDAR DATA SUMMARIES

Table B-I

DATA SUMMARY, 25 MAY-1 JUNE 1968

Date (1968)	Site No.	Observational Period No.	Cross Section No.	Azimuth Angle	Elevation Angle (First)	Time (Start) (EDT)	Elevation Angle (Last)	Time (End) (EDT)	Elevation Angle Increment	No. of Lidar Shots	Subtotal No. of Shots	Weather, Remarks
5/25	1	1	1	045	13	0912:30	6	0916:00	1/2	15		0800: ○ 1/4 GF C
			2	000	25	0917:30	11	0921:00	1	15		0900: ○ 7 L/V
			3	315	21	0922:00	7	0925:25	1	15		Plume Hdg ~ 245°
		2	4	000	30	1034:00	4	1039:45	1	27		
			5	045	16	1040:15	4	1043:30	1	13		
			6	315	23	1045:00	4	1048:00	1	20		
		3	7	000	89	1423:00	7	1428:00	3	28		1400: /◍ 15 140/5
			8	045	89	1431:00	5	1435:00	3	29		Plume Looping
			9	315	89	1437:00	5	1442:15	3	29		
			10	045	60	1448:00	3	1453:00	3,1	28	219	
5/26	2	4	11	200	9	0854:00	1	0856:15	1/2	17		0800: 100◍/◍10 090/5
			12	226	16	0858:00	3	0902:40	1/2	26		Plume Hdg ~ 315°
			13	252	20	0904:30	5	0906:30	1	16		
			14	253	15	0908:45	5	0913:00	1/2	20		
			15	226	15	0915:45	6	0918:00	1/2	19		
			16	200	9	0921:00	1	0926:00	1/2	29		
		5	17	200	13	1145:30	5	1148:30	1/2	29		1000:100◍v◍/◍ 7 090/10
			18	226	30	1151:30	22	1153:00	1	9		
			19	226	30	1154:30	4	1158:30	1	27		Plume Looping
			20	226	30	1200:30	4	1204:15	1	27		
			21	226	30	1205:00	4	1208:30	1	27	465	
5/27	3	6	22	065	12	0908:10	3	0912:00	1/2	19		0800:E25 ⊕ 4R-090/15G25
			23	032	25	0913:15	1	0916:45	1	25		Plume Hdg 270-290°
			24	000	24	0918:00	1	0922:00	1	24		
			25	065	15	0923:00	2	0927:00	1/2	27		
			26	032	25	0928:00	1	0931:30	1	25		
			27	000	24	0932:20		0935:20	1	24		
		7	28	065	15	1013:45	2	1018:15	1/2	28		
			29	032	25	1019:45	2	1022:45	1	24		
			30	000	20	1024:00	2	1026:45	1	21		
			31	065	15	1035:30	0	1039:30	1/2	30		
			32	032	25	1040:30	2	1043:45	1	24		
			33	000	24	1045:45	2	1049:00	1	23	759	
5/28	4	8	34	020	89	0909:45	3	0913:00	3	30		0800:E35⊕8 090/5

Table B-I (Continued)

Date (1968)	Site No.	Observational Period No.	Cross Section No.	Azimuth Angle	Elevation Angle (First)	Time (Start) (EDT)	Elevation Angle (Last)	Time (End) (EDT)	Elevation Angle Increment	No. of Lidar Shots	Subtotal No. of Shots	Weather, Remarks
5/28	3	9	35	065	20	1113:30	3	1116:00	1	19		(Plume overhead,
			36	032	25	1116:30	3	1119:45	1	23		shifting EWD, so moved
			37	000	25	1121:00	3	1123:30	1	23		to Site 3)
			38	333	25	1126:40	4	1128:00	1	22		Plume turning into water
			39	065	20	1135:45	3	1138:00	1	18		cloud
			40	032	25	1139:45	2	1142:20	1	24		1200:E12⊕3R--F 090/10
			41	000	25	1143:30	2	1147:00	1	24		
			42	333	25	1148:20	4	1150:00	1	22	964	
5/29	5	10	43	350	15	0855:30	2-1/2	0859:00	1/2	26		0830:E50 ⊕ 5HGFC
			44	030	15	0900:00	2	0903:45	1/2	28		Plume moving to ESE
			45	070	12	0905:00	4	0908:15	1/2	17		
			46	030	12	0912:15	2	0915:15	1/2	22		
		11	47	350	20	1208:15	2	1209:30	2	10		
			48	350	20	1210:10	2	1212:30	1	19		
			49	020	20	1213:30	2	1215:45	1	19	1105	
5/30	2	12	50	117	28	0844:00	4	0848:00	1	25		0845: -X10 ⊕ 1/4R-FC
			51	117	25	0945:15	5	0948:30	1	23		0945: E10 ⊕ 2R--FC
			52	117	28	1018:15	4	1021:15	1	25	1178	1015: E8 ◍ 50 ⊕ 3R--
												F 200/4
5/31	6	13	53	228	10	0820:30	1-2/3	0823:30	1/3	27		0800: E10 ⊕ 5H 220/3
			54	199	15	0824:45	2	0827:15	1/2	27		Plume becoming water
			55	170	15	0828:15	3-1/2	0830:40	1/2	24		cloud
			56	199	15	0831:15	1-1/2	0824:25	1/2	28		0900: A 13 ◍ 25 ⊕ 5H
		14	57	228	15	0935:15	3-1/3	0938:45	1/2,1/3			(Chopper report)
			58	199	20	0940:15	3	0943:45	1/2	34		
			59	170	20	0944:45	3-1/2	0948:15	1/2	29	1378	
6/1	6	15	60	170	90	1018:00	15	1020:45	5	18		Ground fog till 1000
			61	350	85	1025:00	6	1027:30	5,3,2,1	23		Plume overhead
			62	215	90	1030:00	12	1032:15	5,3	19		
			63	305	90	1034:00	6	1037:00	5,3,1	24		Plume rising almost
			64	260	90	1041:00	5	1043:30	5,3,2,1	25		vertically and then
												spreading horizontally--
												wind light/variable
Total No. of Shots											1487	

Table B-II

DATA SUMMARY, 15-24 OCTOBER 1968

Date (1968)	Site No.	Observational Period No.	Cross Section No.	Azimuth Angle	Elevation Angle (First)	Time (Start) (EDT)	Elevation Angle (Last)	Time (End) (EDT)	Elevation Angle Increment	No. of Lidar Shots	Subtotal No. of Shots	Weather, Remarks
10/15	6	1	1	270	45	0932:00	3	0936:04	2	22		0915: ◯ 3 GF
			2	300	50	0939:00	4	0943:11	2	26		Plume Hdg 022°
			3	330	50	0945:30	2	0949:40	2	26		
			4	270	40	0955:00	2	0957:50	2	20		
			5	300	40	0959:00	2	1002:25	2	20		
			6	330	36	1004:40	2	1007:25	2	18		
			7	270	30	1032:30	2	1034:40	2	15		
			8	300	50	1036:30	2	1041:00	2	25		
			9	330	36	1044:00	2	1047:00	2	18		
			10	300	40	1059:20	2	1102:20	2	20		
			11	300	44	1116:00	2	1118:50	2	22		Strong vertical wind
			12	300	70	1138:00	1	1141:30	3,2	25		shear in direction
			13	300	70	1143:00	1	1145:45	3	24		
			14	300	70	1147:00	1	1150:00	3,2	25	306	1156: ◯ 5-7H
												light/variable
10/16	16	2	15	145	90	0852:20	40	0855:00	5	11		
			16	100	90	0916:00	5	0918:15	5	18		
			17	55	90	0920:20	45	0923:00	5	12		
			18	100	90	0934:00	5	0937:00	5	18		
			19	100	90	0938:30	5	0941:50	5,2	24		
			20	100	90	0943:15	6	0946:20	5,2	26		0945: ◯ 7 HK 360/5
		3	21	255	30	1149:30	2	1151:30	2	15		1145: ◯ 8H 135/8
			22	230	30	1153:20	2	1155:45	2	15		
			23	230	36	1157:30	1	1159:00	2,1	19		
			24	230	15	1200:10	1	1203:00	1	15		
			25	230	20	1204:00	1	1206:25	1	20	499	
10/17	16	4	26	090	15	0903:30	90	Msg.	5	16		
			27	090/270	15	0910:00	6	0914:25	5,2	33		Plume Hdg 360°
			28	090/270	15	0916:30	6	0922:20	5,2	34		
			29	090/270	15	0928:00	5	0934:35	5,2,1	35		0927: E60 ◍/◍ 8 090/5
			30	090/270	15	0936:00	5	0942:20	5,3,2	33		Plume overhead
		5	31	090/270	3	1151:15	5	1157:15	5,3,1	33		1216: 120◍ 8 060/8
			32	090/270	5	1201:45	5	1207:10	5,4,3,2	29		
			33	090/270	15	1212:00	5	1216:25	5,4,3,2	27	739	

Table B-II (Continued)

Date (1968)	Site No.	Observational Period No.	Cross Section No.	Azimuth Angle	Elevation Angle (First)	Time (Start) (EDT)	Elevation Angle (Last)	Time (End) (EDT)	Elevation Angle Increment	No. of Lidar Shots	Subtotal No. of Shots	Weather, Remarks
10/18	17	6	34	080/260	3	0917:20	3	0922:15	5,4,3	34		0900: 80 ◍/◍8 110/8
			35	080/260	3	0928:20	3	0932:30	5,4,3,2	33		Plume overhead
			36	080/260	3	0935:20	3	0939:45	5,4,3	33		
			37	080/260	3	0941:00	3	0944:20	5,4,3	33	872	1100: 15◑80 ◍/◍8 130/10
10/20	21	7	38	200/020	3	0909:00	2	0914:45	5,4,3,2	35		0900: ◯15
			39	200/020	45	0916:15	2	0919:00	5,3,2	24		
			40	200/020	14	0928:00	2	0932:00	5,2	34		
			41	200/020	14	0937:00	2	0941:30	5,2	34		0945: ◯ 15 160/7
		8	42	200/020	2	1018:00	1	1024:20	5,2	42		1015: ◯ 5H
			43	200/020	20	1038:30	10	1040:50	10	16	1057	1100: ◯ 5H 220/10
10/21	22	9	44A	270	24	0854:00	5	0855:40	2,1	17		0830: 50◯6H 270/3
			44B	225	26	0856:40	8	0858:35	2,1	18		
			45	180	16	0859:30	3	0901:20	1	14		
			46	270	24	0903:00	5	0904:40	2,1	16		
			47	225	26	0906:30	6	0908:20	2,1	18		
			48	180	16	0909:30	4	0910:50	1	13		
			49	225	26	0921:30	9	0923:40	2,1	17		
			50	180	16	0925:00	5	0926:00	2,1	10		
			51	225	26	0928:00	9	0929:40	2,1	18		
			52	270	24	0930:30	7	0932:15	2,1	14		
			53	225	26	0934:00	9	0935:40	2,1	15		0945: 40◑V◍6H 135/5
		10	54	270	45	1023:00	2	1025:55	3,2,1	24		
			55	225	60	1027:30	3	1030:30	5,3,2,1	26		
			56	180	60	1033:20	2	1036:50	5,3,2,1	27	1304	1100: 25◑50◍8 290/10
10/22	6	11	57	270	15	0900:00	2	0901:20	1	14		0840: /◑ 7 GF
			58	300	16	0903:00	3	0904:30	1	14		Plume Hdg 020°
			59	330	15	0905:20	2	0907:30	1	14		
			60	270	15	0921:45	3	0923:10	1	13		
			61	300	16	0923:50	3	0925:10	1	14		
			62	330	15	0925:45	3	0927:00	1	13		
			63	270	15	0938:30	2	0939:45	1	14		
			64	300	15	0940:35	2	0942:00	1	14		1015: /◍ 7 080/5
			65	330	15	0943:45	2	0945:15	1	14		1015: undulations on top of plume

Table B-II (Continued)

Date (1968)	Site No.	Observational Period No.	Cross Section No.	Azimuth Angle	Elevation Angle (First)	Time (Start) (EDT)	Elevation Angle (Last)	Time (End) (EDT)	Elevation Angle Increment	No. of Lidar Shots	Subtotal No. of Shots	Weather, Remarks
10/22		12	66	270	20	1134:00	2	1136:10	2,1	17		
			67	300	20	1137:00	3	1138:30	2,1	15		1140: /◍7 090/10
			68	330	20	1139:15	3	1140:40	2,1	15		
			69	270	20	1151:50	1	1153:25	2,1	18		1050: Plume looping
			70	300	20	1154:15	0	1157:30	1	25		
			71	330	30	1158:45	3	1201:50	2,1	27		1205: /◍8 090/10
			72	270	26	1227:00	1	1229:15	2,1	19		
			73	300	30	1231:00	1	1233:00	2,1	20		
			74	330	40	1234:45	2	1236:55	3,2,1	20		
			75	300	34	1238:30	2	1240:30	2	17		
			76	300	30	1241:15	2	1242:50	2	15		1245: /◍8 090/10
			77	300	30	1243:45	2	1245:05	2	15	1665	
10/23	6	13	78	220	16	0850:15	1-1/2	0853:15	1,1/2	28		0845: /-◍ 10 315/10
			79	220	18	0856:45	2	0858:30	1	17		
			80	180	26	0859:45	2	0901:45	2,1	17		Plume Hdg 080°
			81	140	24	0902:40	5	0904:45	2,1	18		Fairly strong winds at
			82	220	20	0909:00	2	0911:20	1	19		plume level
			83	180	20	0912:45	1	0915:50	1	20		Cu forming at top of
			84	140	26	0916:00	5	0918:00	2,1	18		plume
		14	85	220	22	0941:20	2	0943:45	2,1	20		0945: /-◍ 10 315/15
			86	180	26	0946:30	2	0949:40	2,1	21		
		15	87	220	24	1155:00	2	1157:40	2,1	19		1130: 40◍V◍10 270/12
			88	180	30	1158:45	1	1201:20	2,1	23		
			89	140	45	1206:00	5	1209:30	5,3,2,1	17		
			90	190	50	1218:00	1	1220:30	3,2,1	22		
			91	180	90	1223:45	2	1227:10	5,3,2	27	1951	
10/24	11	16	92	110	30	0930:00	3	0932:30	2,1	21		Plume Hdg 340°
			93	070	34	0933:15	2	0934:40	2	17		0945: 80 ◍160 ⊕ 5H
			94	030	26	0936:00	5	0937:05	2,1	16		135/5
			95	110	22	0938:30	5	0940:00	2,1	15		
			96	070	30	0941:00	4	0942:30	2	14		
			97	030	34	0943:30	2	0945:20	2	17		
			98	070	30	1002:00	5	1003:40	2,1	17		
			99	070	26	1004:40	5	1006:00	2,1	15		
			100	070	34	1017:45	9	1019:30	2,1	17		
			101	070	34	1020:00	6	1021:45	2,1	20		

Table B-II (Continued)

Date (1968)	Site No.	Observational Period No.	Cross Section No.	Azimuth Angle	Elevation Angle (First)	Time (Start) (EDT)	Elevation Angle (Last)	Time (End) (EDT)	Elevation Angle Increment	No. of Lidar Shots	Subtotal No. of Shots	Weather, Remarks
10/24	11	16	102	070	30	1032:30	9	1034:10	2,1	15		
			103	070	30	1035:15	8	1037:50	2,1	22		
			104	070	38	1047:30	5	1050:30	2,1	28		
			105	070	36	1051:30	6	1053:25	2	16		
			106	070	46	1103:30	4	1105:45	2	22		
			107	070	46	1117:30	2	1119:50	2	23		
			108	070	90	1134:00	8	1136:30	10,5 3,2	23		
			109	070	90	1145:45	4	1151:35	10,5 3,2	25		1150: 80◐160⊕5H 180/10
			110	070	90	1202:00	4	1204:45	10,5 3,2	25	2319	

Appendix C

LIDAR DATA DIGITIZING AND CONDITIONING DETAILS

Appendix C

LIDAR DATA DIGITIZING AND CONDITIONING DETAILS

(by C. E. Brabant)

1. Photographic Processing

The lidar returns were recorded on Polaroid photographs and on magnetic disk tracks in analog form. These signals were then reproduced from the magnetic recordings and displayed repetitively on the screen of a standard laboratory oscilloscope (Tektronix Model 555). A photographic transparency on 35-mm film was made of each oscilloscope trace with an illuminated graticule superimposed on the background to provide reference axes for scaling the photograph. The time scales used in the photographic frames were 2 μs/cm (3-km range full scale), and when appropriate, 5 μs/cm (7.5-km range full scale). The vertical amplitude scale was set at 100 mV/cm.

2. Graphical-to-Digital Conversion

A Model 300 CALMA Co. digitizer was used to convert the optically enlarged photographic trace to numerical increments recorded on digital magnetic tape. The data on the photographs were automatically digitized when the cursor was manually traced over the image of the lidar return signal amplitude. Scaling was performed at the beginning of each digitizing-recording session and immediately preceding a change in scale whenever this occurred.

Engineering values in millivolts and microseconds were entered via the digitizer keyboard, as were all other special control characters. These were recorded on magnetic tape along with the records of the incremental digital values describing the X and Y Cartesian coordinates of the analog signal. These values were recorded for equal increments in time at a resolution of approximately 25 ns, corresponding to 3.8 m in range. The vertical scale resolution was 0.75 mV. General accuracy obtained in curve tracing is estimated to be no worse than one-half of

the trace width, which varied from approximately 10 to 20 mV, although it is possible that larger deviations from the curve occurred infrequently.

3. Transformation to Engineering Units and Conditioning

A standard CDC 6400 computer program developed by the CALMA Co. was used to recover the data, scaled in engineering units. Much of the data required special handling because of operator errors in entering control characters via the keyboard, foot-treadle, and console pushbuttons of the digitizer. This step produced the first intermediate digital magnetic tape and a control listing of the decimated data points. This listing also provided data for verifying the scaling factors used to convert incremental values into scaled engineering values.

A pair of special CDC 6400 computer programs were developed to select data between predetermined starting and ending ranges (travel time values for lidar return signals) at equally spaced intervals. Adequate spatial resolution was obtained by selecting every fifth point in the data record, yielding an increment of approximately 100 ns (15-m range) between selected sample points. The second program of the pair listed the entire output tape, point-by-point, as a check for subsequent processing.

Appendix D

PLAN VIEWS OF HORIZONTAL PLUME POSITIONS FROM LIDAR OBSERVATIONS

Appendix D

PLAN VIEWS OF HORIZONTAL PLUME POSITIONS FROM LIDAR OBSERVATIONS

To help clarify the plume cross sections from the October period that are presented in Sec. V, plan views of horizontal plume positions derived from these cross sections are shown on the following pages (Figs. D-1 to D-9). By referring to these plan views, the elongation in the cross sections caused by the lidar azimuth angle being nonperpendicular to the plume axis may be determined.

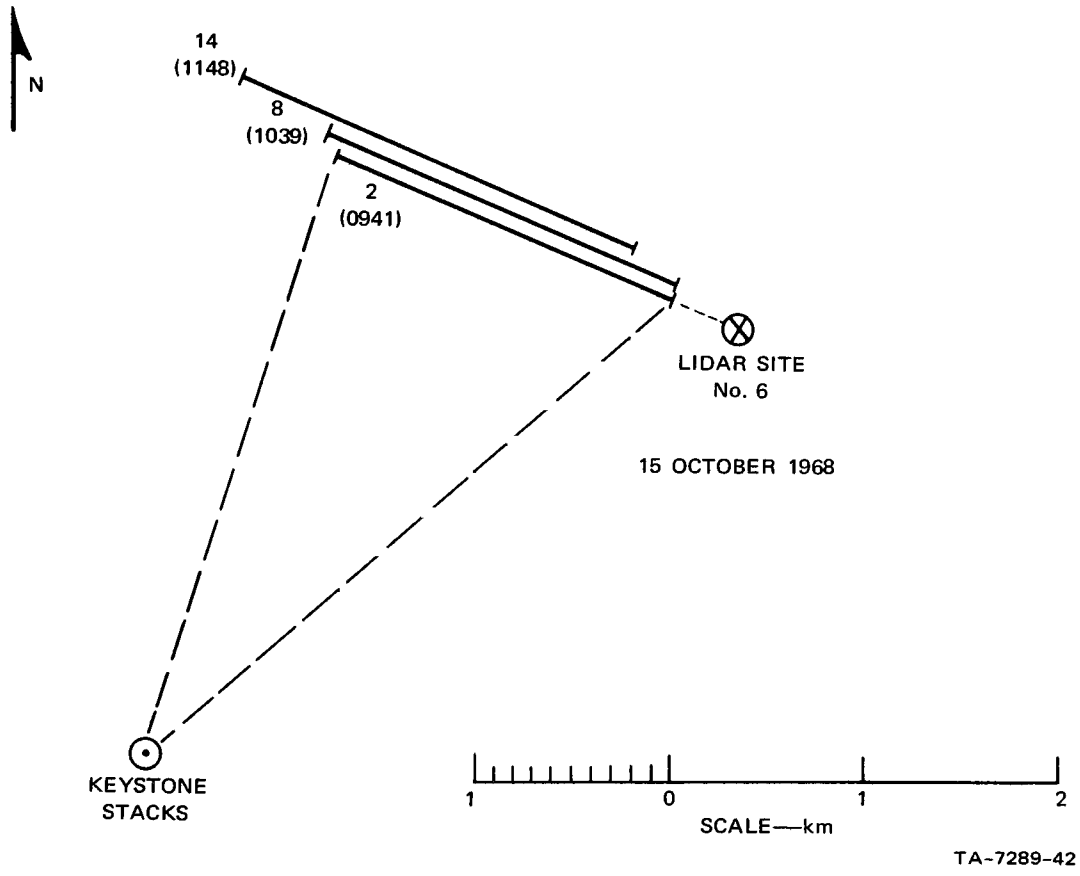

FIGURE D-1 PLAN VIEW OF HORIZONTAL PLUME POSITIONS, 15 OCTOBER 1968
Cross section numbers and times in EDT are shown beside each horizontal plume position.

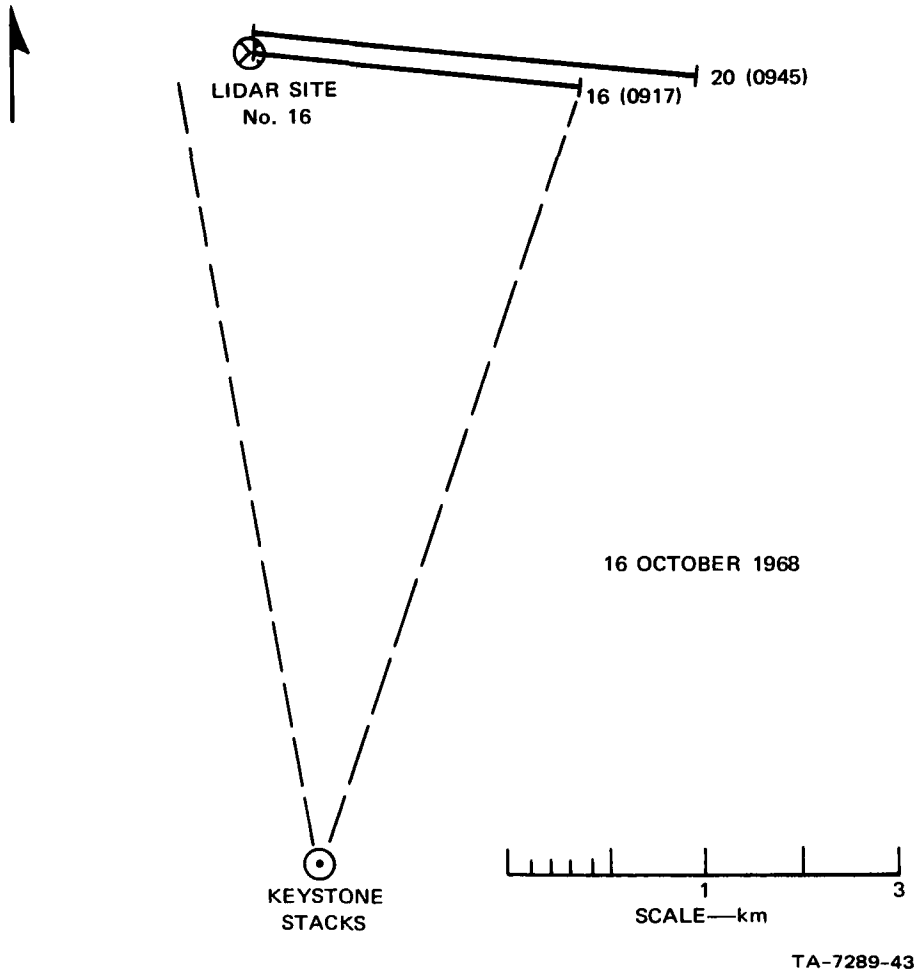

FIGURE D-2 PLAN VIEW OF HORIZONTAL PLUME POSITIONS, 16 OCTOBER 1968

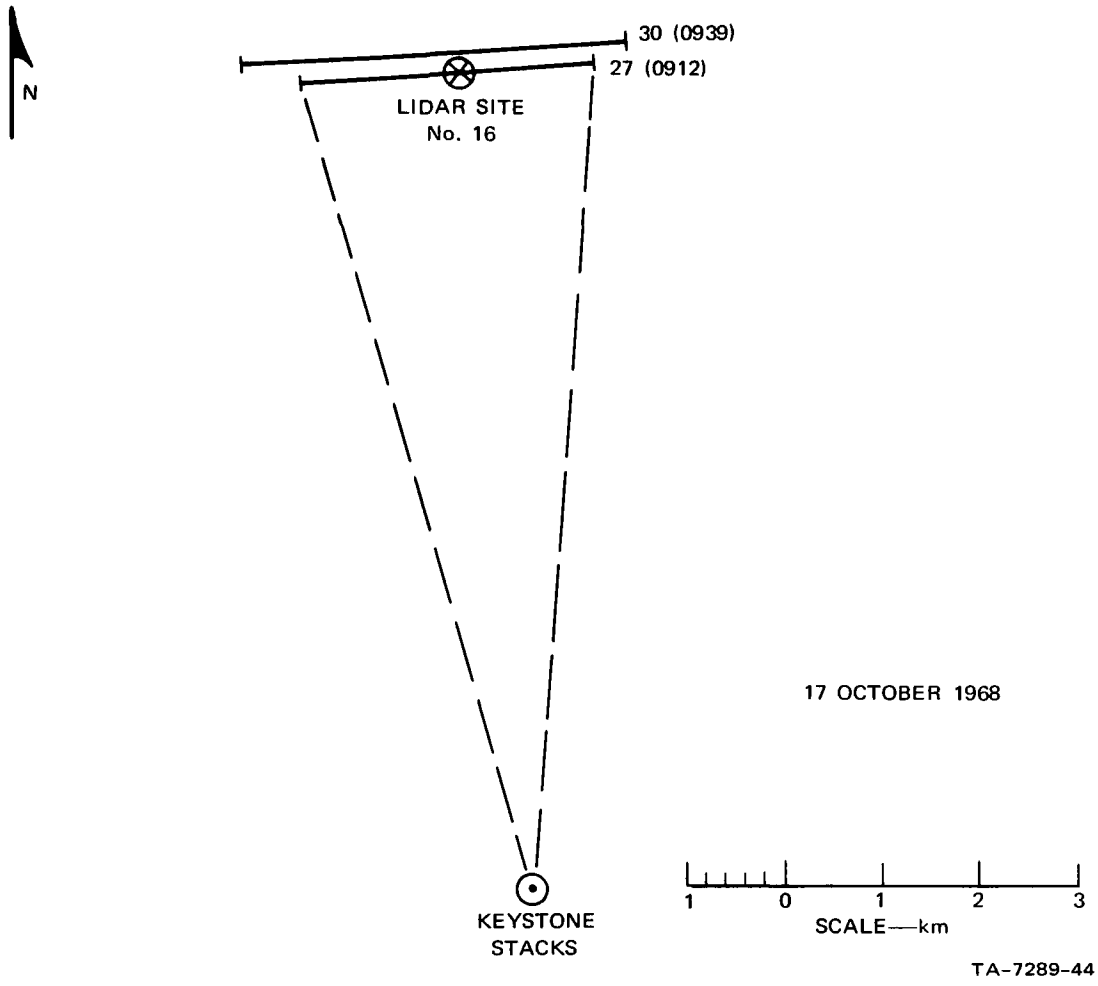

FIGURE D-3 PLAN VIEW OF HORIZONTAL PLUME POSITIONS, 17 OCTOBER 1968

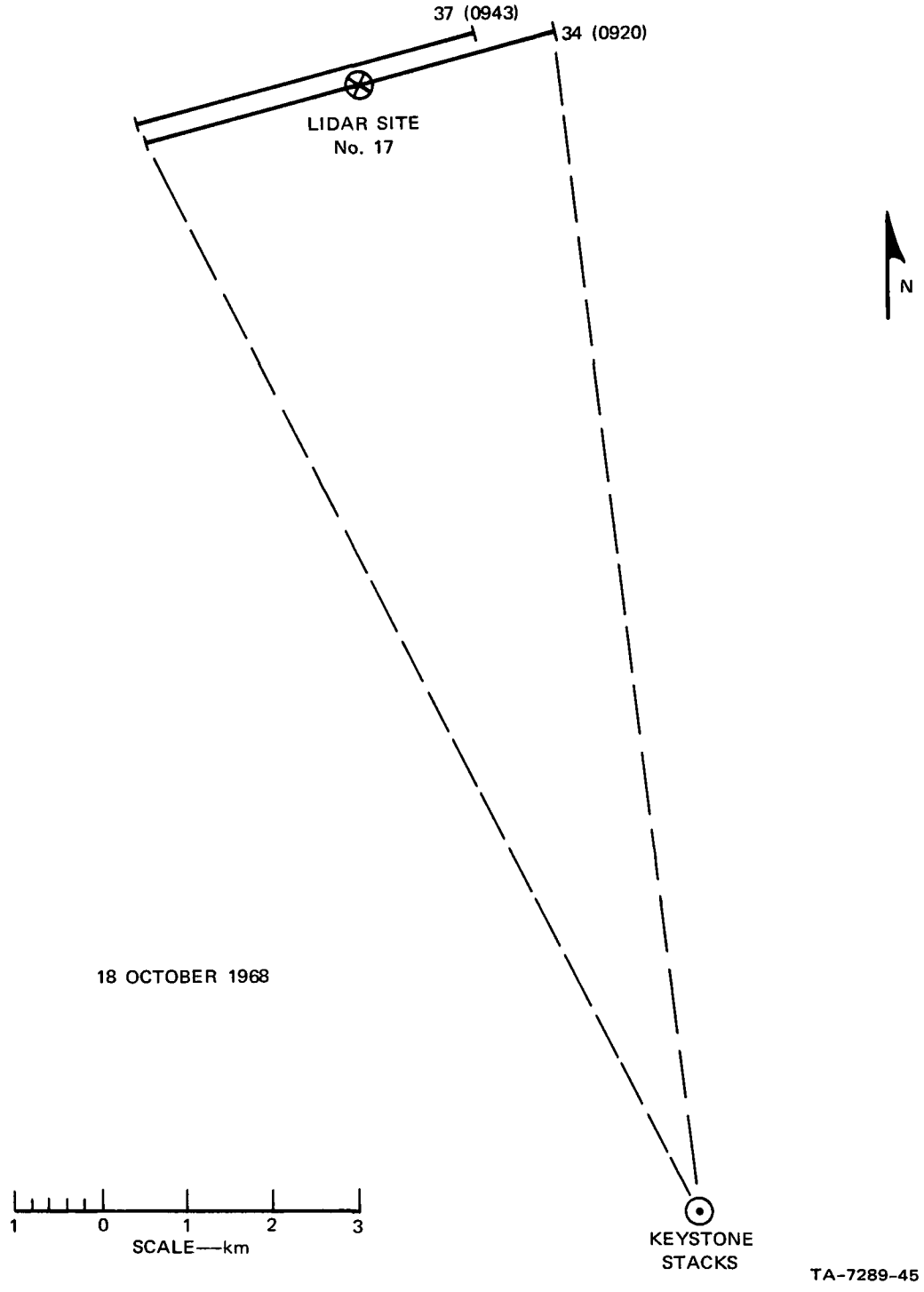

FIGURE D-4 PLAN VIEW OF HORIZONTAL PLUME POSITIONS, 18 OCTOBER 1968

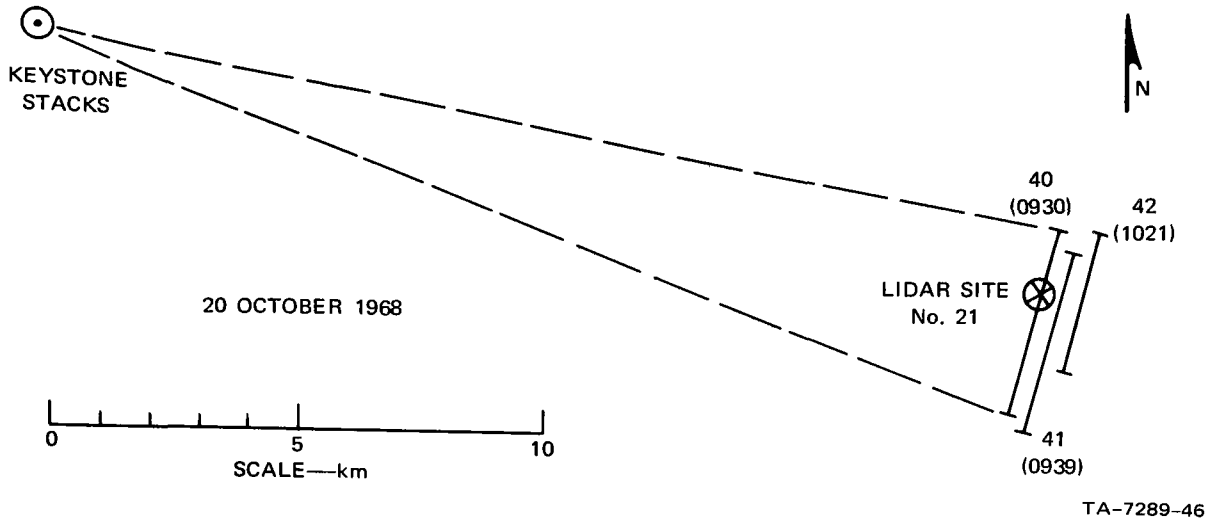

FIGURE D-5 PLAN VIEW OF HORIZONTAL PLUME POSITIONS, 20 OCTOBER 1968

For those observation series where the azimuth angle was held constant and the plume structure observed as a function of time, the first cross section in the series is shown at the proper position, and subsequent cross sections are displaced slightly for graphic purposes to avoid superposition.

The horizontal plume boundaries interpolated between cross sections are indicated by dashed lines in the figures. It should be remembered that these illustrations show the total horizontal projection of the plume. At any given height, the plume would normally be narrower than this.

The cross section number and time (EDT) are shown beside each horizontal plume position.

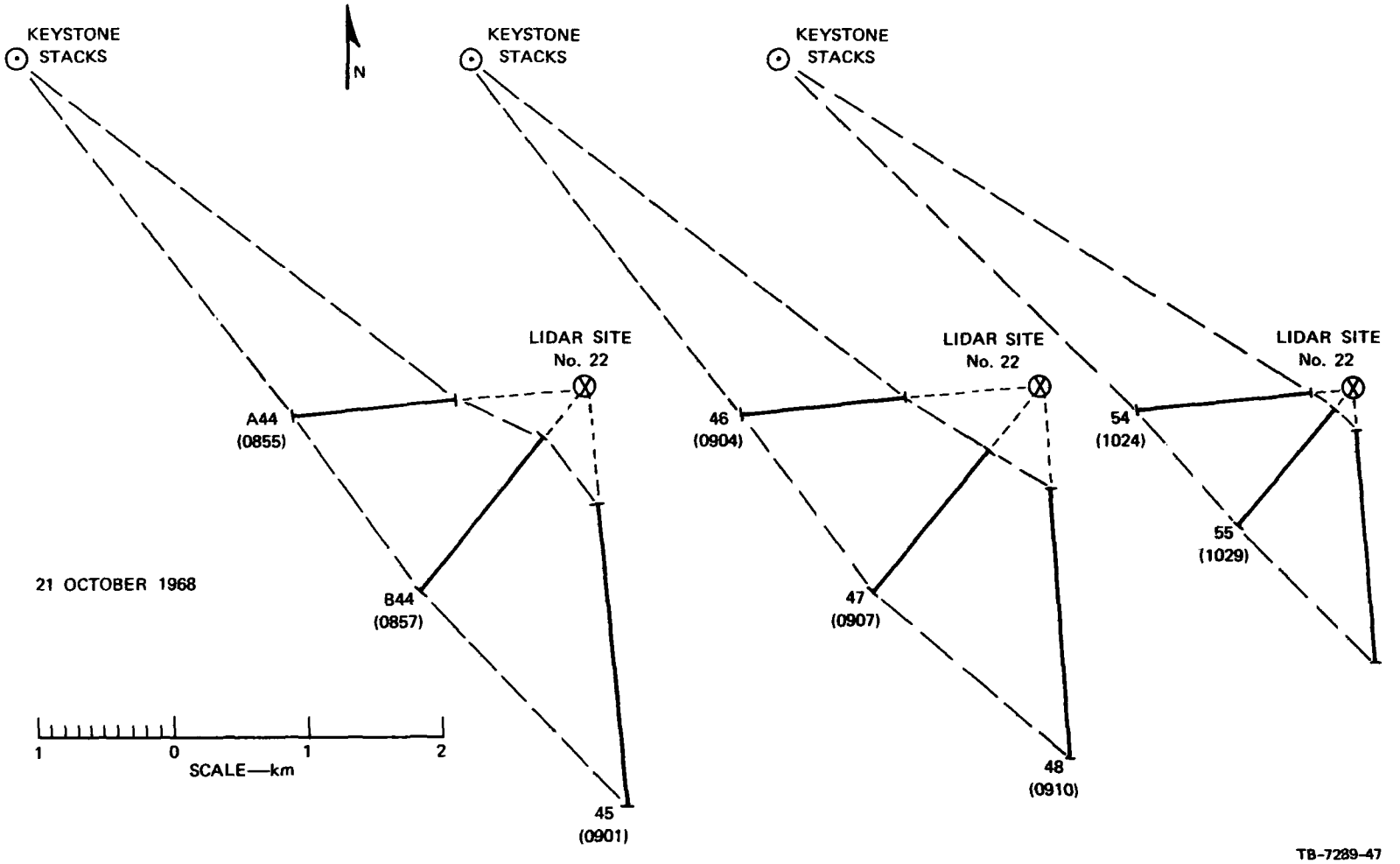

FIGURE D-6 PLAN VIEWS OF HORIZONTAL PLUME POSITIONS, 21 OCTOBER 1968

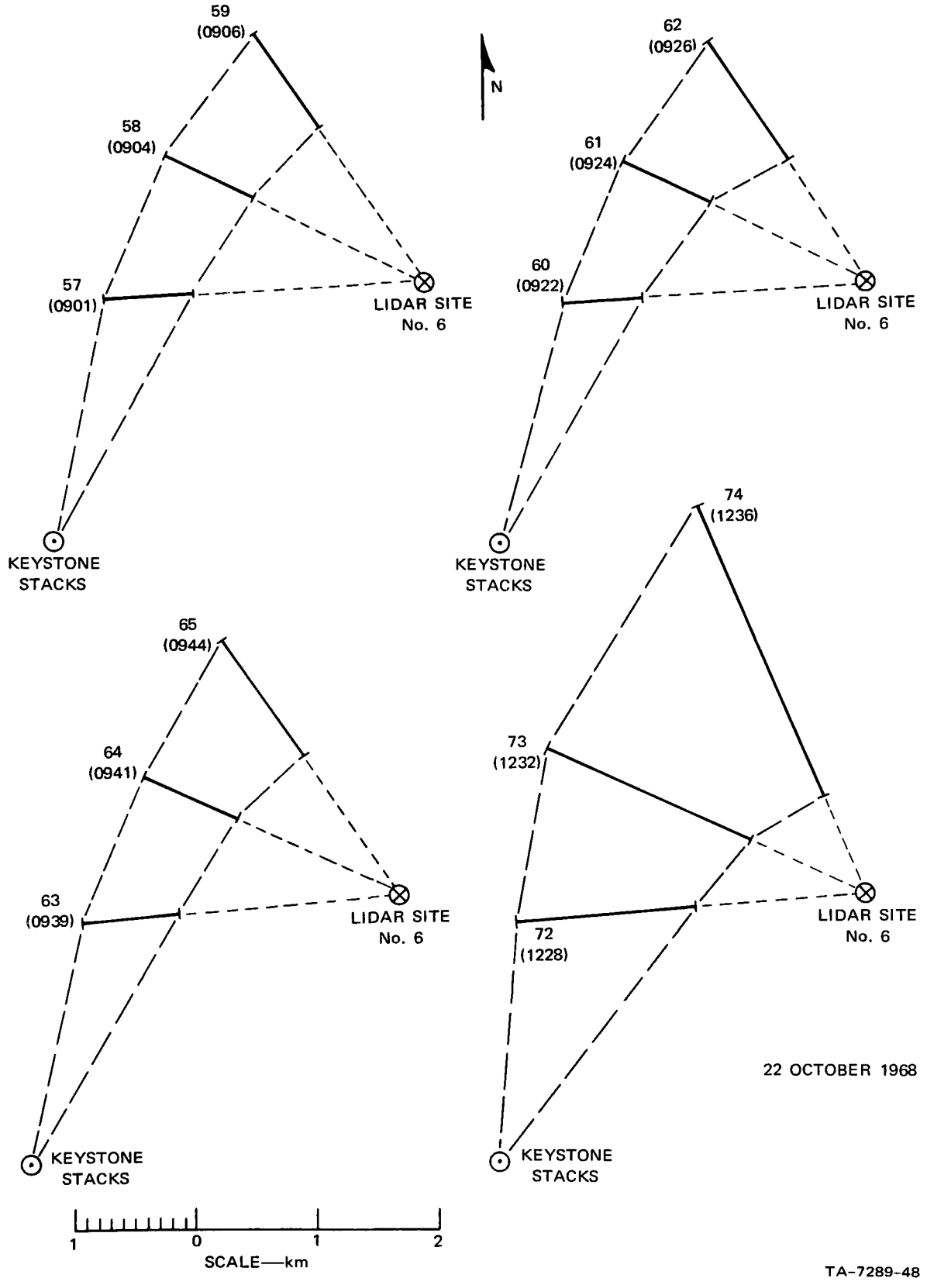

FIGURE D-7 PLAN VIEWS OF HORIZONTAL PLUME POSITIONS, 22 OCTOBER 1968

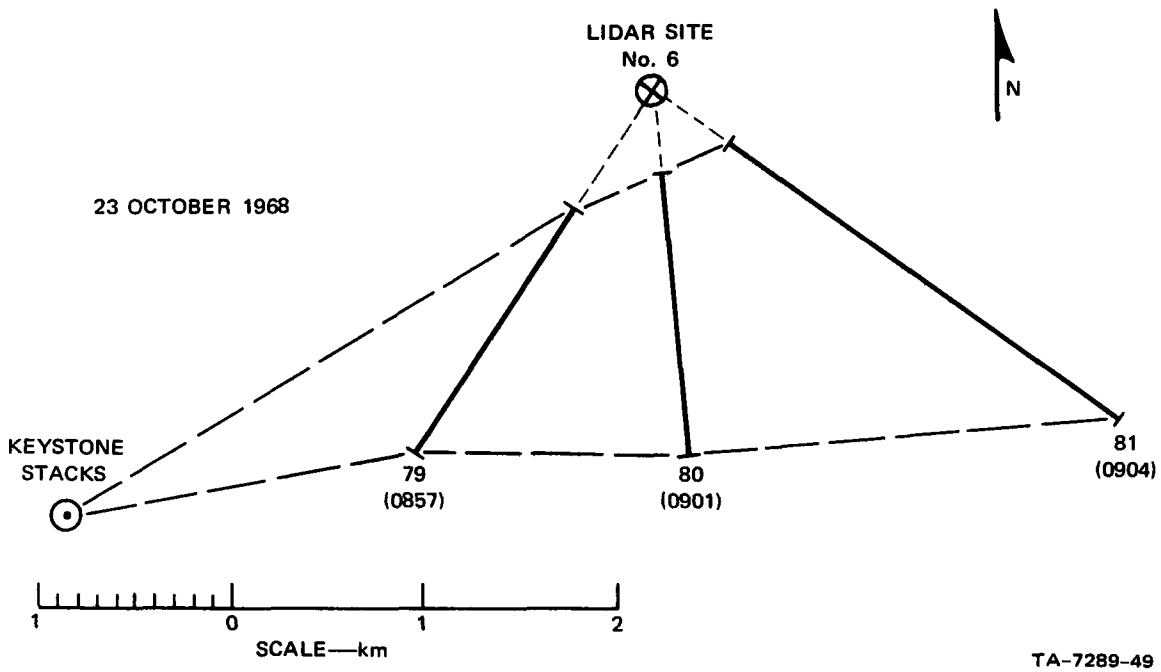

FIGURE D-8 PLAN VIEW OF HORIZONTAL PLUME POSITIONS, 23 OCTOBER 1968

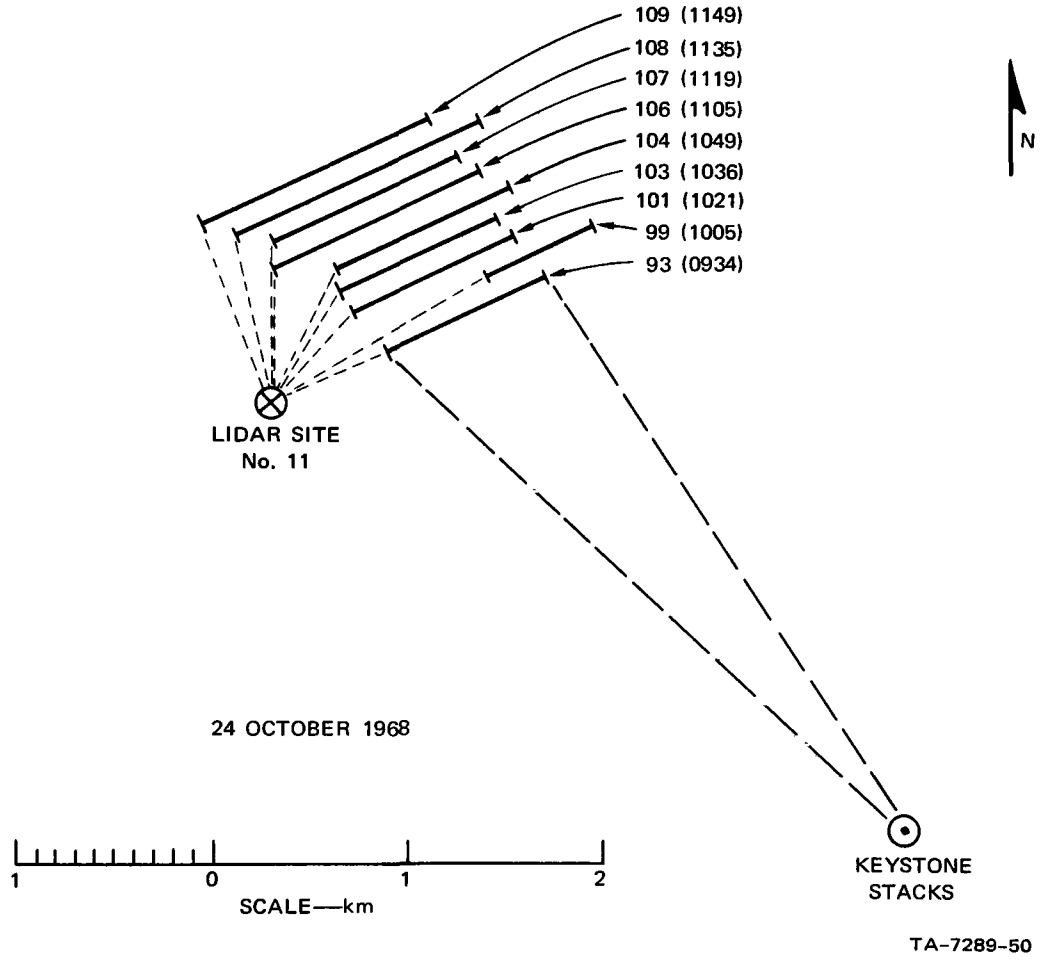

FIGURE D-9 PLAN VIEW OF HORIZONTAL PLUME POSITIONS, 24 OCTOBER 1968

Appendix E

LIDAR EYE-SAFETY CONSIDERATIONS

Appendix E

LIDAR EYE-SAFETY CONSIDERATIONS

Although often exaggerated, the question of safety in the use of experimental lidar systems should be carefully considered.

The series of observations described in this report were carried out with careful adherence to the safety procedures that have been developed and practiced by SRI teams over the last six years of field experiments. Some of the more important aspects of the safety question are described below.

The Mark V lidar pulse is harmless to the skin, but could cause eye damage in the form of a minute retinal lesion if the pulse were viewed directly. The lidar pulse takes the form of a cylinder of light, initially 15 cm in diameter and 6 m long, traveling through the atmosphere at the speed of light. Each pulse is only 0.00000002 s (0.02 μs) in duration, and the pulses occur approximately 5 s apart. The lidar is designed to totally prevent any emission of stray laser light from any direction other than that in which the unit is pointed.

Thus an eye hazard exists only at the exact instant of firing and only in the precise direction the lidar is aimed. The lidar is highly directional: the increase in diameter of the pulse with range (travel distance) is very slight--from 15 cm at the transmitter to 1.3 m at two miles range--so that the spatial extent of the hazard is confined to a very narrow cone. In this sense, the hazard from a lidar is directly analogous to that from a rifle or other firearm, except that the magnitude of the danger is considerably less for the lidar. This is because the pulse can only cause eye damage, and even then, only a partial (localized) loss of vision could result. Generally this loss would take the form of a blind spot ten times smaller than the natural one already present (and unnoticed) in every human eye at the location of the optic nerve.

Our standard general safety procedures for field experiments (which have proven worthy by use in many projects) are as follows:

(1) Mechanical stops are placed on the equipment to confine the pointing angles to a specific field of view.

(2) Aiming and firing is accomplished manually by an operator who uses an aiming telescope to monitor the field of view, as well as a large surrounding area. This operator is the only person who can fire the lidar, and he does not trigger the unit until he is sure the area is clear.

(3) A separate observer equipped with binoculars also keeps the entire firing area under surveillance. This observer is equipped with an override switch to prevent firing of the lidar when any human activity (airplane, ship, etc.) is sighted in the firing area.

(4) When not being fired, the lidar is always rendered completely safe by a switch which discharges the capacitor bank furnishing high voltage to the laser flash lamps. Without this high voltage supply, the lidar cannot be fired.

(5) As an additional precaution, the stowage position of the lidar is such that it is never pointed at eye level.